

Probing elliptical orbital configuration of the close binary of supermassive black holes with differential interferometry

Andjelka B. Kovačević¹, Yu-Yang Songsheng^{2,3}, Jian-Min Wang^{2,3,4}, Luka Č. Popović^{3,1}

¹ Department of astronomy, Faculty of mathematics, University of Belgrade Studentski trg 16, Belgrade, 11000, Serbia
e-mail: andjelka@matf.bg.ac.rs

² Key Laboratory for Particle Astrophysics, Institute of High Energy Physics, Chinese Academy of Sciences, 19B Yuquan Road, Beijing 100049, China
e-mail: songshengyuyang@ihep.ac.cn, wangjm@ihep.ac.cn

³ School of Astronomy and Space Science, University of Chinese Academy of Sciences, 19A Yuquan Road, Beijing 100049, China

⁴ National Astronomical Observatories of China, Chinese Academy of Sciences, 20A Datun Road, Beijing 100020, China

⁵ Astronomical observatory Belgrade Volgina 7, P.O.Box 74 11060, Belgrade, 11060, Serbia
e-mail: lpopovic@aob.rs

Received ; accepted

ABSTRACT

Context. Detections of electromagnetic signatures from the close binaries of supermassive black holes (CB-SMBH) is still a grand observational challenge. The Very Large Telescope Interferometer (VLTI), and the Extremely Large Telescope (ELT) will be a robust astrophysics suite offering the opportunity of probing the structure and dynamics of CB-SMBH at high spectral and angular resolution. **Aims.** Here, we explore and illustrate the application of differential interferometry on unresolved the CB-SMBH systems in elliptical orbital configurations. We also investigate peculiarities of interferometry signals for a single SMBH with clouds in elliptical orbital motion.

Methods. Photocenter displacements between each SMBH and regions in their disc-like broad line regions (BLR) appear as small interferometric differential phase variability. To investigate the application of interferometric phases for the detection of CB-SMBH systems, we simulate a series of differential interferometry signatures, based on our model comprising ensembles of clouds surrounding each of supermassive black hole in a CB-SMBH. Setting model to the parameters of a single SMBH with elliptical cloud motion, we also calculated a series of differential interferometry observables for this case.

Results. We found various deviations from the canonical S-shaped of CB-SMBH phases profile for elliptically configured CB-SMBH systems. The amplitude and specific shape of the interferometry observables depend on orbital configurations of the CB-SMBH system. We get distinctive results when considering antialigned angular momenta of cloud orbits regarding total CB-SMBH angular momentum. We also show that their velocity distributions differ from the aligned cloud orbital motion. Some simulated spectral lines from our model closely resemble observations of Pa α line got from near-infrared AGN surveys. We found differences between differential phases ‘zoo’ of a single SMBH and CB-SMBH systems. The differential phases ‘zoo’ for a single SMBH comprises deformed S shape. We also showed how their differential phase shape, amplitude, and slope evolve with various sets of cloud orbital parameters and observer position.

Conclusions. We calculated an extensive atlas of the interferometric observables, revealing distinctive signatures for the elliptical configuration of close supermassive binary black holes. We also provide interferometry atlas for the case of a single SMBH with clouds in an elliptical motion, differing from those of CB-SMBH. These maps can be useful for extracting exceptional features of the BLR structure from future high-resolution observations of CB-SMBH systems, but also of a single SMBH with clouds in elliptical orbital setup.

Key words. Techniques: interferometric–quasars: supermassive black holes –quasars: emission lines, Pa α

1. Introduction

Observations of active galactic nuclei (AGN) probe the extreme limits of physical conditions in the universe set by the event horizon of a supermassive black hole (SMBH) in their centers. Our view of AGNs was limited until technologically advanced observatories, and monitoring campaigns uncover their electromagnetic spectrum. Particularly, information about broad line regions (BLRs) surrounding SMBH comes mainly from reverberation mapping (RM) campaigns (Peterson et al. 1998, 2002, 2004; Kaspi et al. 2000, 2007; Shapovalova et al. 2001, 2004, 2008, 2010a,b, 2012, 2013, 2016, 2017, 2019; Bentz et al. 2008, 2009; Denney et al. 2009; Barth et al. 2011, 2013, 2015; Popović et al. 2011, 2014; Grier et al. 2012; Wang et al. 2014;

Du et al. 2014, 2015, 2016, 2018b; Shen et al. 2016; Grier et al. 2017; Edelson et al. 2019; Pancoast et al. 2019; Wang et al. 2020a). Most of these data suffer from ‘Static Illusion’, because what we can observe with this method perhaps changes on timescales larger than centuries ($10^4 - 10^7$ yr, Elvis 2001). The problem is most apparent in the periodicity detection in the light curves of AGNs. AGNs mostly appear stationary with notable exceptions, such as changing look AGNs (see, e.g. Wang et al. 2018b; Shapovalova et al. 2019; Ilić et al. 2020).

RM campaigns indicate that the largest BLR radii can be a few hundreds of light days, this is equivalent to angular sizes of $\sim 100\mu\text{as}$ for nearby AGNs, which is well below the canonical resolution of optical interferometry instruments (e.g., $\sim 3\text{mas}$

for VLTI/GRAVITY, Gravity Collaboration et al. 2017). Still, interferometry could offer a qualitatively new view of these objects. It is possible to obtain optical interferometry information from non-resolved sources measuring the displacement of object photocenter with wavelength. It was used first by speckle interferometry, then adopted by long baseline interferometry and finally has been one of the design parameters of the VLTI focal instrument AMBER (see Petrov 2012, and references therein). AMBER was the first generation near-infrared instrument of VLTI, with one of the goal to study AGNs (Petrov 2006). Several authors (Jaffe 2004; Swain 2004; Kishimoto 2009; Weigelt et al. 2012) have done pioneering optical-interferometric observations of some Seyfert I AGNs. Petrov (2012) reported the first optical interferometry observations of the BLR of a quasar just a decade ago. The GRAVITY instrument at the VLTI had made a significant breakthrough when its differential phase precision $< 1^\circ \sim 10 \mu\text{as}$ allowed Gravity Collaboration (2018) to probe and detect successfully disc-like BLR in 3C 273¹. A recent high signal-to-noise, decadal reverberation mapping campaign by Zhang et al. (2019) yielded $H\beta$ time lag (to the continuum 5100 Å) of ~ 146.8 light days in the rest frame, which agrees well with the Pa α region (145 light days) measured by the GRAVITY.

However, the Event Horizon Telescope (EHT), the first planetary very long baseline interferometric array, obtained the first image of the shadow of a spinning Kerr SMBH in the M87 galaxy (Akiyama et al. 2019). Safarzadeh et al. (2019) pointed out that M87 at the center of the cluster of galaxies has the possibility of its SMBH mass growth through mergers of neighboring galaxies (Hopkins et al. 2006). Their analysis implies the existence of a binary companion such as an intermediate-mass black hole (Colpi et al. 2009). Safarzadeh et al. (2019) argued that the EHT long-term monitoring campaign of M87 at $\sim 1 \mu\text{as}$ positional accuracy would detect small mass SMBH companion of M87. The differential interferometry is among the very promising techniques for detection of close binaries of supermassive black holes (CB-SMBH Songsheng et al. 2019a). Also, the dispersion, in AGN mass-luminosity relation (based on RM measurements of SMBH masses) amount to about a factor of three (Peterson et al. 2004); this systematic uncertainty decreases when using RM and differential interferometry measurements. Wang et al. (2018a) have recently proposed kinematic signatures based on 2D transfer functions, that can be derived from RM campaigns, as a promising avenue to address the problem of CB-SMBH detection (Songsheng et al. 2020).

The process of synergy between RM and interferometry investigations of AGN has already begun. The long-term RM project ‘The Monitoring AGNs with $H\beta$ Asymmetry’ (MAHA), using the Wyoming Infrared Observatory 2.3 m telescope, explores the geometry and kinematics of the gas responsible for complex $H\beta$ emission-line profiles that also provides the opportunity to search for evidence of CB-SMBH (see Du et al. 2018a). Also, Songsheng et al. (2019a) have already presented the first atlas of expected differential phases of circular CB-SMBH systems. They found that the current GRAVITY setup can detect differential phase curves because of the circular orbital motion of CB-SMBH. In this work, we consider the central question of the modeling interferometry observables of eccentric orbital settings of clouds in a single SMBH and eccentric orbital configurations of CB-SMBH systems. As for excitation of binary orbital elongation, advanced N-body or hydrodynamical simulations have showed major mergers of gas-rich disc galaxies with

central SMBHs (Mayer et al. 2007; Cuadra et al. 2010; Sesana 2010; Roedig et al. 2011). For binary systems with a circumbinary accretion disc, the binary can reach a limiting eccentricity of ~ 0.6 (Roedig et al. 2011) through the inspiral. Sesana (2010) proposed that scattering of bound and unbound stars in the galactic bulge excites high eccentric binary systems. Then circularization can occur when the gravitational wave shrinking time-scale is smaller than the gas or star induced binary migration. But, once again, a significant amount of eccentricity can be gained when the binary occupies the frequency band of gravitational wave observations. The excitation of binary eccentricity also has physical consequences (Roedig et al. 2011). Binaries with larger eccentricity will coalesce on a shorter time-scale due to faster GW energy loss (Peters and Mathews 1963). Accretion flows leaking through the cavity, and fueling SMBHs can induce a more prominent periodicity signal (Artymowicz and Lubow 1996), which can increase the binary identification via time-variability. In this paper, we extend and refine the search for specific features of differential interferometry $\xi(\lambda)$ and spectroscopic $\Xi(\lambda)$ functions to the case of CB-SMBH systems with elliptical orbits and the BLR configurations. The results are in the form of an atlas showing the evolution of $\xi(\lambda)$ and $\Xi(\lambda)$ functions with varying parameters of orbital configurations.

The outline of the paper is: in Section 2, we briefly overview our CB-SMBH phenomenological model and introduce interferometric observables. General inferences about differential phase shape for single SMBH and CB-SMBH, based on a first order approximation, are given in Appendix A. The chosen results of the simulations, also resembling real-AGN spectral lines, are described in two separate Subsections 3.1 and 3.2, related to single SMBH and CB-SMBH, respectively. Detailed results are included in the Appendices B, C and D for single SMBH, aligned and anti-aligned CB-SMBH, respectively. In Section 4, we discuss anticipated results from observations, limitations of the present model, and some implications of random clouds’ motion on interferometric observables. Finally, Section 5 concludes the paper by summarizing our results.

2. Spectroastrometry: Spectral lines and Differential phase

Here we present the elliptical CB-SMBH interferometry-oriented model. We first briefly summarize our dynamical CB-SMBH model and introduce equations of the observable quantities of elliptical CB-SMBH interferometry.

2.1. Recapitulation of CB-SMBH model

To study, characterize, and illustrate the evolution of differential phases of a single SMBH with elliptical clouds motion in a disc-like BLR surrounding it as well as CB-SMBH system and clouds in their BLRs on elliptical orbits, we used the model which closely resembles that in Kovačević et al. (2020). Here, we only briefly recall the key aspects and some modifications and refer the reader to the above paper for further details. In this paper, we adopt the following notation: a bold font variable refers to a 3×1 vector, and unless otherwise specified, the indices $k = 1, 2$ are used to discern parameters of the primary and secondary component. We identify the respective quantities for the cloud in the BLR with the subscript c, which can be followed by index $k = 1, 2$ if a cloud is in the BLR of primary or secondary. Solely used subscript c indicate that all clouds in the BLR have the same value of a particular parameter. We define M_1 and M_2

¹ the differential phase precision differs from resolving the object.

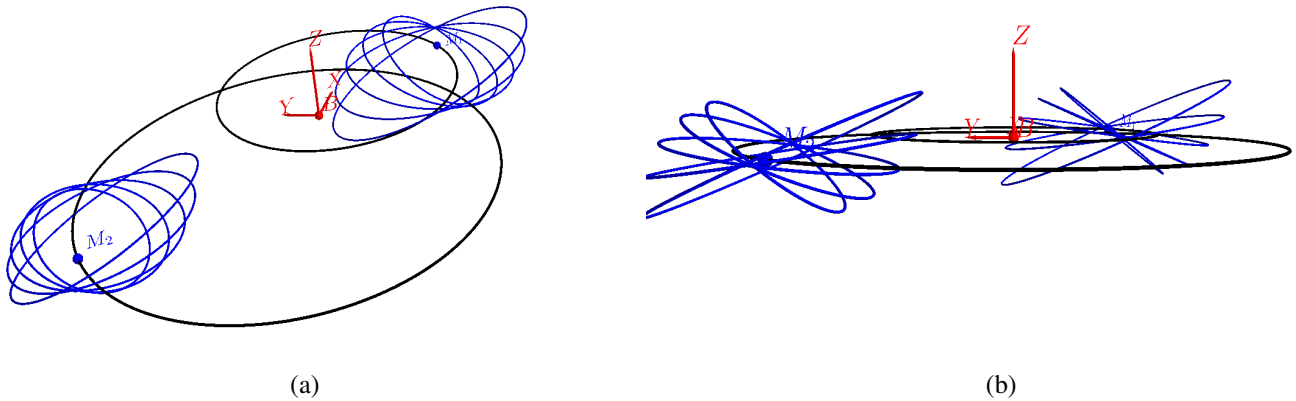


Fig. 1. Realization of a coplanar elliptical CB-SMBH system with clouds in non-coplanar orbits in both BLRs calculated from the model. M_1 and M_2 are the locations of the SMBHs in a binary system. Blue ellipses are every 20th of the 100 orbits of clouds in each BLR. SMBH parameters are $M_1 = 6 \cdot 10^7 M_\odot$, $M_2 = 4 \cdot 10^7 M_\odot$, $A_0 = 100$, $\Omega_1 = \Omega_2 = 3^\circ$, $\omega_1 = 1^\circ$, $\omega_2 = 181^\circ$, $e_1 = e_2 = 0.5$. Clouds parameters are $\Omega_{c1} = \Omega_{c2} = 180^\circ$, $\omega_{c1} = 2^\circ$, $\omega_{c2} = 182^\circ$, $i = (-40^\circ, 40^\circ)$, $e = 0.5$, but their orbital planes have different inclinations. The reference plane (BXY) is the plane of the relative orbit of M_2 to M_1 , and the origin of the coordinate system is the barycenter (B) of the CB-SMBH system. (a) An elevation view of the CB-SMBH system. (b) A side view to the YBZ coordinate plane.

Table 1. Model parameters and their range of values used in simulations.

Parameters	Description	Range or monotony	Values in simulations
(M_1, M_2)	SMBHs masses in $10^7 M_\odot$		(6, 4)
q	$\frac{M_2}{M_1}$	(0,1)	$\frac{2}{3}$
\mathcal{A}_0	Semimajor axis of SMBHs relative orbit [ld]		(100, 175)
(a_1, a_2)	SMBHs semimajor axes		$(\frac{q\mathcal{A}_0}{1+q}, \frac{\mathcal{A}_0}{1+q})$
$(e_1 = e_2)$	SMBHs orbital barycentric eccentricities	(0,1)	(0.05, 0.5)
(i_1, i_2)	SMBHs orbital barycentric inclinations ^a		(0°, 45°)
$(\Omega_k, \omega_k, k = 1, 2)$	longitude of ascending node and argument of pericenter of SMBHs barycentric orbits	(0°, 360°)	(0°, 360°)
$(f_k, k = 1, 2)$	true anomaly of SMBHs orbits	(0°, 360°)	(0°, 90°, 180°)
(a_1^c, a_2^c)	semimajor axes of clouds orbits in BLRs around SMBHs [ld]		((20, 40), (16, 32))
(e_1^c, e_2^c)	clouds orbital eccentricities	(0,1)	(0.05, 0.5), $\Gamma, (0.3, 1)$, $\mathcal{R}(1)$
(i_1^c, i_2^c)	clouds orbital inclinations		(0°, 45°) \vee (90°, 175°) ^b
$(\Omega_k^c, \omega_k^c, k = 1, 2)$	longitude of ascending node and argument of pericenter of cloud orbits	(0°, 360°)	(0°, 360°)
Auxiliary parameters			
\mathfrak{I}	varied range of clouds orbital inclinations within single simulation		$\mathfrak{I} = i_{min}^c + i_{max}^c$
i_0	angular position of the observer		(0°, 45°)
\mathbf{J}_{bin}	CB-SMBH angular momentum	$\mathbf{J}_{bin} \cdot \mathbf{J}_k \leq 0$	$\mathbf{J}_{bin} > 0$
$\mathbf{J}_k^c, k = 1, 2$	BLRs angular momenta	$\mathbf{J}_{bin} \cdot \mathbf{J}_k^c \leq 0$	$\mathbf{J}_{bin} \cdot \mathbf{J}_k^c \leq 0$

Notes. ^(a) Degeneration of barycentric orbits can arise for different reasons such as third body gravitational interaction known to be significant in some cases, quadrupole or relativistic precession. We take into account non-coplanar CB-SMBHs as one of the degenerate cases. However, the latter two effects are irrelevant for qualitative orbital characteristics at short observational time scales. In any situation, there is a freedom to select the coordinate system so that the parameterization is convenient and reasonable (Klioner 2003)

^(b) The first and the second range of clouds orbital inclinations are equivalent to the angular momenta conditions $\mathbf{J}_{bin} \cdot \mathbf{J}_k^c > 0$ and $\mathbf{J}_{bin} \cdot \mathbf{J}_k^c < 0$, respectively.

to be the primary and secondary SMBH masses ($M_1 > M_2$), respectively and

$$q = \frac{M_2}{M_1} < 1$$

to be the CB-SMBH mass ratio.

All model parameters are defined in Kovačević et al. (2020), but we briefly describe them here for completeness. The input parameters are five orbital elements defining the size and shape (a, e, i, Ω, ω) of orbit and time t . The output parameters are position ($\mathbf{r}(t)$) and velocity ($\dot{\mathbf{r}}(t)$) of SMBHs and each cloud in the

BLRs, obtained by solving Kepler's equation:

$$\{a, e, i, \Omega, \omega, \mathcal{M}, t\}_k \Rightarrow \text{Kepler's Eqn.} \Rightarrow \{\mathbf{r}(t), \dot{\mathbf{r}}(t)\}_q, k = 1, 2 \quad (1)$$

where \mathcal{M} is mean anomaly. The barycentric vector \mathbf{n} defines the line of the sight. Then the binary inclination angle to the observer is $\cos i_0 = \mathbf{n} \cdot \mathbf{J}_{bin}$ where \mathbf{J}_{bin} is the normalized orbital angular momentum vector of the CB-SMBH system. There is no reason to expect AGN not to be oriented randomly, meaning all orientations are equally likely. We will estimate the probable inclination angle of such an object. The relative likelihood that AGN inclination is within a differential range between di and $i + di$ of a specific inclination angle i is proportional to the area on the unit sphere covered by that range of angles. The solid angle defined by the inclination range i to $i + di$ equals $w = 2\pi \sin i$, then we can write the probability density function as a geometric probability in the form of a ratio of w and the solid angle of complete sphere

$$d(Prob) = \frac{w}{4\pi} = \frac{2\pi \sin i di}{4\pi} = \frac{d \cos i}{2}.$$

From this, we got that it is more likely to observe highly inclined AGN whereas the probability of observing an object at inclination i_0 is $\sim \sin i_0$.

For the case of single SMBH, we adopted physical parameters given in Kovačević et al. (2020), while for the CB-SMBH system, we used physical parameters given in Songsheng et al. (2019a, see Table 1). For the BLRs, we adopted a disc-like model. The BLR kinematic structures for about two dozens of AGNs, inferred from velocity-resolved RM, indicate a virialized disc, inflow, and outflow BLR geometries (see Lu et al. 2019, and references therein). The latest finding of Lu et al. (2019) indicates that the BLR of Mrk 79, which is sub-Eddington accreting AGN, probably originates from a disc wind launched from the accretion disc. We will focus on the most straightforward BLR elliptical disc-like geometry here to simulate differential observables.

Returning briefly to the subject of circular binaries (with orbital eccentricities $e_i = 0, i = 1, 2$, and semi-major axes $a_i, i = 1, 2$), we point out the time independence of the relative distance of two SMBH

$$|\mathbf{r}(e_1 = 0, e_2 = 0)| = a, \quad (2)$$

where $a = a_1 + a_2$. In circular case, the velocities of SMBHs and their relative velocity are also time-independent. However, in the case of elliptical configurations of clouds in the BLR of SMBH and elliptical CB-SMBH system, the positions and velocities depend on time and osculating orbital elements. Our model accounts for all these parameters, as explained in Kovačević et al. (2020). We used the parameter ranges in Table 1 to generate different combinations of parameters, and run simulations with 100 clouds in each BLR. The clouds orbital positions are uniformly sampled at every time instance $t_n, n = 1, \dots, 1000$. All simulations were performed at the initial CB-SMBH orbital phase, if not stated otherwise. As an illustrative example, one realization of elliptical geometrical configuration of CB-SMBH, depicted from the elevated and the side, is shown in Fig. 1. Moreover, Fig. 2 illustrates how our model captures dynamics and consequently the distribution of radial velocities of clouds in two BLRs occurring for different clouds' orbital angular momenta alignments to the CB-SMBH orbital angular momentum using randomly chosen orbital parameters. We set the radial velocity distributions at clouds positions in each BLR on the same plot for comparison. For each cloud in the disc-like BLR, we determine its combined velocities of orbital motion sampled at 1000

points of its orbit and its angular momenta, taking into account its central SMBH motion. We then project the clouds velocity field onto the plane of the observer for a value of i_0 to determine the line-of-sight projection of the combined velocity at each position in the inclined disc-like BLRs. The maximum of V_1 and V_2 radial velocities of the primary and secondary components in CB-SMBH occur at passing the ascending node in their true orbits. The epoch of passage through the ascending node corresponds to the instant when radial velocity of the secondary component reaches maximum (or when the radial velocity of the primary component reaches minimum). The asymmetry of distributions is a consequence of the asymmetry of elliptical orbital motions of SMBHs and clouds. There is a distinction between radial velocity distributions (see Fig. 2). Specifically, we see the topological difference between velocity fields for aligned (Fig. 2a) and anti-aligned orbital configurations of clouds (Figs. 2b-2d). Clouds in anti-aligned orbits have inclinations between 90° and 175° consequently. Velocity field for anti-aligned clouds orbital momenta shows elongated features that are strained. In all these cases, clouds orbital inclinations are linearly spaced between given boundaries. Velocity fields are the closed surfaces,² preserving topological volume and surface coherency³. We also tested the cases where inclinations are randomly distributed within given ranges, and such velocity fields of the BLRs are not volume-preserving in the topological sense.

For aligned BLRs, the absolute value of velocity increases toward the outer left and right side lobes of disc-like BLRs (regarding the smaller BLR diameter). However, with anti-aligned BLRs, the absolute value of velocity increases toward frontal and backward lobes (oriented in the directions of larger BLR diameters).

As discussed above, the general form of equations for calculation of brightness distribution of singular SMBH and CB-SMBH system is the same as in Songsheng et al. (2019a), but the difference is that the input and output variables depend on the time. Replacing the double integral by a summation on the coordinates of clouds, and time with single SMBH gives a discrete form of equations. For the CB-SMBH system, the summation is on the coordinates of clouds in the BLRs, both SMBHs and time.

2.2. Differential phase

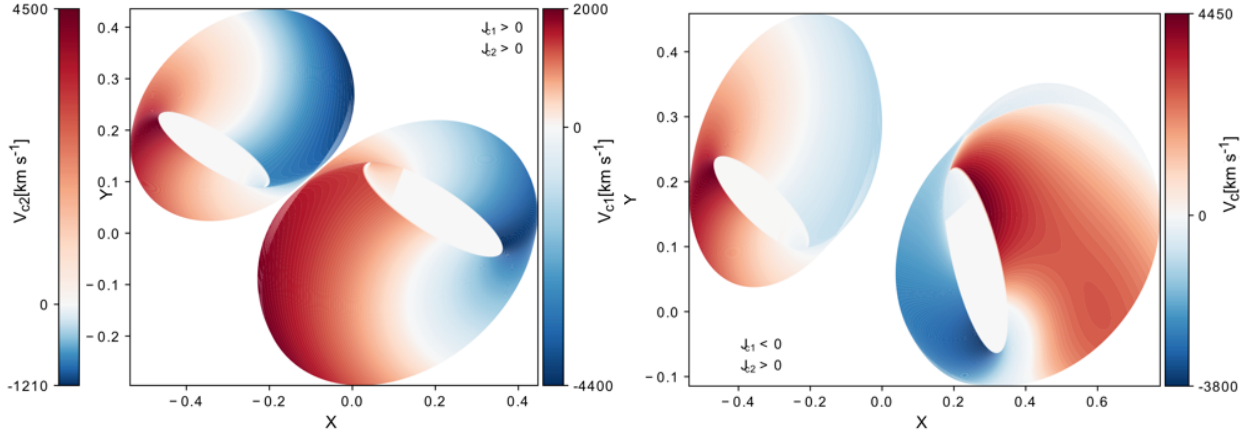
The primary advantage of using differential phase measurements is that their uncertainties are reduced in the case of narrow spectral lines and they are not contaminated by wavelength-independent errors (see Waisberg et al. 2017). We modeled the differential phases from the computed brightness distribution according to the prescription given by (Songsheng et al. 2019a) based on the Zernike-van Cittert's theorem. In particular, from this theorem, we obtain:

$$Q(\mathbf{u}, \lambda) = \iint I(\boldsymbol{\sigma}, \lambda) e^{-2\pi i \boldsymbol{\sigma} \cdot \mathbf{u}} d\alpha d\beta \quad (3)$$

where $Q(\mathbf{u}, \lambda)$ is a coherent flux of the object, $I(\boldsymbol{\sigma}, \lambda)$ is the intensity of the object emission in the observer direction, transferred the spectral channel of band $\delta\lambda$ and centered on the wavelength λ ; $\boldsymbol{\sigma} = (\alpha, \beta)$ is the celestial angular coordinates of an emitting point in the object, and $\mathbf{u} = \frac{\mathbf{r}}{\lambda} = (u, v)$ is the interferometry

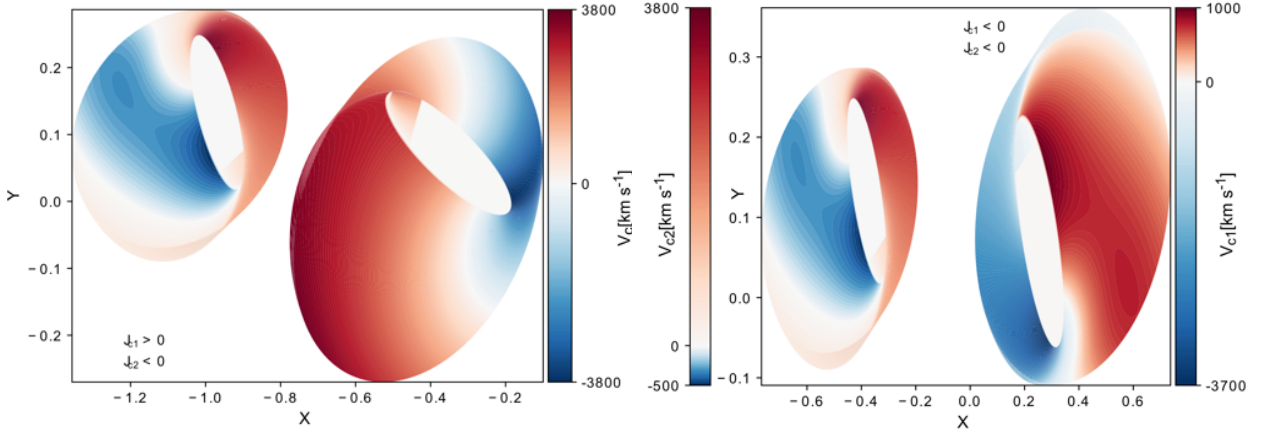
² Compact and without boundary surface is closed. Notable examples are the sphere and torus. An example of non-closed surfaces is a cylinder.

³ We use coherence in the sense that levels of velocity intensity do not fluctuate widely.



(a) $A_0 = 175 \text{ld}$, $i_0 = 40^\circ$, $i = 80^\circ$, ld , $\Omega_1 = 300^\circ$, $\Omega_2 = 50^\circ$, $e_k = 0.5$, $k = 1, 2$, $\omega_1 = 70^\circ$, $\omega_2 = 250^\circ$, $i_{c1} = i_{c2} = 40^\circ$, $\Omega_{c1} = \Omega_{c2} = 300^\circ$, $\omega_{c1} = 70^\circ$, $\omega_{c2} = 250^\circ$, $e_c = 0.5$

(b) $A_0 = 175 \text{ld}$, $i_0 = 40^\circ$, $i = 80^\circ$, $\Omega_1 = 300^\circ$, $\Omega_2 = 50^\circ$, $e_k = 0.5$, $k = 1, 2$, $\omega_1 = 70^\circ$, $\omega_2 = 250^\circ$, $i_{c1} = (90^\circ, 175^\circ)$, $i_{c2} = 40^\circ$, $\Omega_{c1} = \Omega_{c2} = 300^\circ$, $\omega_{c1} = 70^\circ$, $\omega_{c2} = 250^\circ$, $e_c = 0.5$



(c) $A_0 = 175$, $i_0 = 40^\circ$, $i = 80^\circ$, ld , $\Omega_1 = 300^\circ$, $\Omega_2 = 50^\circ$, $e_k = 0.5$, $k = 1, 2$, $\omega_1 = 70^\circ$, $\omega_2 = 250^\circ$, $i_{c1} = 40^\circ$, $i_{c2} = (90^\circ, 175^\circ)$, $\Omega_{c1} = \Omega_{c2} = 300^\circ$, $\omega_{c1} = 60^\circ$, $\omega_{c2} = 240^\circ$, $e_c = 0.5$

(d) $A_0 = 175$, $i_0 = 40^\circ$, $i = 80^\circ$, ld , $\Omega_1 = 300^\circ$, $\Omega_2 = 50^\circ$, $e_k = 0.5$, $k = 1, 2$, $\omega_1 = 70^\circ$, $\omega_2 = 250^\circ$, $i_{c1} = i_{c2} = (90^\circ, 175^\circ)$, $\Omega_{c1} = \Omega_{c2} = 300^\circ$, $\omega_{c1} = 60^\circ$, $\omega_{c2} = 240^\circ$, $e_c = 0.5$

Fig. 2. Radial velocity maps of simulated images of the BLRs around the primary and secondary components in CB-SMBH. Abscissas (X) and ordinates (Y) are normalized by the $\mathcal{A}_0 = 100 \text{ld}$. Clouds orbital angular momenta alignment with CB-SMBH orbital angular momentum is indicated in legends.

baseline vector. By defining the moments of intensity distribution (see details in Waisberg et al. 2017).

$$\mu_{lm} = \iint I \delta \lambda(\sigma, \lambda) \alpha^l \beta^m d\alpha d\beta \quad (4)$$

one can see that μ_{00} is total intensity of the object, while the normalized first order moments give the centroid positions:

$$p_\alpha(\lambda) = \frac{\mu_{10}}{\mu_{00}} = \frac{\iint \alpha I(\sigma, \lambda) d\alpha d\beta}{\iint I(\sigma, \lambda) d\alpha d\beta}, \quad (5)$$

$$p_\beta(\lambda) = \frac{\mu_{01}}{\mu_{00}} = \frac{\iint \beta I(\sigma, \lambda) d\alpha d\beta}{\iint I(\sigma, \lambda) d\alpha d\beta}$$

Consequently, we have that $Q(0, \lambda) = \mu_{00} = \Xi(\lambda)$. The emission line ($\Xi(\lambda)$) is the zero order moment of brightness distribution of the object.

Also, from the Zernike-van Cittert's theorem, the fringe phase is:

$$\begin{aligned} -\text{Arg}\left(\frac{Q(\mathbf{u}, \lambda)}{\mu_{00}}\right) &\sim \frac{\int \sin(2\pi\boldsymbol{\sigma} \cdot \mathbf{u}) I(\boldsymbol{\sigma}, \lambda) d\alpha d\beta}{\int \cos(2\pi\boldsymbol{\sigma} \cdot \mathbf{u}) I(\boldsymbol{\sigma}, \lambda) d\alpha d\beta} \\ &\sim 2\pi \frac{\int I(\boldsymbol{\sigma}, \lambda) \boldsymbol{\sigma} d\alpha d\beta}{\int I(\boldsymbol{\sigma}, \lambda) d\alpha d\beta} \cdot \mathbf{u} \\ &\sim 2\pi \mathbf{u} \cdot \boldsymbol{\xi}(\lambda) \\ &= 2\pi u_\alpha \xi_\alpha(\lambda) + 2\pi v_\beta \xi_\beta(\lambda) \end{aligned} \quad (6)$$

Let us now consider an unresolved source ($\mathbf{u} \cdot \boldsymbol{\sigma} < 1$), for which is possible to relate vectorial components given in Eq. 6 to the photocenter p_α, p_β (Eq. 5) of the intensity distribution (see details in Jankov et al. 2001):

$$\xi_\alpha(\lambda) = \frac{\mu_{10}}{\mu_{00}} = p_\alpha(\lambda) \quad \xi_\beta(\lambda) = \frac{\mu_{01}}{\mu_{00}} = p_\beta(\lambda) \quad (7)$$

The terms in Eq. 7 are the fringe phase components. They are proportional to the photocenter of intensity distribution and equivalent to the first moment of the intensity distribution. However, the fringe phase can be disrupted by the atmospheric turbulence if only one baseline (two telescopes) is used. This problem

can be reduced with the differential phase $\Delta\phi$ (see, e.g. Delaa et al. 2013, and references therein). The differential phase is defined as the difference between the fringe phases obtained in two spectral channels centered on the wavelengths λ and λ_r , respectively

$$\Delta\phi = -2\pi\mathbf{u} \cdot (\xi(\lambda) - \xi(\lambda_r)) \quad (8)$$

This quantity is relevant for line profiles when accounting for the kinematics of the source, and the continuum region is the natural choice as a reference so that $\xi(\lambda_r) = 0$ (see Domiciano de Souza et al. 2004). Thus, the first vectorial component of differential phase (Eq. 7) is usually observed and modeled in the literature. We have also followed this approach. It has been shown both empirically (Gravity Collaboration 2018) and theoretically (Songsheng et al. 2019a) that differential interferometry produces a variation of BLR photocenter $\xi(\lambda)$. It is an unexploited astrophysical parameter in AGN investigation, with an interpretation similar to the BLR spectral lines $\Xi(\lambda)$. Line profiles reveal a large scale spatial and physical effects of the BLRs. But with $\xi(\lambda)$ we can check and add new details to the spectroscopic information to get a complete picture of the object. The information in $\xi(\lambda)$ is always new, because the weights of contribution of different parts of the object in $\Xi(\lambda)$ and $\xi(\lambda)$ are different (Petrov 1989).

All the interferometric data are usually quantitatively interpreted within the frame of a single, self-consistent physical model, which should produce observables. Modern spectro-interferometers can measure the variation of the interferometric phase across an emission line of AGN (Gravity Collaboration 2018). This first measurement of phase displays a simple S-shaped profile comprising a single reversal, arising from the line emission from a circular rotating disc-like BLR. The S form is one of the most common observed differential phase shapes, and here we briefly explained it.

Assuming that the source has Gaussian spatial brightness distribution, $\mathbf{G}(\sigma, \lambda)$, and integrating $\xi_a(\lambda)$ (see Eq. 7) in both directions β and α , we get that differential phase shapes is

$$\xi_a(\lambda) \sim \text{Gaussian}(\alpha) \text{erf}(\beta)$$

where erf is a 'error function' of sigmoid shape which causes differential phase (Eq. 8) to be of S shape. In general, Lachaume (2003) showed that the differential phase can be related to the skewness and diameter of the object flux distribution.

Songsheng et al. (2019a) showed the same reasoning for interferometric observables is valid for the CB-SMBH case. The interferometric model of the CB-SMBH system is a composition of two sources (their BLRs) considered either as point-like or disc-like models with assumed morphologies. Let we denoted the brightness of disc-like BLR components as $I_k(\sigma_k, \lambda)$ and their barycentric positions (σ_k) , $k = 1, 2$.

The total brightness distribution of such system can be written as

$$I(\sigma, \lambda) = I_1(\sigma_1, \lambda) + I_2(\sigma_2, \lambda). \quad (9)$$

Taking into account Eq.3, Eq. 9, additional and translational property of Fourier transform one can get that coherent flux is simply

$$Q(\mathbf{u}, \lambda) = Q_1(\mathbf{u}, \lambda) + Q_2(\mathbf{u}, \lambda) = F_1 e^{-2\pi i \sigma_1 \cdot \mathbf{u}} + F_2 e^{-2\pi i \sigma_2 \cdot \mathbf{u}} \quad (10)$$

where F_1 and F_2 are the fluxes of components. Normalization gives

$$Q_n(\mathbf{u}, \lambda) = \frac{F_1 e^{-2\pi i \sigma_1 \cdot \mathbf{u}} + F_2 e^{-2\pi i \sigma_2 \cdot \mathbf{u}}}{F_1 + F_2} \quad (11)$$

We can expand the complex exponential terms in Eq. 11 in a Taylor series:

$$e^{-2\pi i \sigma_k \cdot \mathbf{u}} \sim 1 - 2\pi i (\sigma_k \cdot \mathbf{u}) - \mathcal{O}((\sigma_k \cdot \mathbf{u})^2), \quad k = 1, 2 \quad (12)$$

Taking into account that $\arctan(x) \sim x$ when $|x| < 1$ and $|\sigma_k \cdot \mathbf{u}| < 1$, $k = 1, 2$, we can estimate

$$\text{Arg}(Q_n(\mathbf{u}, \lambda)) \sim \arctan\left(\frac{\text{Im}(Q_n(\mathbf{u}, \lambda))}{\text{Re}(Q_n(\mathbf{u}, \lambda))}\right) \sim 2\pi\mathbf{u} \cdot \frac{F_1\sigma_1 - F_2\sigma_2}{F_1 + F_2} \quad (13)$$

If the binary components are on circular orbits, then $\sigma_1 = \sigma$ and $\sigma_2 = \sigma$, where σ is a component barycentric distance. Under this condition, the Eq. 13 shows that $\xi(\lambda)$ signal is proportional to the binary separation σ . However, with CB-SMBH on elliptical orbits, we can expect $\xi(\lambda)$ signal to be more complex. Especially, since spectral lines are compound functions of the form $F_k = \Xi_k(\lambda, \mathbf{r}_{km}^c, \mathbf{V}_{km}^c)$, $k = 1, 2, m = 1, 100$ where $\mathbf{r}_{km}^c, \mathbf{V}_{km}^c$ are composite vector field, representing at each position (\mathbf{r}_{km}^c) of the m -th cloud in the k -th BLR its velocity \mathbf{V}_{km}^c given in CB-SMBH barycentric coordinate system (see Kovačević et al. 2020).

Moreover, Eq. 9 -13 show us that the primary difference between the binary and single model is that the brightness distribution is no longer symmetric, what makes the differential phase to be a complex function.

2.3. Observational constrains

The differential phase of the circular CB-SMBH system depends on extrinsic parameters (the inclination of a CB-SMBH system to the observer) and intrinsic parameters (an opening angle of the BLR, SMBH masses and their mutual distance, and orientation of total angular momentum) as it was shown in (Songsheng et al. 2019a). Here we extend analysis on non-coplanar CB-SMBH system with varying orbital elements, and randomly distributed clouds orbital inclinations, eccentricities, and semi-major axes. We choose clouds in randomly inclined orbits as an interesting case based on Wanders et al. (1995) model of C IV emitting region of NGC 5548 with an ensemble of clouds on randomly inclined and spherically distributed orbits around the continuum source. However, this spectral line is observed as blue-shifted with certain blue-asymmetric features, perhaps indicating material outflow. Because of these characteristics, the C IV emitting region is distinctive from those related to H β and Pa α . Moreover, emission line profiles are indicators of the BLR gas kinematics. No one of the functional forms (i.e., Gaussian, Lorentzian, even Power law) is connected directly to the ordered motion of clouds in the BLR. Except for double-peaked profiles, all spectroscopic line shapes are consistent with randomly oriented orbits in a gravitationally bound cloud system (see Netzer 2013). Randomly distributed clouds' orbital semi-major axes and eccentricities lead to their random position, velocities and orbital angular momenta. We calculated differential phases for a 100-meter baseline with a position angle of 90° to the direction of the semi-major axis of the CB-SMBH system. The differential phases correspond to the emission Pa α line, which rest-frame wavelength is $\lambda_0 = 1.875\mu\text{m}$ for objects at redshift of $z \sim 0.1$. These parameters correspond to sources (such as 3C 273), which are red-shifted enough so that the Pa α line is in the K band. This band is convenient because the emission is at least two times stronger in Pa α than in e.g. Bry (Petrov 2012). Moreover, as shown by Landt et al. (2008), the strongest Paschen hydrogen broad emission lines Pa α and Pa β are seen to be without strong

blends implying good measurement of their widths. The line attenuation by dust is much more reduced in the near-IR lines than in the optical and UV.

3. Results

Here we present our investigation of the effects of variation of SMBH and clouds orbital elements on the amplitude and shape of $\text{Pa}\alpha$ and corresponding differential phase. We present the results divided in the domains of observables of the single SMBH and CB-SMBH system. We select representative cases that resemble examples of “real-world” AGN discussed in SubSect 4.1. For each referred AGN, we show the models whose spectrum resembles the observations, and the predicted differential phases for that model. The plots from all the combinations of parameters (i.e. the atlas of spectra and differential phases) are moved to appendices. As expected, the phase signatures occur under specific conditions, and their diagnostic potential is clearer for some parameters than for others. The set of models being compared is composed of those in which one (or all) of the parameters could have different values. For reference, interferometric observables marked with a blue colour in plots were simulated for values at the lower end of the parameters ranges, if not stated otherwise.

3.1. Interferometric signatures of a single SMBH

Here, we explore potential effects, induced by changes in the elliptic orbital parameters of clouds in single BLR, on the interferometric observables. Before conducting our numerical simulations, we analyzed generalized forms of the first order approximation of differential phase (Appendix A.1). The predicted deformation of differential phase S shape is asymmetric indicating clouds elliptical orbital motion (see Fig. A.1).

Then we simulated the $\text{Pa}\alpha$ lines and corresponding differential phases by considering the orbital dynamics controlled by orbital elements of clouds and different values of the i_0 parameter. The curves are given as a function of the wavelength. For a better comparison, the scale of twin x-axis at the top of each plot is presented in radial velocity. First, we adopted that the clouds move on orbits with uniformly distributed inclinations $i_c = \mathcal{U}(-5^\circ, 5^\circ)$ and varying other parameters. The most dramatic evolutions of observables occur when varying either Ω_c or ω_c between 10° and 180° (see Fig. 3a). For fixed clouds orbital eccentricity $e = 0.5$ larger values of Ω and ω cause an increase of the amplitude of the differential phase (see Figs. 3a and 3b). Additionally, these two orbital angle parameters have more significant influence on the amplitude of differential phase when eccentricity is smaller as it is shown in Fig. A.1.

Further, these simulations capture another characteristic of the spectra: the flat-topped spectra can appear not only for circular motion but also because of clouds’ elliptical motion (see Figs. 3a and 3b). The shapes of the flat top depend on the angles Ω and ω of the elliptical orbits of clouds. Compared to simulations for small clouds’ orbital eccentricity, we recorded the most notable variations of differential phase shape associated with variation of angle i_0 , fixed high orbital eccentricity ($e = 0.5$) and orbital inclination $i_c = \mathcal{U}(-7.5^\circ, 7.5^\circ)$ (see Fig. 3c). The inclination of the observer i_0 and clouds orbital inclination affects similarly the slope of the differential phase (see Fig. 3c). Here we also identify a characteristic pattern of alternation of the amplitudes in the left and the right wing of differential phase because of variation of the clouds’ orbital pericenter ω (Fig. 3c).

All previous simulations assumed constant or homogenous distribution of clouds’ orbital eccentricities. As a valuable study

case, the novel simulations for non-homogenous clouds’ orbital elongation have been considered where some interesting effects affecting differential phase can occur. The detailed distribution of orbits is unknown because clouds have a wide distribution of masses. The elongation of these orbits changes with variation of clouds column densities: high column densities clouds allow for mildly elongated even circular orbits (the right-skewed eccentricity distribution), but low column density clouds require highly eccentric ones (the left-skewed eccentricity distribution Krause et al. 2011). We can now construct these distributions, reflecting assumptions about skewness based on clouds’ column density, which will be used in our simulations. Similar to the variable defined for construction of a skewed random spatial distribution of clouds in BLR models (see Wang et al. 2020a, and references therein), we sampled clouds orbital eccentricities from the left-skewed distribution given as:

$$\mathcal{E} = S\langle e \rangle + \frac{\langle e \rangle(1 - S)}{\alpha} \Gamma(\alpha, \beta) \quad (14)$$

where S is a random number from an uniform distribution between 0 and 1, $\langle e \rangle \sim 0.8$ is the mean value of the random variable, and parameters of Γ distributions are $\alpha = 0.3, \beta = 1$. The random variable in Eq. 14 is a shifted and scaled Γ distribution, thus we will refer to it as Γ_s . Randomly chosen samples of eccentricities increase steadily with a peak around $e \sim 0.65 - 0.8$.

After introducing the left-skewed eccentricity distribution, we outline the right-skewed distribution using Rayleigh distribution $\mathcal{R}(1)$ which probability density function is

$$\mathcal{R}(p) = \frac{x}{p^2} e^{-\frac{x^2}{2p^2}} \quad (15)$$

In contrast to Γ_s , random samples of clouds’ orbital eccentricities drawn from $\mathcal{R}(1)$ have a peak at $e \sim 0.2 - 0.4$. For each of these distributions of eccentricities and $\omega > 180^\circ$ of non-coplanar clouds, we observed various broad spectral lines and differential phases (compare Fig. 4a to Fig. 4b). Conversely, larger differential phases amplitudes are seen for coplanar orbital configurations of clouds. Clouds’ orbital setups drawn from \mathcal{R} yield differential phases with larger amplitudes than more elongated orbital layouts (following shifted Γ_s distribution). But the effects of observer position i_0 and clouds’ orbital inclinations are the same as in the models with a homogenous distribution of clouds’ eccentricities.

Distinctly, for models with clouds’ orbital parameter $\omega \lesssim 50^\circ$, the spectral lines and differential phases are narrower for observer angles smaller than 30° (see Fig. 4b). We found global geometrical pattern that differential phases are deformed regarding an invariant point in its right wing for coplanar orbital configurations and different observer positional angle (compare Figs. 4a and 4b). For any value of wavelength that is close enough to the wavelength of the invariant point, the differential phase values are close to the fixed point.

Based on our simulations, the shape of the differential phase obtained from the emission of clouds on elongated orbits is distinctive from circular ones. The typical S-shape signature of a rotating disk is clearly distorted. The peaks are deformed due to the superposition of trigonometric functions of angles controlling the orbital shape arising from the first term in the Eq. A.2 (see also Fig. A.1 upper plot). Also, an increasing cloud orbital inclination produces differential phases with smaller amplitudes. These distortions are an illustrative proof of the presence of an asymmetry in the disk. Meilland et al. (2011) showed that losing simple S shape, when stellar environments are dominated by

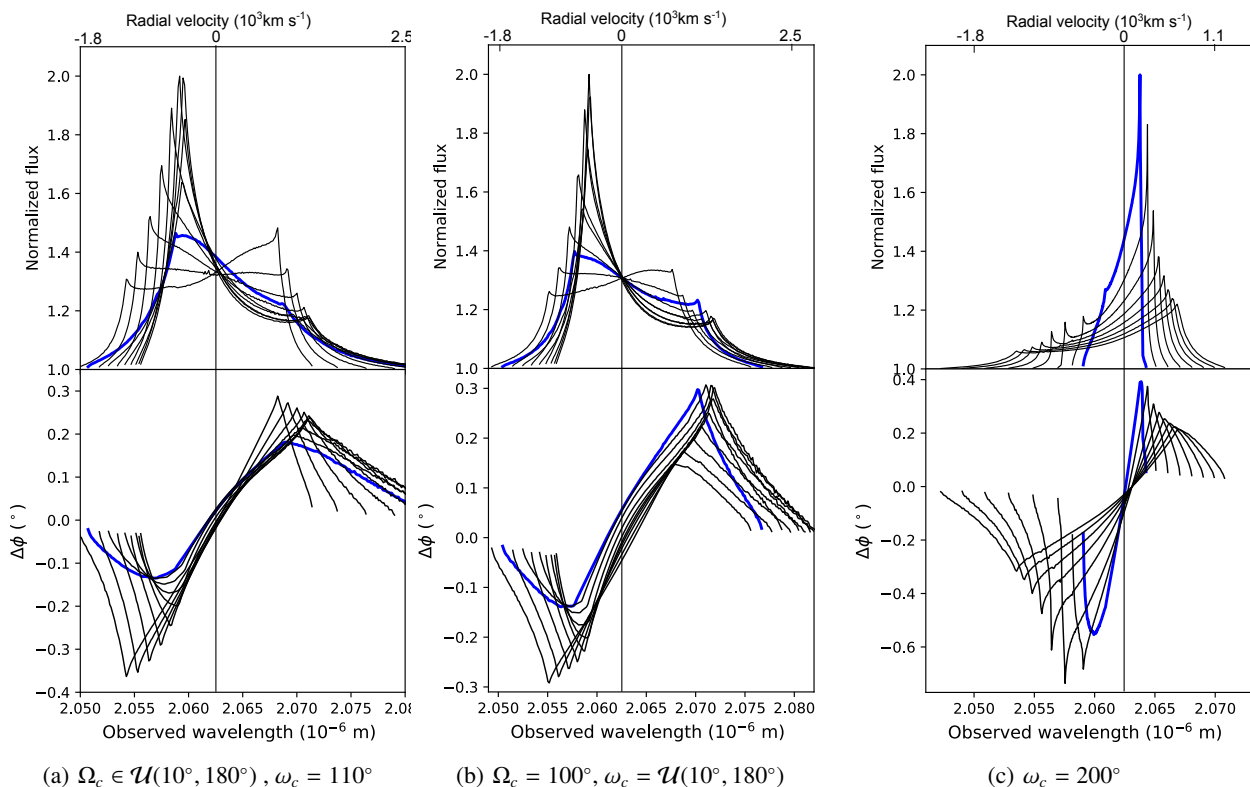


Fig. 3. Evolution of the Pa α emission line (upper subplots) and corresponding differential phase ($\Delta\phi$, lower subplots) as a function of the wavelength for different values of clouds’ orbital parameters in the different models of single SMBH. Common parameters for all models: (a) and (b) clouds’ orbital inclination $i_c \in [-5^\circ, 5^\circ]$, clouds’ orbital eccentricity $e_c = 0.5$ and $i_0 = 45^\circ$. (c) clouds’ orbital inclination $i_c = \mathcal{U}(-7.5^\circ, 7.5^\circ)$ and $i_0 = \mathcal{U}(10^\circ, 45^\circ)$. Varying parameters are given in subcaptions. $\mathfrak{J} = \mathcal{U}(l, r)$ stands for collection of inclination ranges from $\mathcal{U}(-l, l)$ up to $\mathcal{U}(-r, r)$. For reference, interferometric observables marked with blue colour were modeled for values at the lower end of the parameters ranges.

rotation, occurs for larger baselines. We summarize the simulation results in Table 2, which shows some general qualitative morphological characteristics of the differential phase for various simulation parameters. Appendix B provides detailed atlas of interferometric observables.

3.2. Interferometric signatures of CB-SMBH

Gravity Collaboration (2018) assumed that all clouds have ordered motion when they measured the BLR size and black hole mass of 3C 273. But as pointed out by Stern et al. (2005), and shown for circular CB-SMBH by Songsheng et al. (2019a), the phase curves could encode the distribution of angular momentum of clouds in the BLR. If the GRAVITY provides the angular momentum distribution of clouds, then the clue for BLR formation will be found as well (Wang et al. 2017). In our simulations, all clouds of individual BLRs have their own either clockwise or anticlockwise rotation. Then the total angular momentum of the BLR is the vector sum of the all clouds’ orbital angular momenta. The direction of the total BLRs angular momenta (either aligned or counter-aligned with the CB-SMBH system orbital angular momentum) has a strong effect on both interferometric observables as shown in further paragraphs. The orbital angular momentum of CB-SMBH is simply

$$\mathbf{J}_{bin} = \sum_{i=1,2} M_i \mathbf{V}_i \times \mathbf{r}_i^i$$

We define the orientation of the cloud orbits (with inclination i_c) to the invariable plane of the CB-SMBH system, which is

perpendicular to the total orbital angular momentum \mathbf{J}_{bin} . In the next we assume the net angular momenta of BLRs and the orbital angular momentum of CB-SMBH are independent of one another, so there are cases of CB-SMBH with all angular momenta aligned or when one or both of BLR net angular momenta are misaligned. In this section we will consider two sets of results: for aligned and anti-aligned CB-SMBH. Before simulation, we first predict the pattern of differential phases from first order approximation given in Appendix A.2. Prediction surfaces comprise a complex system of two ridges and valleys (see Fig. A.2). Because of such topology, deformed double S shapes are expected. We have presented more detailed atlases in Appendices C for aligned and D for anti-aligned CB-SMBH.

3.2.1. CB-SMBH system with aligned angular momenta

In these simulations, we focused on CB-SMBH systems which all clouds’ orbital angular momenta in both BLRs are aligned with the CB-SMBH system angular momentum $\mathbf{J}_{bin} \cdot \mathbf{J}_{ci} > 0$, $i = 1, 2$. This condition is equivalent to the condition that clouds in both BLRs have prograde motion, i.e. clouds’ orbital inclinations are $i_c < 90^\circ$. Fig. 5a shows some typical interferometry observables for aligned CB-SMBH systems. Even when the the spectral lines of both SMBH are well blended in blue-coloured models in Fig. 5a, corresponding differential phases still show two peaks. Hence small velocity differences can be measured with differential interferometry (see, e.g. Tokovinin 1992). The phases are most sensitive to the asymmetric brightness distribu-

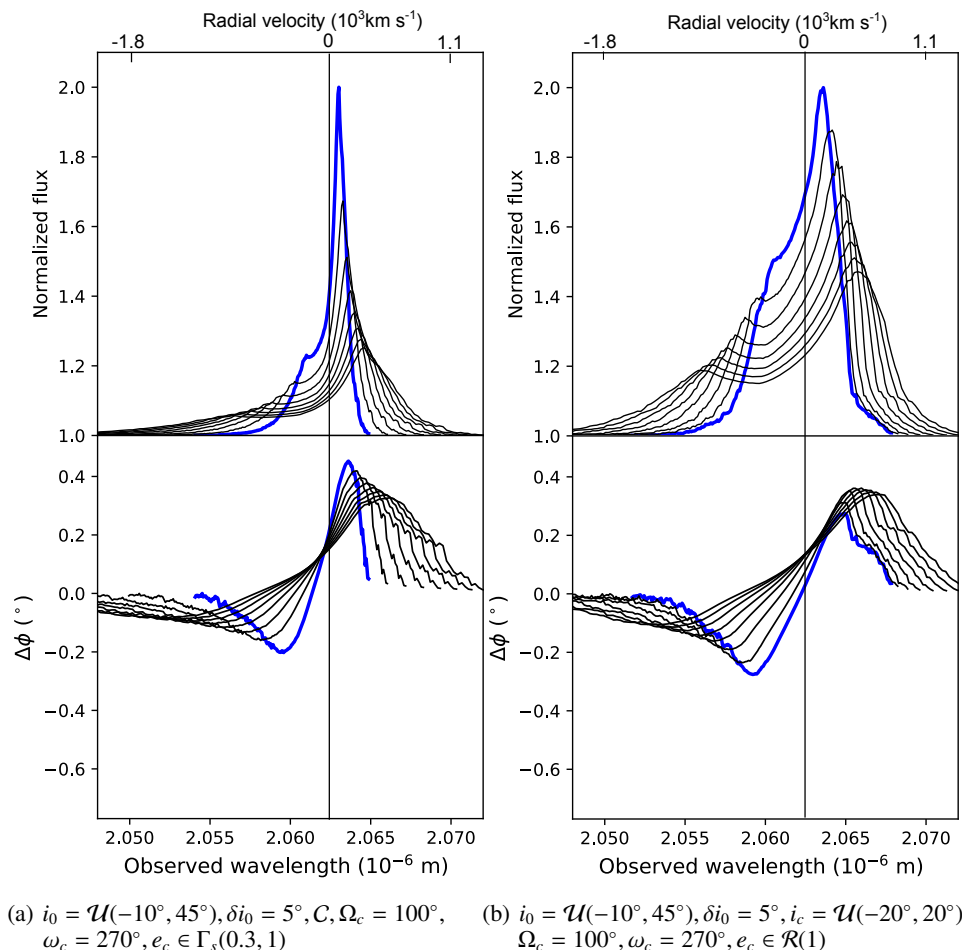


Fig. 4. Same as Fig. 3 but for random samples of clouds’ orbital eccentricities generated from $\Gamma_s(0.3, 1)$ and $\mathcal{R}(1)$ distributions. Varying parameters are listed in subcaptions, C stands for coplanar clouds orbits.

Table 2. Qualitative summary of simulation parameters effects on the morphology of differential phase (DP) curves for a single SMBH. The columns are: orbital and auxiliary parameters, range or monotony of parameters used in simulations, the effect on DP amplitude, and DP slope between two peaks.

Orbital element	Range or monotony	Amplitude	Slope
(e, i, Ω, ω)	$(0.1 - 0.5), (5^\circ - 40^\circ), > \frac{\pi}{2}, > \frac{\pi}{2}$	decrease	decrease
$(e, \text{coplanar orbits}, i_0)$	$(e \sim \Gamma_s(0.3, 1) \vee \mathcal{R}(1), C, (10^\circ - 45^\circ))$	increase, fixed point in the right wing	increase
$(e, \text{non-coplanar orbits}, i_0)$	$(e \sim \Gamma(0.3, 1) \vee \mathcal{R}(1), -C, (10^\circ - 45^\circ))$	decrease, no fixed point	decrease
i	increasing	decrease	decrease
Ω	increasing	increase	
ω	$< \frac{\pi}{2}$	prominent right wing	
ω	$> \frac{\pi}{2}$	prominent left wing	
Auxiliary parameters			
i_0	increasing	decrease	decrease

tion of the object. Even if the spectra might have differed a very little in peculiar aspects, the corresponding differential phases differ clearly. We found that there is a distinction between differential phases ‘zoo’ of a single SMBH and CB-SMBH systems.

Namely, the single SMBH phases ‘zoo’ consists of deformed but still recognizable S shape, which indicates the rotational motion of clouds in the BLR. The differential phases of CB-SMBH show a complex structured signal looking as two blended and deformed S-shaped signals. Differential phase variations are re-

lated to the orbital motions of clouds and SMBHs. These patterns are asymmetrical about the line center.

For fixed values of SMBHs and clouds’ orbital eccentricities, variations of the ranges of clouds orbital inclinations lead to an appearance of ridges in the wings of differential phases (see Fig. 5a). When the orbits of larger SMBH and clouds in its BLR have a smaller angle of pericenter, the plateaus between peaks of differential phases are less deformed (compare Fig. 5a). We turn now to the effects in the differential phase for various positions of SMBHs orbits in the orbital plane. Simulations for dif-

ferent combinations of variations of parameters revealed a wide range of distinct patterns (Fig. 5b). For simultaneous increase of observer angular position, SMBHs and clouds' orbital inclination, we observed a broadening of spectral lines and differential phases flattens and broadens. The more dramatic change of position of differential phase wings is associated with the change of longitude of ascending nodes of SMBHs between $230^\circ - 330^\circ$ (Fig. 5b).

3.2.2. CB-SMBH system with antialigned angular momenta

Next we look for the effects of retrograde orbital motion of clouds in the BLRs (i.e., $i_c > 90^\circ$) or equivalently with a general class of systems that satisfy the condition $\mathbf{J}_{bin} \cdot \mathbf{J}_{ci} < 0, i = 1, 2$. Predicted deformations of the differential phase shows two whirls from the opposite sides of the ridge specific for this kind of simulation (see the bottom left plot in Fig. A.2). The shape of whirls vary, depending on the values of the SMBHs and clouds longitudes of node and pericenter. More or less prominent additional deformation in the form of depression in the right wing of the surface appears (the bottom left plot in Fig. A.2). When this deformation is prominent, we can find specific double deformed S shape of differential phase as in Fig. D.2.

We consider the case when the CB-SMBH are coplanar while clouds in the BLR of less massive component have anti-aligned angular momenta. The inclinations of orbits of clouds are randomly distributed between 90° and 175° (see Figs. 6a-6c). Similarly to consideration of angle distributions of AGN in Subsect. 2.1, one can expect more frequently highly inclined clouds' orbits. This is a consequence of the form of distribution function for i_c which is given by $P(i_c)di_c = \sin i_c di$. From this one can see that the average i_c is about 45° . Moreover, *a priori* probability that $\sin i_c > \sin 45^\circ$ is about 87 percent.

The grid of models presented in Fig. 6a-6c shows that if a more substantial number parameters vary simultaneously, the shapes of differential phases will be more complicated. We can see that the central whirl has deformed wings because of larger ascending node and pericenter ($> \pi/2$) of SMBHs and clouds orbits as well for highly inclined clouds' orbital motion (see Figs. 6a-6c). Based on the theory of orbital motion, the variation of orbital nodes is influenced only by perturbations that are normal to the orbital plane. For example, in the case of a spinning SMBH, there may be rocket effect orthogonal to the orbital plane (see Redmount and Rees 1989).

Similarly to simulations of non-uniformly elongated clouds' orbits in the case of single SMBH (see Subsection 3.1), we consider the same skewed distributions (Γ_s and Rayleigh \mathcal{R}) of clouds' eccentricities in both BLRs of CB-SMBH system. A general prediction of \mathcal{R} distribution effects on the differential phase over the grid of the ascending node and the true anomaly of more massive SMBH is given in the bottom right plot of Fig. A.2. We observe a rough and unsmooth surface because of the randomly sampled clouds orbital eccentricities from Rayleigh distribution. Detailed Fig. 7a summarizes simulations for different combinations of Rayleigh distribution of clouds' eccentricities and fixed SMBHs and clouds other orbital parameters. We performed simulations separately for $\Gamma_s(0.3, 1)$ distribution of clouds orbital eccentricities. The differential phases are smooth but with subtle differences to the previous case. The central part of differential phase is depressed for coplanar clouds' motion in both BLRs (see Fig. 7b). For fixed orbital eccentricities of clouds ($e = 0.5$) around larger SMBH, irrespective of the coplanarity of their orbital planes, the right wing of differential phase is promi-

nent (Figs. 7b). It seems that subtle distinctions between orbital characteristics of clouds' motion could be important rather than to assume they are broadly similar.

More extensive atlas of expected interferometric observables probing the elliptical configuration of anti-aligned CB-SMBH systems is given in Appendix D. We summarize the results for the simulation in Table 3 that reports the effects of orbital parameters of the aligned and anti-aligned CB-SMBH system on the differential phase curves. The overall impact on the differential phase is more significant than for the single SMBH case presented in Table 2. We point out the following two effects. Eccentricities of SMBHs orbits, together with SMBH orbital orientation angles, complicate differential phase curves so that even double S-like shapes can appear.

4. Discussion

In this work, we probed the detection of interferometric signatures of single SMBH and CB-SMBH systems with elliptical orbital configurations. The differential phase was computed at the wavelength of Pa α spectral line. As expected, these signatures in differential phases occur under specific conditions, and their diagnostic potential is more evident for some parameters than for others. To quantify this, we calculated the evolution of the spectral line and differential phase as a function of wavelength and radial velocity for distinct sets of models. Further discussion focuses on three points: anticipated results for specific objects-which can be crucial to observers, the limitations of the present model in the light of selections of future observational targets and the information loss because of random cloud's motion.

4.1. Anticipated results for future observations

The results of simulations also show interesting qualitative similarities of some synthetic Pa α lines with those observed and reported in the literature. The corresponding differential phases might be used as a starting point to predict what would be the interferometric signatures of these specific targets.

Type 1 AGN and single SMBH models expected signatures
With single SMBH models, more or less asymmetric synthetic flat top lines given in Fig. 3a and 3b show similar gradients and shapes with flat top lines reported in the literature by Landt et al. (2014, see their Fig. 2) for IRAS 1750-508, PDS 456, PG 0026+129, Mrk 335. These objects are classified as type 1 AGN. Their expected differential phases could be of S-form for single SMBH, but with asymmetric amplitudes and widths of peaks implicating elongated cloud' orbits. Furthermore, the sharpness of the differential phases peaks became more prominent as Ω_c or ω_c is increased. The spectral line in Fig. 3c resembles Pa α line of SDSSJ05530.0-0.85704.0 (Kim et al. 2010), which is also type 1 AGN. Here anticipated differential phase would be broader as inclination position of the observer is larger, the sharpness of differential phases is more prominent than in the previous case, because of larger $\omega_c = 200^\circ$ and slightly more inclined cloud orbits. Similarly, in the third series of plots of Fig. B.3, the evolution of observables is peculiar. Here, models keep orbital eccentricity of clouds constant but vary the inclination angle from $i = 5^\circ$ to $i = 40^\circ$. We see that amplitude changes of phases are prominent and the position of maxima of phases, which gives an additional tool for interpreting the observations.

The blue lines reported in Figs. 1Ba-3b, 2Ba and 3Ba show the profiles in the waveform with a more prominent left peak. A comparable pattern was found in PG 0844+349 (Landt et al.

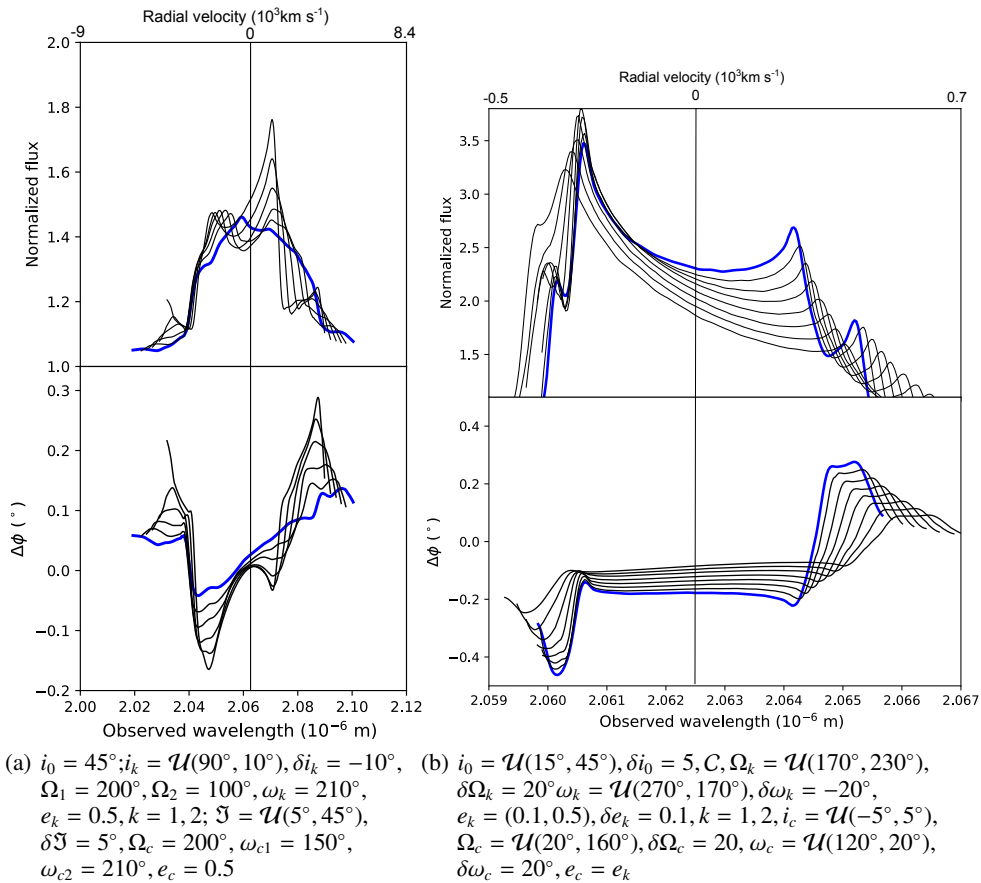


Fig. 5. Evolution of the Pa α emission line (upper subplots) and corresponding differential phase ($\Delta\phi$, lower subplots) as a function of the wavelength for different values of model parameters for aligned CB-SMBH system. Orbital elements that are the same for all clouds in both BLR are designed by subscript c. Varying parameters are listed in sub-captions, C stands for the coplanar CB-SMBH system.

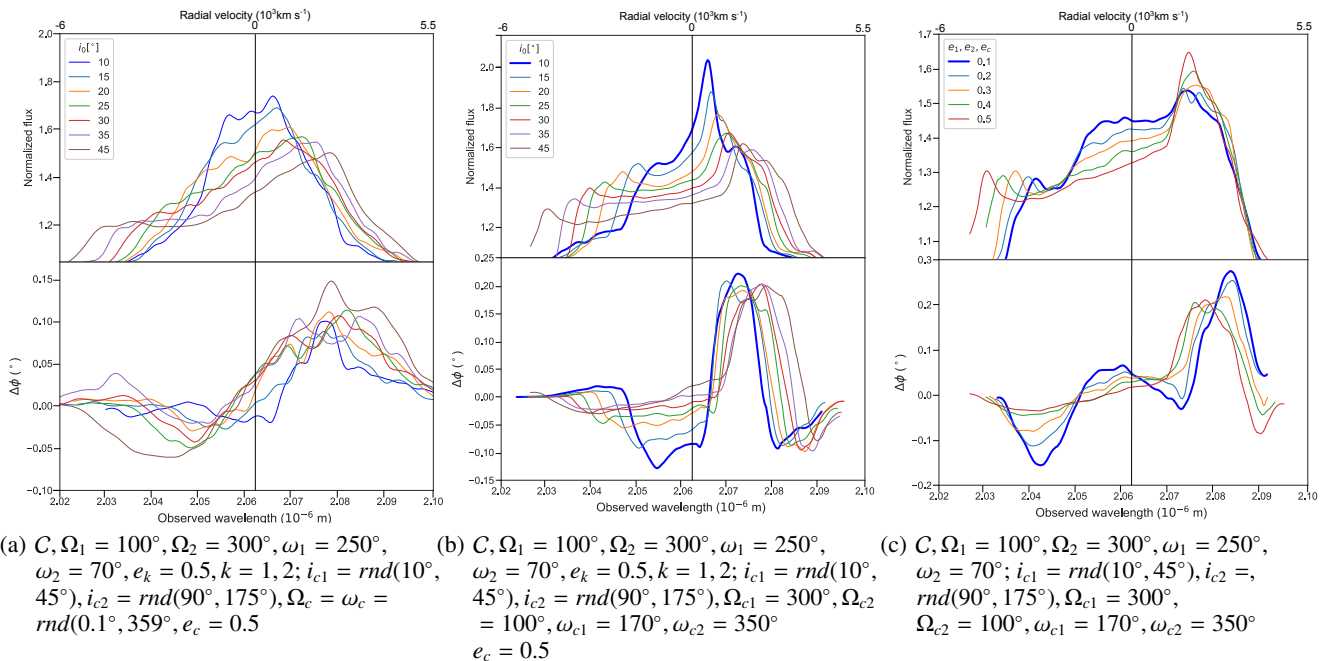


Fig. 6. Same as Fig. 5 but for anti-aligned angular momenta of clouds in the BLR of less massive SMBH.

2014, see their Fig. A2). It suggests that predicted differential phases are deformed, when either Ω_c or ω_c reaches minimal value of $\sim 10^\circ$. The width of the phase increases with increase in clouds' orbital inclinations. We find that at this wavelength, there is a clear signal in the differential phase for different pa-

rameters. In general, single SMBH produces differential phases that are more or less symmetric relative to the core of spectral lines depending on the excitation of eccentricity and parameters controlling the position of clouds orbit.

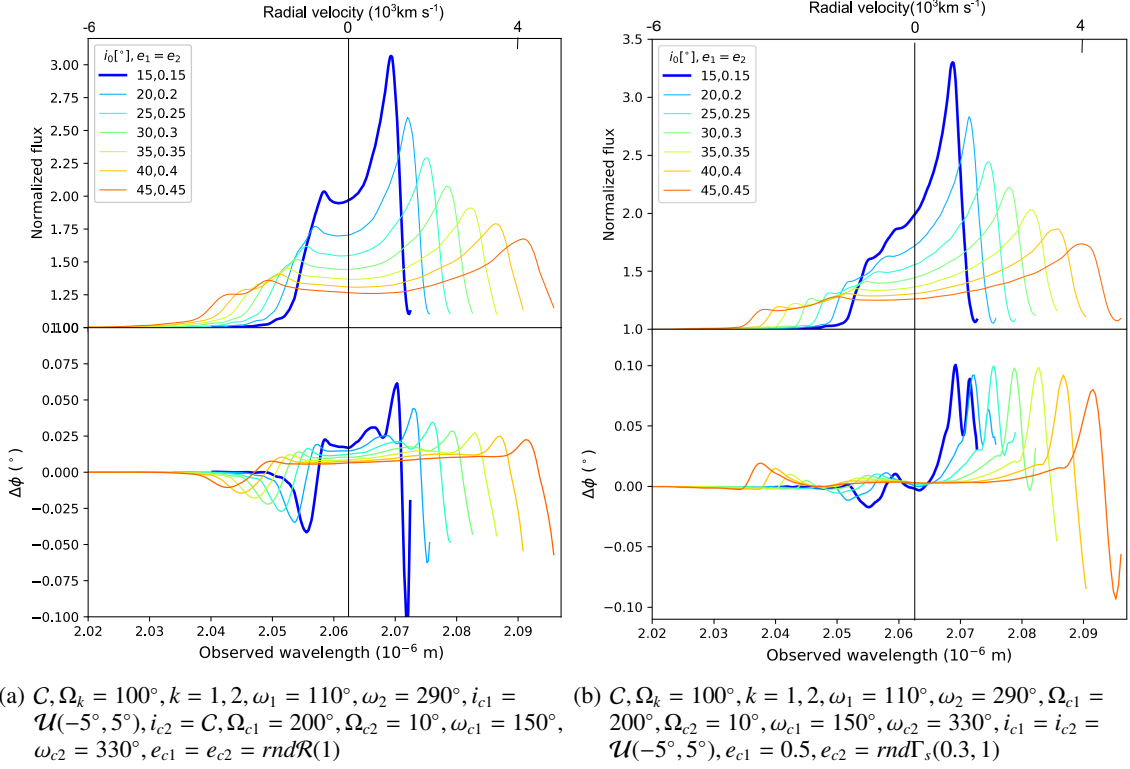


Fig. 7. Evolution of the Pa α emission line (upper subplots) and corresponding differential phase ($\Delta\phi$, lower subplots) as a function of the wavelength for aligned CB-SMBH system when clouds orbital eccentricities are drawn from non-uniform distributions. (a) clouds orbital eccentricities are drawn from Rayleigh distribution (b) clouds orbital eccentricities are drawn from scaled and shifted $\Gamma_s(0.3, 1)$ distribution.

Table 3. Qualitative summary of simulation parameters effects on the morphology of differential phase (DP) curves for CB-SMBH systems. The columns are: CB-SMBH and clouds' orbital and auxiliary parameters; range or monotony of parameters used in simulations; the effects on DP amplitude, its central part, wings, and slope, respectively.

Orbital elements	Range or monotony	Amplitude	central part	wings	slope
(e_1, e_2)	(increasing, increasing)	decreasing		deforming	
(e_{c1}, e_{c2})	$(\mathcal{R}(1), \mathcal{R}(1))$	decreasing and noise		deforming and noise	
$(e_{c1}, e_{c2}, i_{ck}, k = 1, 2)$	$(\Gamma_s(0.3, 1), \Gamma_s(0.3, 1), C)$	smooth	depressed	smooth	
$(e_{c1}, e_{c2}, i_{c1}, i_{c2})$	$(\Gamma_s(0.3, 1), \Gamma_s(0.3, 1), C, -C)$	smooth and decreasing		smooth	
$(e_{c1}, e_{c2}, k = 1, 2)$	$(0.5, \Gamma_s(0.3, 1), C)$	smooth		prominent right wing	
$(\Omega_k, \omega_k, k = 1, 2)$	$> \pi/2$		deforming		
$(i_k, k = 1, 2)$	increasing				decreasing
$(i_{ck}, k = 1, 2)$	increasing	$(0^\circ, 45^\circ)$			decreasing
$\mathbf{J}_k^c, k = 1, 2$	$\mathbf{J}_{bin} \cdot \mathbf{J}_k^c < 0^a$		central whirl		
Auxiliary parameters					
i_0	increasing	decrease	decrease		

Notes. ^(a) Conditions: $\mathbf{J}_{bin} \cdot \mathbf{J}_k^c > 0$ is equivalent to clouds orbital inclinations less than 90° ; $\mathbf{J}_{bin} \cdot \mathbf{J}_k^c < 0$ is equivalent to clouds orbital inclinations larger than 90° .

Type 1 AGN (NLSy1, quasars) and aligned CB-SMBH models expected signatures

Two SMBH and their BLRs induce more rich and complex differential phase patterns. There are many configurations for which the aligned CB-SMBH differs among themselves and to single SMBH. Features of synthetic spectra given in Figs. 2C b and 2C c show similarity with those found in 3C 390.3 (Landt et al. 2014, see their Fig. A1). This object is well known as a double-peaked line emitter in the optical band. The double-peaked profiles can be also associated with accretion disc emission (Eracleous and Halpern 1994, 2003; Gezari et al 2007). But, if the binary model is appropriate for this object, then asso-

ciated differential phases will have a complex double S-shaped structure. This model reflect the possibility of a non-coplanar CB-SMBH, with highly inclined orbits of clouds in both BLRs. If a single SMBH model with a BLR d of 95 light days is true (see Shapovalova et al. 2010b) a differential signal would be 0.9° . Even that spectral lines of objects can share some characteristics, our model predicts that corresponding differential phases are distinct because of different SMBH and clouds orbital parameters. The optically bright quasar PG 1211+143 (Landt et al. 2014) has a convex Pa α shape slightly depressed of the center, as in our synthetic case present in Fig. 2C a. The predicted differential phase would resemble asymmetric double S shape,

caused by non-coplanarity of the CB-SMBH system and high values of clouds orbital elements Ω_c and ω_c . Moreover, the high rise spectral line in Fig. 5a is also observed in the spectrum of SDSSJ032213.8+005513.4 (Kim et al. 2010, see their Fig. 1). If the CB-SMBH model is appropriate for this object, then the expected differential phase would be similar in morphology with the previous case but distinct in their details because of different values of Ω_2 . In addition, asymmetric two horn feature (blue line) found in Fig. 3C b, is also highly consistent with observed line in Mrk 79 (Landt et al. 2008, see their Fig. 13). Anticipated differential phases differ from those seen in previous cases because of large values $230^\circ < \Omega_1, \Omega_2 < 330^\circ$ and the decreasing $\omega_k, k = 1, 2$.

Type 1 AGN (binary black hole candidates, quasars) and anti-aligned CB-SMBH models expected signatures

Significant changes in differential phases shape for anti-aligned CB-SMBH, are given in Fig. 6a. The spectral line marked as a blue curve in Fig. 6b is like Pa α line in SDSSJ01530.0-085704.0 (see Fig. 2 in Kim et al. 2010), and in NGC 7469 (see Fig. 13 in Landt et al. 2008, black line). The expected differential phase for these two objects would have complex double S shape with prominent wings, which is a consequence of anti-aligned orbital angular momenta of clouds in the second BLR and randomized Ω_c of clouds orbits in both BLRs. Even double peaks in simulated spectral line merge for larger inclinations of the CB-SMBH system, differential phases preserve more or less deformed double S shape. In the core of NGC 7469, there is a dust torus at a distance of 65-87 light days from central engine, based on K-band time lags (Sugunama et al. 2006). Thus, expected differential phases could be of the order of $2.17^\circ - 3.04^\circ$. However, the peculiar spectral line (blue model) in Fig. 6c with convex core resembles Pa α line observed in the binary black hole candidate NGC 4151 (see Fig. 4 in Landt et al. 2008). Here, the expected differential phase has a smaller central part and prominent right wing, caused by anti-aligned orbital angular momenta of clouds in the second BLR. But Ω_c of cloud orbits in both BLRs are not randomized. This object, located at 19 Mpc, is among the nearest galaxies that contains an actively growing black hole (Wang et al. 2010). Its proximity and claimed evidence for the first spectroscopically resolved sub-parsec CB-SMBH (Bon et al. 2012) offer one of the best chances also for interferometric studies. Bon et al. (2012) found CB-SMBH to have eccentric orbit $e \sim 0.4$ with period of 15.2 years, argument of longitude of pericenter $\omega \sim 95^\circ$, semi-major axes of $(a_1 + a_2) \sin i \sim 0.002 + 0.008$ pc, and masses of components $M_1 \sim 3 \times 10^7 M_\odot$, $M_2 \sim 8.5 \times 10^6 M_\odot$.

These results imply that the expected signal in the differential phase would be of the order $\sim 0.5^\circ$ using Eq. 13. CB-SMBH with a small orbital period of the order of 1 yr, as discussed in the next subsection 4.2, we will be able to observe them at different orbital phases. Fig. D.4 shows a set of models depicting interferometric observables calculated at three different CB-SMBH orbital phases $\Theta(t) = 0, 0.25, 0.5$ where $\Theta(t) = \frac{t-\tau}{P}$, t is time, τ is time of pericenter passage and P is a binary period. Interferometric observables appeared to be unfavorable in all the cases. However, careful inspection shows that interferometric signal varies with orbital phase (i.e., time). These synthetic spectral lines look like those observed in PG 1307+085, PG 0804+761, PG 1211+143, PG 0026+129 (Landt et al. 2014). In summary, we show that using differential phases morphology can help us distinguish between models. Though some spectral lines of single SMBH can be morphologically indistinguishable from those in CB-SMBH, their differential phases differ in various manners,

and they are likely to be one of the essential tools for CB-SMBH detection.

4.2. Limitation of present model

In our model we assumed that the CB-SMBH orbital period is longer than the dynamical timescale of each BLR, which holds for separated BLRs. In opposite the orbital motion of SMBHs will perturb the BLRs, complicating line profiles and phase curves. For example, periodic flares in the light curves of OJ 287 have been successfully predicted by the model of the secondary impacting the accretion disc of the primary SMBH, twice during one orbit (Laine et al. 2020).

We assumed the physical parameters of the BLRs emissivity and clouds motion as an unaltered if the orbital period is longer than observational time-baseline. But, if the orbital period of the binary system is of the order of a time baseline of observation, e.g. ~ 1 year orbital period in the photometric light curve of Mrk 231 (Kovačević et al. 2020), then these quantities can differ from being invariant.

If the CB-SMBH merged to a later phase, a viable way of overcoming the 'final parsec problem' is interaction with a disc surrounding binary (see, e.g. Armitage and Natarajan 2005; MacFadyen and Milosavljević 2008). Dissipative torques could align the circumbinary disc plane with the binary orbital plane while circumbinary disc is rotating in the same sense as the binary (aligned angular momenta). Detailed simulations (see, e.g. Hayasaki et al. 2008) showed that such triple-disc CB-SMBH systems have tidally deformed BLR discs by the time-varying binary potential because of the orbital eccentricity. Also Lodato et al. (2009) show that tidal interaction could transform circumbinary disc into a decretion regime, which removes angular momentum outward, but with small inward mass transfer. This could prevent the binary separation from reducing to the 10^{-2} pc. However, it is highly likely that at some point, there will be a retrograde coplanar disc surrounding the binary, remaining in accretion mode. Material from such disc is gravitationally captured by the binary while reducing its angular momentum. Then the eccentricity threshold between the circular and non-circular binary system is determined by the surface density distribution of the circumbinary disc (see e.g. Nixon et al. 2011, and references therein). Wang et al. (2020b) explained recent ALMA observation of counter-rotating disc surrounding the core of NGC 1068 as a binary system with a counter-rotating circumnuclear disc. Also, ALMA observed a gas hole in the core of NGC 1365, NGC 1566, and NGC 1672 (Combes et al. 2019). Similar observations are expected to resolve the signatures of counter-rotating circumnuclear discs.

Also, we supposed both components in CB-SMBH to have same a non-negligible Eddington ratio ($\lambda_{Edd} \sim 0.1$). However, if luminosity variations are much smaller ($\lambda_{Edd} \lesssim 0.01$), then we can expect a small periodically varying flux component with an amplitude proportional to the black hole mass M_\bullet (Haiman et al. 2009)

$$\sim \frac{\lambda_{Edd}}{0.01} \left(\frac{M_\bullet}{3 \cdot 10^7 M_\odot} \right) \times 10^{-15} \text{ erg s}^{-1} \text{ cm}^{-2},$$

so that object would be too faint for analysis.

Regarding near-infrared observables, they might be detectable if a dusty torus surrounds the binary core. For example, geometrically thick BLR of single SMBH in 3C 273 detected by the GRAVITY is roughly consistent with dusty torus (Zhang et al. 2019). Thus torus inner edge would be irradiated by, and thus mirror, the variable central UV and X-ray sources.

Estimated error of the differential phase ($\delta\sigma_\phi$), can be obtained from Eq. 13 as a function of errors on the fluxes of both components ($\delta F_i, i = 1, 2$) and $\delta\sigma_i, i = 1, 2$ (Eq. A.4):

$$\delta\sigma_\phi \sim \frac{\frac{\delta F_1}{F_1}\sigma_1 + \delta\sigma_1 - \frac{\delta F_2}{F_2}\sigma_2 + \frac{F_2}{F_1}\delta\sigma_2}{1 + \frac{F_2}{F_1}} \quad (16)$$

To estimate contribution of terms in the error budget, we first consider that larger component is dominant in CB-SMBH $\frac{F_2}{F_1} \ll 1$ implying that also $\frac{\delta F_2}{F_2} \ll 1$. Then Eq.16 simplifies to

$$\delta\sigma_\phi \sim \frac{\delta F_1}{F_1}\sigma_1 + \delta\sigma_1 \quad (17)$$

Taking into account that $\frac{\delta F_1}{F_1} \sim 0.05(5\%)$, the angular scale of nearby CB-SBHBs is $\sim o(10\mu as)$, measured photocenter offset by GRAVITY, and that $\delta\sigma_1 \sim o(1\mu as)$ is of the order of precision of GRAVITY photocenter offset measurement of 3C 273, we get

$$\delta\sigma_\phi \sim 0.05\sigma_1 + o(1\mu as) \sim 0.05o(10\mu as) + o(1\mu as)$$

. We see that differential phase error is dominated by photocenter offset measurement of the more massive component. However, if $\frac{F_2}{F_1} \sim 1$ then

$$\delta\sigma_\phi \sim 0.025(\sigma_1 - \sigma_2) + \frac{\delta(\sigma_1 - \sigma_2)}{2} \sim 0.025o(10\mu as) + 0.5o(1\mu as)$$

, which is smaller than previous estimate. But we did not consider the sources of noise such as the photon noise, the background thermal noise and the detector readout noise. A crude analysis of Eq. 13 suggests that the cadence of fluxes of both BLRs and photocenter offset measurements are crucial for a well-sampled differential phase curve. Also, we assumed that the object wavelength dependence is only because of the variation of the fluxes of both BLRs. If the object intensity distribution depends on the wavelength in a more sophisticated way, the changes of the phase arise because of effects from the spatial frequency variation and the wavelength dependency of the object.

4.3. Differential phase loss of information

Interferometric signals decorrelate (become incoherent) due to either instrumental and/or physical characteristics of observed object such as random motion of clouds in the BLR (see analysis in Songsheng et al. 2019b). The differential phase curve becomes sensitive to the numbers of the clockwise and counter-clockwise rotating clouds in the BLR, which is essential for GRAVITY measurements of the BLR.

Information loss can be explained by moments introduced in Subsection 2.2. Namely, if the velocity distributions of clockwise and counter-clockwise moving clouds resemble roughly $N(0, \sigma^2)$, then the differential phase as the first-order moment (barycenter) will be zero. In turn, the second-order moment of such distribution will be $\sim \sigma^2 \neq 0$. If the disordered motion of clouds in the BLRs comes from turbulence (see Pancoast et al. 2014) then information recovered from the second-order moment would correspond to the parameter of distribution of turbulence velocity field $\sim \sigma^2 = \sigma_{turb}^2$. Thus higher-order moments can contain interferometric information.

5. Conclusions

We used the interferometry-oriented model described here, to estimate signatures of the elliptical orbital motion of clouds in the BLR of a single SMBH and elliptical orbital setup of CB-SMBH on spectro-interferometric observables. Besides, we investigate how these observables evolve with a variety of different combinations of orbital and geometrical parameters. Important findings and conclusions are summarized as follows:

1. The differential phases 'zoo' for a single SMBH comprises deformed but still recognizable S shape, indicating rotational and asymmetrical motion of clouds in BLR. We showed the evolution of differential phase shape, amplitude and slope with various sets of cloud orbital parameters and observer position. These maps can be useful for extracting exceptional features of the BLR structure from future high-resolution observations.
2. We found various deviations from the canonical S-shaped phases profile for elliptically configured CB-SMBH systems. There are notable differences between differential phases 'zoo' of single SMBH and CB-SMBH systems. The differential phases of CB-SMBH look as two blended and deformed S-shaped signals, asymmetrical about line center, which variability depend on the orbital motion of clouds and SMBHs.
3. The shape and amplitude of the phases of CB-SMBH systems depend on presumably orbital characteristics of SMBHs and clouds in their BLRs. Among the many sets of model parameters explored, we found that the signal is sensitive to the position of orbital nodes, inclinations, eccentricities, and argument of pericenter along with standardly expected effects of geometrical inclination of an observer. The right-skewed distributions of clouds orbital eccentricities cause noise effects in the form of small random fluctuations in the differential phase curve. We found some examples of synthetic spectral lines of a single SMBH, which are indistinguishable from those obtained from the CB-SMBH system, but with differing differential phases. Thus, the differential phases are markers for identifying signals of CB-SMBH.
4. Observationally, the variability of the differential phase is most substantial for lower inclinations of an observer. As much as the central part of the spectral lines is disfigured, the net effect is that the differential phase peaks move away from the line center. The plateau between differential phase peaks is more prominent. The opposite is valid when there are higher contributions of projected lower velocities in spectral lines. The reversed situation is occurring when line peaks are closer together, then differential phase peaks move closer to the center of the line.
5. The velocity distributions for anti-aligned clouds' orbital momenta in CB-SMBH show elongated features that are strained by the surface of positions of clouds. Velocity fields manifest in the closed surface, preserving topological volume and spatial coherency. We also tested the cases of randomly distributed inclinations, but the velocity fields of such BLRs are not volume-preserving in the topological sense. For synchronous alignment of angular momenta of the BLR clouds, the absolute value of clouds' velocities increases toward outer side lobes of disc-like BLRs. For anti-aligned BLRs, the absolute value of velocity increases toward sections close to apocenter and pericenter.

Acknowledgements. The authors gratefully acknowledge valuable comments and suggestions of the Reviewer, which helped us to improve and clarify our

work. AK and LCP are supported by Ministry of Education, Science and Technological development of Republic Serbia through the *Astrophysical Spectroscopy of Extragalactic Objects* project number 176001. JMW and YYS are supported by *National Key R&D Program of China* through grant 2016YFA0400701, by NSF through grants NSFC-11991050, -11873048, and by Grant QYZD-SSW-SLH007 from the *Key Research Program of Frontier Sciences, CAS*, by the *Strategic Priority Research Program of the Chinese Academy of Sciences* grant no. XDB23010400.

References

- Gravity Collaboration, Abuter, R., Accardo, M., Amorim, A., Anugu, N., Ávila, G. et al., 2017, *A&A*, 602, id. A94
- Event Horizon Telescope collaboration Akiyama K., et al. 2019, *ApJL*, 875, L1
- Armitage P. J. Natarajan P. 2005, *ApJ*, 634, 921
- Artymowicz, P., Lubow, S. H. 1996, *ApJ*, 467, L77
- Barth, A. J., Pancoast, A., Thorman, S. J. et al. 2011, *ApJ*, 743, 4
- Barth, A. J., Pancoast, A., Bennert, V. N. et al. 2013, *ApJ*, 769, 128
- Barth, A. J., Bennert, V. N., Canalizo, G. et al. 2015, *ApJS*, 217, 26
- Begelman, M. C., Blandford, R. D., Rees, M. J. 1990, *Nature* 287, 307
- Bentz, M. C., Walsh, J. L., Barth, A. J. et al. 2008, *ApJL*, 689, L21
- Bentz, M. C., Walsh, J. L., Barth, A. J. et al. 2009, *ApJ*, 705, 199
- Bon, E., Jovanović, P., Marziani, P., Shapovalova, A. I., Bon, N., Borka - Jovanović, V., Borka, D., Sulentic, J., Popović, L. Č. 2012, *ApJ*, 759, id. 118, 9
- Colpi, M., Mayer, L., Governato, F. 1999, *ApJ*, 525, 720
- Combes, F., García-Burillo, S., Audibert, A., Eckart, A., et al. 2019, *A&A*, 623, A79
- Cuadra, J., Armitage, P. J., Alexander, R. D., Begelman, M.C. 2009, *MNRAS*, 393, 1423
- Delaa, O. Zorec, J., Domiciano de Souza, D., Mourard, D., Perrau, K., et al. 2013, *A&A*, 555, A100
- Denney, K. D., Peterson, B. M., Pogge, R. W. et al. 2009, *ApJL*, 704, L80
- Domiciano de Souza, A., Zorec, J., Jankov, S., et al. 2004, *A&A*, 418, 781
- Du, P., Hu, C., Lu, K.-X., Wang, F., Qui, J., Li, Y.-R., Bai, J.-M., Kaspi, S., Netzer, H., Wang, J.-M. 2014, *ApJ*, 782, 45
- Du, P., Hu, C., Lu, K.-X., Huang, Y.-K., Cheng, C., Qiu, J., Li, Y.-R., et al. 2015, *ApJ*, 806, 22
- Du, P., Lu, K.-X., Zhang, Z.-X., Huang, Y.-K., Wang, K., Hu, C., Qiu, J., Li, Y.-R. et al. 2016, *ApJ*, 825, 126
- Du, P., Brotherton, M. S., Wang, K., Huang, Z.-P., Hu, C., Kasper, D. H., Chick, W. T. et al. 2018, *ApJ*, 869, id. 142
- Du, P., Zhang, Z.-X., Wang, K., Huang, Y.-K., Zhang, Y., Lu, K.-X., Hu, C., Li, Y.-R. et al. 2018, *ApJ*, 856, 6
- Edelson, R., Gelbord, J., Cackett, E., Peterson, B. M., Horne, K., Barth, A. J. et al. 2019, *ApJ*, 870, 2, id. 123
- Elvis, M., 2001, in *The Century of Space Science* (eds J.A. Bleeker, J. Geiss, and M. Huber), Kluwer Academic Publishers, 529
- Eracleous, M., Halpern, J. P. 1994, *ApJS*, 90, 1
- Eracleous, M., Halpern, J. P. 2003, *ApJ*, 599, 886
- Gezari, S., Halpern, J. P., Eracleous, M. 2007, *ApJS*, 169, 167
- Grier, C. J., Peterson, B. M., Pogge, R. W. et al. 2012, *ApJ*, 755, 60
- Grier, C. J., Trump, J. R., Shen, Y. et al. 2017, *ApJ*, 851, 21
- Haiman, Z., Kocsis, B., Menou, K. 2009, *ApJ*, 700, 1952
- Hayasaki, K., Mineshige, S., Ho, L. C. 2008, *ApJ*, 682, 1134
- Hopkins, P. F., Hernquist, L., Cox, T. J., Di Matteo, T., Robertson, B., Springel, V. 2006, *ApJS*, 163, 1
- Ilić, D., Oknyansky, V., Popović, L. Č., Tsygankov, S. S., Belinski, A. A., Tatarnikov, A. M., Dodin, A. V., Shatsky, N. I., Ikonnikova, N. P., Rakić, N., Kovačević, A., Marčeta-Mandić, S. et al. 2020, accepted in *A&A*
- Jaffe, W., Meisenheimer, K., Röttgering, H. J. A., Leinert, Ch., Richichi, A. et al. 2004, *Nature*, 429, 6987, 47
- Jankov, S., Vakili, F., Domiciano de Souza Jr., A., Janot-Pacheco, E. 2001, *A&A*, 377, 721
- Kaspi, S., Smith, P. S., Netzer, H. et al. 2000, *ApJ*, 533, 631
- Kaspi, S., Brandt, W. N., Maoz, D. et al. 2007, *ApJ*, 659, 997
- Kim, D., Im, M., Kim, M. 2010, *ApJ*, 724, 386
- Kishimoto, M., Hönig, S. F., Antonucci, R., Kotani, T., Barvainis, R., Tristram, K. R. W., Weigelt, G. 2009, *A&A*, 507, L57
- Klioner, S. 2003, *ApJ*, 125, 1580
- Kovačević, A., Wang, J.-M., Popović, L. Č. 2020, *A&A*, 635, id. A1, 19
- Kovačević, A. B., Yi, T., Dai, X., Yang, X., Čvorović-Hajdinjak, I., Popović, L. Č. 2020, *MNRAS*, 494, 4069
- Krause, M., Burkert, A., Schartmann, M. 2011, *MNRAS*, 411, 550
- Laine, S., Dey, L., Valtonen, M., Gopakumar, A., Zola, S., Komossa, S. et al. 2020, *ApJL* 894 L1
- Landt, H., Ward, M. J., Elvis, M., Karovska, M. 2014, *MNRAS*, 439, 1051
- Landt, H., Ward, M. J., Peterson, B. M., Bentz, M. 2013, *MNRAS*, 432, 113
- Landt, H., Bentz, M. C., Ward, M. J., Elvis, M., Peterson, B. M., et al. 2008, *ApJS*, 174, 282
- Lodato, G., Nayakshin, S., King, A. R., Pringle, J. E. 2009, *MNRAS*, 398, 1392
- Lachaume, R., 2003, *A&A*, 400, 795
- Lu, K.-X., Bai, J.-M., Zhang, Z.-X., Du, P., Hu, C., Kim, M., Wang, J.-M., Ho, L. C., Li, Y.-R. et al. 2019, *ApJ*, 887, id. 13
- MacFadyen, A. I. Milosavljević, M. 2008, *ApJ*, 672, 83
- Mayer, L., Kazantzidis, S., Madau, P., Colpi, M., Quinn, T., Wadsley, J. 2007, *Science*, 316, 1874
- Meilland, A., Delaa, O., Stee, Ph., Kanaan, S., Millour, F. et al., 2011, *A&A* 532, A80
- Netzer, H. 2013, *The physics and evolution of active galactic nuclei*, Cambridge university press
- Nixon, C. J., Cossins, P. J., King, A. R., Pringle, J. E. 2011, *MNRAS*, 412, 1591
- Pancoast, A., Brewer, B. J., Treu, T. 2014, *MNRAS*, 445, 3055
- Pancoast, A., Skielboe, A., Pei, L., Bennert, V. N.; et al. 2019, *ApJ*, 871, id. 108
- Peters, P. C., Mathews, J. 1963, *Phys. Rev.*, 131, 435
- Peterson, B. M., Wanders, I., Bertram, R. et al. 1998, *ApJ*, 501, 82
- Peterson, B. M., Berlind, P., Bertram, R. et al. 2002, *ApJ*, 581, 197
- Peterson, B. M., Ferrarese, L., Gilbert, K. M., Kaspi, S. et al. 2004, *ApJ*, 613, 682
- Petrov, R. G., Malbet, F., Weigelt, G., Antonelli, P., Beckmann, U., Bresson, Y., et al. 2007, *A&A*, 464, 1
- Petrov, R. G., Millour, F., Lagarde, S., Vannier, M., Rakshit, S., Marconi, A., Weigelt, G., 2012, in *Proc. SPIE 8445, Optical and Infrared Interferometry III*, ed. F. Delplancke, J. K. Rajagopal, & F. Malbet, 84450W-1
- Petrov, R. G. 1989, in *Diffraction-Limited Imaging with Very Large Telescopes*, Proceedings of the NATO Advanced Study Institute, held in Cargèse, September 13-23, 1988, Dordrecht: Kluwer, 1989, edited by D. M. Alloin and J. M. Mariotti. NATO Advanced Science Institutes (ASI) Series C, 274, 249
- Popović, L. Č., Shapovalova, A. I., Ilić, D., Kovačević, A., Kollatschny, W. et al. 2011, *A&A*, 528, A130
- Popović, L. Č., Shapovalova, A. I., Ilić, D., Burenkov, A. N., Chavushyan, V. H., Kollatschny, W., Kovačević, A. et al. 2014, *A&A*, 572, A66
- Redmount, I. H., Rees, M. J. 1989, *Comments on Astrophys.*, 14, 165
- Roedig, C., Dotti, M., Sesana, A., Cuadra, J., Colpi, M. 2011, *MNRAS*, 415, 3033
- Safarzadeh, M., Loeb, A., Reid, M. 2019, *MNRAS*, 488, L90
- Sesana, A. 2010, *ApJ*, 719, 851
- Shapovalova, A. I., Burenkov, A. N., Carrasco, L., Chavushyan, V. H. et al. 2001, *A&A*, 376, 775
- Shapovalova, A. I., Doroshenko, V. T., Bochkarev, N. G., Burenkov, A. N. et al. 2004, *A&A*, 422, 92
- Shapovalova, A. I., Popović, L. Č., Collin, S., Burenkov, A. N. et al. 2008, *A&A*, 486, 99
- Shapovalova, A. I., Popović, L. Č., Burenkov, A. N., Chavushyan, V. H., Ilić, D., Kovačević, A. et al. 2010a, *A&A*, 509, A106
- Shapovalova, A. I., Popović, L. Č., Burenkov, A. N., Chavushyan, V. H., Ilić, D., Kollatschny, W., Kovačević, A. et al. 2010b, *A&A*, 517, A42
- Shapovalova, A. I., Popović, L. Č., Burenkov, A. N., Chavushyan, V. H., Ilić, D., Kovačević, A., Kollatschny, W., Kovačević, J. et al. 2012, *ApJS*, 202, 10
- Shapovalova, A. I., Popović, L. Č., Burenkov, A. N., Chavushyan, V. H., Ilić, D., Kollatschny, W., Kovačević, A. et al. 2013, *A&A*, 559, A10
- Shapovalova, A. I., Popović, L. Č., Chavushyan, V. H., Burenkov, A. N., Ilić, D., Kollatschny, W., Kovačević, A. et al. 2016, *ApJS*, 222, id. 25
- Shapovalova, Alla I., Popović, L. Č., Chavushyan, V. H., Afanasiev, V. L., Ilić, D., Kovačević, A. et al. 2017, *MNRAS*, 466, 4759
- Shapovalova, A. I., Popović, L. Č., Afanasiev, V. L., Ilić, D., Kovačević, A., Burenkov, A. N., Chavushyan, V. H., Marčeta-Mandić, S. et al. 2019, *MNRAS*, 485, 4790
- Shen, Y., Horne, K., Grier, C. J., Peterson, B. M., Denney, K. D. et al. 2016, *ApJ*, 818, 30
- Songsheng, Y. Y., Wang, J.-M., Li, Y.-R., Du, P. 2019a, *ApJ*, 881, 140
- Songsheng, Y. Y., Wang, J.-M., Li, Y.-R. 2019b, *ApJ*, 883, 184
- Songsheng, Y.-Y., Xiao, M., Wang, J.-M., Ho, L. C. 2020, *ApJS*, 247, 3
- Suganuma, M., Yoshii, Y., Kobayashi, Y., Minezaki, T., Enya, K. et al. 2006, *ApJ*, 639, 46 10.1086/499326
- Shull, J. M., Stevans, M., Danforth, C. W. 2012, *ApJ*, 752, 162
- Stern, J., Hennawi, J. F., Pott, J.-U. 2015, *ApJ*, 804, 57
- Gravity Collaboration, Sturm, E., Dexter, J., Pfulf, O., Stock, M. R., Davies, R. I., Lutz, D. et al. 2018, *Nature*, 563, 7733, 657
- Swain, M. R. 2004, in *Proceedings of SPIE Volume 5491*. Edited by Wesley A. Traub. Bellingham, WA: The International Society for Optical Engineering, 2004., 1
- Tokovinin, A. 1992, in *Proceedings of ESO Conference on High-Resolution Imaging by Interferometry II. Ground-Based Interferometry at Visible and Infrared Wavelengths*, Garching bei München, Germany, October 15-18, 1991. Editors, J.M. Beckers, F. Merkle, European Southern Observatory, Garching bei München, Germany, 425

- Vannier, M., Petrov, R. G., Lopez, B., Millour, F. 2006, *MNRAS*, 367, 825
- Waisberg, I., Dexter, J., Pfuhl, O., Abuter, R., Amorim, A., Anugu, N. et al 2017, *ApJ*, 844, 72
- Wanders, I., Goad, M. R., Korista, K. T., Peterson, B. M., Horne, K., Ferland, G. J., et al. 1995, *ApJL*, 453, L87
- Wang, J., Fabbiano, G., Risaliti, G., Elvis, M., et al. 2010, *ApJL*, 719, L208
- Wang, J.-M., Du, P., Hu, C., Netzer, H. et al. 2014, *ApJ*, 793, 108
- Wang, J.-M., Du, P., Brotherton, M. S., et al. 2017, *NatAs*, 1, 775
- Wang, J.-M., Songsheng, Y.-Y., Li, Y.-R., Du, P., Zhang, Z.-X. 2020a, *Nat. Astron.*, 4, 517
- Wang, J.-M., Songsheng, Y.-Y., Li, Y.-R., Du, P., Zhe, Y. 2020b, *MNRAS*, 497, 1020
- Wang, J.-M., Songsheng, Y.-Y., Li, Y.-R., Zhe, Y., 2018, *ApJ*, 862, 171
- Wang, J., Xu, D. W., Wei, J. Y. 2018, *ApJ*, 858, 49
- Weigelt, G., Hofmann, K.-H., Kishimoto, M., Hönig, S., Schertl, D. et al., 2012, *A&A*, 541, L9
- Zhang, Z. X., Du, P. Smith, P. S., Zhao, Y., Hu, C., Xiao, M., Li, Y. R., Huang, Y. H., Wang, K., Bai, J., M., Ho, L. C., Wang, J. M., 2019, *ApJ*, 876, 14

Appendix A: General inferences about differential phase based on a first order approximation

Appendix A.1: Single SMBH

First, we infer some generic patterns about differential phase shape, to assess more specific results of numerical simulations. We recall that spectral line of the source can be approximated as a function of the form $\Xi(\lambda, \mathbf{r}_k^c, \mathbf{V}_k^c)$ where $\mathbf{r}_k^c, \mathbf{V}_k^c$ are composite vector fields of the k -th cloud' position and velocity, given in SMBH centered coordinate system (see Kovačević et al. 2020). Considering a single-source model, a first-order approximation of $\xi(\lambda)$ based on Eq. 11 is:

$$\xi(\lambda) \sim \arctan \frac{\sin(2\pi \mathbf{u} \cdot \boldsymbol{\sigma})}{\cos(2\pi \mathbf{u} \cdot \boldsymbol{\sigma})} \sim \sin(2\pi \mathbf{u} \cdot \boldsymbol{\sigma}) \sim 2\pi \mathbf{u} \cdot \boldsymbol{\sigma} \quad (\text{A.1})$$

When $\mathbf{u} \cdot \boldsymbol{\sigma}$ gets smaller below the resolution limit, the phase tends to a linear expression as it is given by the third term in Eq. A.1 (Vannier et al. 2006). Thus the shape of the differential phase is defined by the projected vectorial field of positions of clouds. For non-resolved sources, the term $2\pi \mathbf{u} \cdot \boldsymbol{\sigma}$ never reaches the value of $\frac{\pi}{2}$ and the maximum value of phase occurs when $\mathbf{u} \cdot \boldsymbol{\sigma}$ is largest. Thus, the elements of clouds elliptical orbit appear in the scalar product:

$$\begin{aligned} \mathbf{u} \cdot \boldsymbol{\sigma} &= u \frac{r_c}{d} [\cos \Omega_c \cos(\omega_c + f_c) - \sin \Omega_c \sin(\omega_c + f_c) \cos i_c] \\ &+ v \frac{r_c}{d} [\sin \Omega_c \cos(\omega_c + f_c) + \cos \Omega_c \sin(\omega_c + f_c) \cos i_c] \end{aligned} \quad (\text{A.2})$$

where d is a distance between the observer and SMBH. The intensity of the radius vector of clouds' orbit is

$$r_c = \frac{a_c(1 - e_c^2)}{1 + e_c \cos f_c} \quad (\text{A.3})$$

where the true anomaly f_c is computed as outlined in Kovačević et al. (2020). Since we assume that the interferometric baseline is perpendicular to the rotation axis ($PA = 90^\circ$, see in Songsheng et al. 2019a, and references therein) then in our calculations will not appear second term containing v -coordinate of the vector \mathbf{u} .

Having defined quantity $\mathbf{u} \cdot \boldsymbol{\sigma}$ in terms of clouds orbital parameters and angular position of interferometric baseline, we will now move on to discuss the interactive effects of clouds orbital elements on the value of the first term in Eq. A.2 using surface plots. In Fig. A.1 upper left plot, we present the surface mesh for $\omega = \pi/3, i = \pi/3, e = 0.5, a = 15ld$ which is plotted over $\Omega - f$ grid. The surface is smooth with regions of local extrema and a central peak, but some slopes are skewed.

An increase in the surface's amplitude results from an increase of the eccentricity of clouds' orbits. This is evident even for smaller clouds' orbital inclinations (see Fig. A.1, bottom plot). An increasing clouds' orbital inclination causes peak slopes to decrease in the diagonal direction (see the red region in the upper left plot of Fig. A.1). Deformed side intersections have an S-like shape. The effects of fixed parameters $\omega = 4.66 \text{ rad}, f = 3.38 \text{ rad}, e = 0.19$ resemble a wavelike, or hilly, structure with S side profile (see Fig. A.1 upper left plot), but with deformed peaks (see red and blue regions).

It is useful, for presenting results that follow, to get an analytic estimate of the first term in Eq. A.2 for some specific values of model parameters. When clouds' orbital inclinations are $\sim 0^\circ$, the term becomes $\sim \frac{r_c}{d} \cos(\Omega + \omega + f)$. If $\Omega \sim 0^\circ$, the term turns into $\sim \frac{r_c}{d} \cos(\omega + f)$. At the initial time (i.e., $f = 0$), the term

becomes $\sim \frac{r_c}{d} \cos(\Omega) \cos(\omega) - \sin \Omega \sin(\omega) \cos i$. So its amplitude depends on values of Ω and ω , and having the largest values for smaller eccentricity (see Fig. A.1, bottom plot).

Let us explore the analytic forms under degenerate cases, when some orbital parameters are not defined. The simplest case is an inclined circular orbit for which we can not define f and ω . Then the so-called argument of latitude η is used and the first term becomes

$$\sim \frac{a}{d} \cos \Omega \cos \eta - \sin \Omega \sin \eta \cos i$$

. For circular orbits with zero inclination, the argument of latitude η is also undefined since the line of nodes is undetermined. Thus, the true longitude L can be used instead, so the first term asymptotically behaves as $\sim \frac{a}{d} \cos L$.

Appendix A.2: CB-SMBH

Let us take a brief look at Eq. 13 and describe some general effects of orbital elements of clouds in both BLR in a CB-SMBH system on characteristics of the composite differential phase of. For simplicity's sake, we omit fluxes $F_k, k = 1, 2$ in the following derivation:

$$\mathbf{u} \cdot (\boldsymbol{\sigma}_1 - \boldsymbol{\sigma}_2) \sim \mathbf{u} \cdot (\mathbf{r}_1^c - \mathbf{r}_{\bullet 1} - \mathbf{r}_2^c + \mathbf{r}_{\bullet 2}) \quad (\text{A.4})$$

where $\sigma_k, k = 1, 2$ are vectors of relative positions of clouds around k -th SMBH in the barycentric frame. The vector σ_k equals to the difference between SMBH barycentric position $\mathbf{r}_{\bullet k}$ and cloud barycentric positions \mathbf{r}_k^c for $k = 1, 2$. Similar to the case of a single SMBH, we calculate the surface mesh of approximate values of the composite differential phase (see Fig. A.2) using Eq. A.4. We plot it on a grid defined by orbital ascending node and the true anomaly of the more massive SMBH. To test the differential phase sensitivity to parameters, we varied the parameters' values from within their ranges as reported in Table A.1.

The calculated surface consists of two ridges and two valleys. The appearance of a complex system of ridges depends on eccentricities and ascending nodes of both SMBHs. If eccentricities of both SMBHs are smaller than 0.5, the second ridge would disappear. Moreover, orbital ascending nodes and angles of pericenter of both SMBHs affect the position and slope of ridges and valleys. The inclinations of SMBH orbits control the slopes of ridges, and the larger inclination values decrease slopes. The effects of clouds and SMBHs orbital elements are similar, but former effects are smaller. The system of ridges and valleys cause complicated differential phase shapes similar to the surface side intersections (upper and bottom left plots of Fig. A.2).

Appendix B: Atlas of interferometric observables for single SMBH

We present three atlases of observables assuming non-randomized motion. In the first series, shown in Fig. B.1, the clouds orbital inclinations have uniform distribution $i_c = \mathcal{U}(-5^\circ, 5^\circ)$. The evolutions of observables depicted in Fig. 1Ba are less dramatic than in Figs. 3a and 3b. Variation of i_0 shapes the evolution of both observables with largest effects seen when $\omega_c = 270^\circ$ (see Figs. 1Bb-1Bd). The left peak of the spectral line is more prominent when $\Omega_c, \omega_c \leq 180^\circ$ and $e_c > 0.3$, but the right peak dominates when $\omega_c = 270^\circ$. These two orbital parameters have a more significant influence on the amplitude of differential phase when eccentricity is smaller (Figs. 1Bb-1Bc).

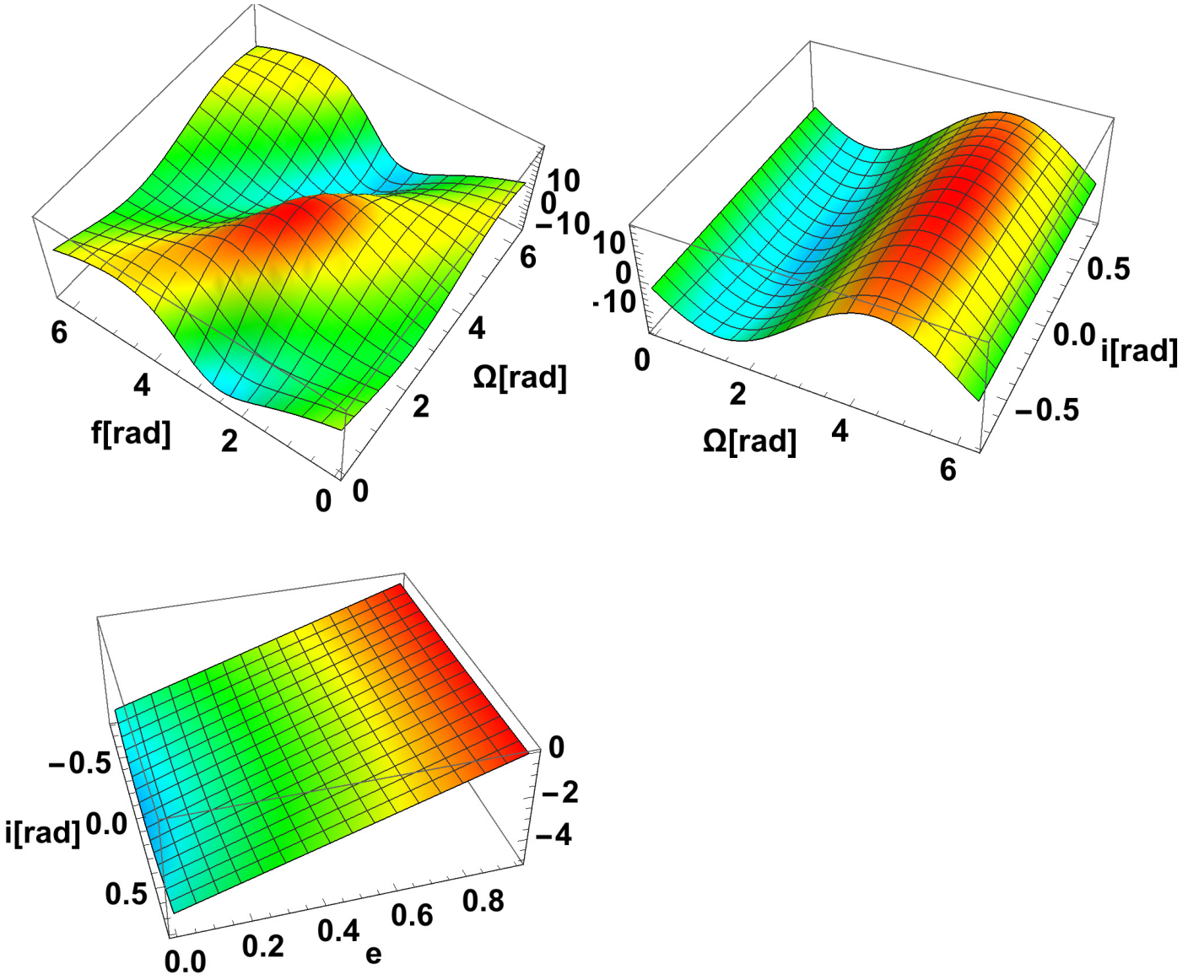


Fig. A.1. Interactive effects of clouds’ orbital elements on the values of the first parameter in Eq. A.2 present as the surface mesh. Upper left: on the x-axis is cloud’s ascending node Ω , on the y-axis is true anomaly (f), on the z-axis are values of the calculated parameter for fixed elements $\omega = \pi/3, i = \pi/3, e = 0.5, a = 15$ ld. Upper right: on the x-axis is cloud’s orbital inclination, and fixed elements are $\omega = 4.66$ rad, $f = 3.38$ rad, $e = 0.19$. Bottom plot: on the x-axis is eccentricity, and fixed elements are $\omega = 11\pi/18, \Omega = 10\pi/18, f = 0$ rad.

Notable net effects of both orbital shape angles are found when they have simultaneously larger values (compare Figs. 1Bc and 1Bd to Fig. 1Bb).

In the second series of plots (see Fig. B.2), simulations show the flat-topped spectra. An increase in clouds’ orbital inclination results in a decrease in the slope between two peaks of the differential phase (Figs. 2Ba- 2Bb). The inclination of the observer i_0 affects the slope of the differential phase similarly as clouds’ orbital inclination (see Fig. 2Bc). Also, an alternation of the amplitudes in the left and the right wing of differential phase occurs because of variation of the clouds’ orbital pericenter ω . Smaller ω causes larger amplitudes in the right wing of differential phases, while larger ω has the opposite effect (see Figs. B.1 and B.3). Also, Fig. 3Bc shows gradual evolution of the asymmetry of differential phases amplitudes for variation of the angle

of pericenter. The slight variation of the slope between the differential phase peaks occurs when $\omega \sim \pi$.

Finally, we compare the evolution of the spectral lines and differential phases for the two non-uniform clouds’ orbital eccentricity distributions (see Fig. B.4). When $\omega \lesssim 50^\circ$ and $i_0 < 30^\circ$ the spectral lines and differential phases are narrower. For coplanar cases, differential phases’ deformation occurs regarding an invariant point in its right wing (compare Figs. 4Bb, 4Bd, 4Bf versus Figs. 4Be, 4Bc).

Appendix C: Atlas of interferometric observables for aligned CB-SMBH

The typical differential interferometry data for CB-SMBH systems are presented in Figs. C.1-C.3 with partially resolved multi-

Table A.1. Parameter sets used in testing the differential phase sensitivity for CB-SMBH based on Eq. A.4. For clarity, subscripts of parameters that relate to SMBHs components are set to 1 and 2; and for clouds they are set to ci , $i = 1, 2$ indicating the clouds of respective BLRs of SMBHs.

(Aa) Case 1									
CB-SMBH parameters									
a_1 [AU]	e_1	ω_1 [rad]	i_1 [rad]	a_2 [AU]	e_2	Ω_2 [rad]	ω_2 [rad]	i_2 [rad]	
5	0.69	6	0.148	10	0.596	4.62	5	0.587	
Clouds parameters									
a_{c1} [AU]	e_{c1}	Ω_{c1} [rad]	ω_{c1} [rad]	i_{c1} [rad]	a_{c2} [AU]	e_2	Ω_{c2} [rad]	ω_{c2} [rad]	i_{c2} [rad]
1	0.77	4.71	4.6	0.1	1	0.428	6	4	0.7

(Ab) Case 2									
CB-SMBH parameters									
a_1 [AU]	e_1	ω_1 [rad]	i_1 [rad]	a_2 [AU]	e_2	Ω_2 [rad]	ω_2 [rad]	i_2 [rad]	
5	0.61	2.28	0.446	10	0.795	2.638	3	0.395	
Clouds parameters									
a_{c1} [AU]	e_{c1}	Ω_{c1} [rad]	ω_{c1} [rad]	i_{c1} [rad]	a_{c2} [AU]	e_2	Ω_{c2} [rad]	ω_{c2} [rad]	i_{c2} [rad]
1	0.77	3.82	2.66	0.43	1	0.65	3.58	4	-0.78

(Ac) Case 3									
CB-SMBH parameters									
a_1 [AU]	e_1	ω_1 [rad]	i_1 [rad]	a_2 [AU]	e_2	Ω_2 [rad]	ω_2 [rad]	i_2 [rad]	
5	0.66	0.01	0.0001	10	0.66	1.62	3	0.0001	
Clouds parameters									
a_{c1} [AU]	e_{c1}	Ω_{c1} [rad]	ω_{c1} [rad]	i_{c1} [rad]	a_{c2} [AU]	e_{c2}	Ω_{c2} [rad]	ω_{c2} [rad]	i_{c2} [rad]
1	0.33	1.81	2.66	2.33	1	0.249	1.96	4	2.75

(Ad) Case 4									
CB-SMBH parameters									
a_1 [AU]	e_1	ω_1 [rad]	i_1 [rad]	a_2 [AU]	e_2	Ω_2 [rad]	ω_2 [rad]	i_2 [rad]	
5	0.786	5.68	0.0001	10	0.836	5.32	3	0.0001	
Clouds parameters									
a_{c1} [AU]	e_{c1}	Ω_{c1} [rad]	ω_{c1} [rad]	i_{c1} [rad]	a_{c2} [AU]	e_{c2}	Ω_{c2} [rad]	ω_{c2} [rad]	i_{c2} [rad]
1	$rnd\mathcal{R}(1)$	0.1	2.66	0.433	1	$rnd\mathcal{R}(1)$	3.58	4	-0.785

peaks spectra. Even when the the spectral lines of both SMBHs are well blended as in blue-coloured models in Figs. 1C d and 2C d, their differential phases have two peaks. The profiles and differential phases in Figs. 2C c and 3C d are less dependent on angles Ω and ω of SMBHs and clouds. In this case, eccentricity is the same for SMBHs and clouds in the BLRs. These and other examples illustrate that information from the observables suffices to remove the ambiguities between the orbital elements (see e.g. Figs. 1C b and 1C c).

For fixed observer position i_0 and with increasing SMBHs orbital eccentricity, the amplitude of differential phase decreasing, but with distorted left and right wings (see Figs. 1C a and 1C e). Also, large angles of pericenter of clouds' orbits in both BLRs $\omega_c > \pi/2$ deform core of the differential phase below 0 value. However, an increasing of the angular position of the observer i_0 and SMBH's orbital inclination decreases the slopes of the differential phase (see Figs. 1C d-1C e). In contrast, Fig. 1C f shows obscured effects of clouds' orbital inclination for the fixed observer angle and eccentricities of both SMBHs. For fixed eccentricities of SMBHs and clouds' orbits, different ranges of clouds' orbital inclinations influence appearance of ridges in the wings of differential phases (compare Figs. 2C a-2C c, and 2C d).

For the smaller angle of pericenter of larger SMBH and clouds in its BLR, plateaus between peaks of differential phases are less deformed (see Figs. 2C d- 2C e).

If both SMBHs orbits have small ascending nodes, but larger SMBH orbit has a smaller angle of pericenter, then varying SMBHs and clouds' orbital inclinations affect the amplitude of differential phase wings (Fig. 3C c).

Appendix D: Atlas of interferometric observables for anti-aligned CB-SMBH

We first look at the case of coplanar CB-SMBH, clouds of less massive SMBH have anti-aligned angular momenta, and the inclinations of orbits of clouds are linearly spaced between 90° and 175° (see Figs. 1B a- 1B c). It is also clear from the grid of models presented in Fig. D.1 that if a more substantial number parameters vary simultaneously, the shapes of differential phases will be more complicated. The randomization of nodes and apocenters of clouds' orbits in both BLRs affects the forms of both observables (see upper row of subplots in Fig. D.1). A central whirl is a prominent feature in Figs. 1B b-1B c). Before proceeding further, we make a digression to an auxiliary con-

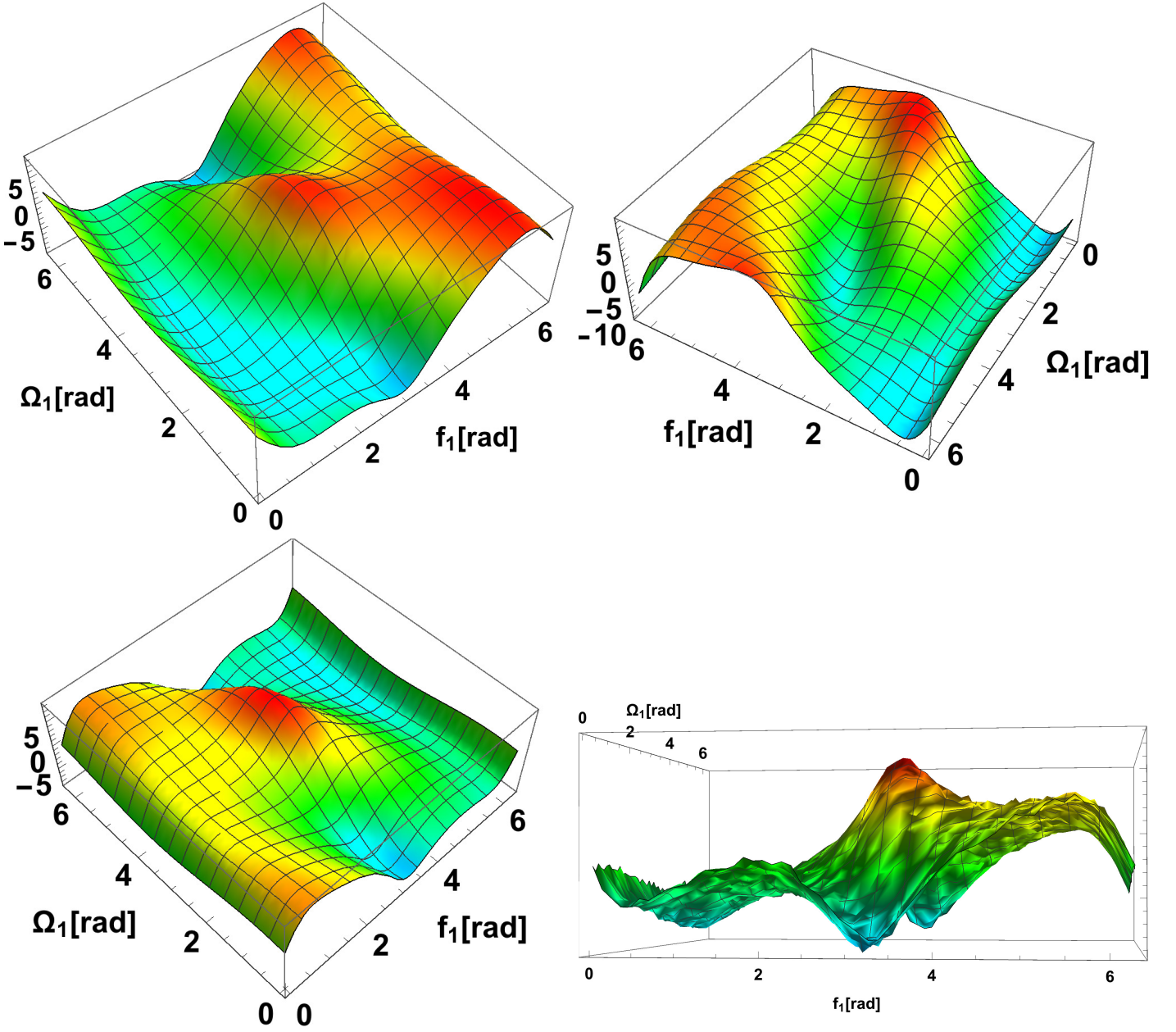
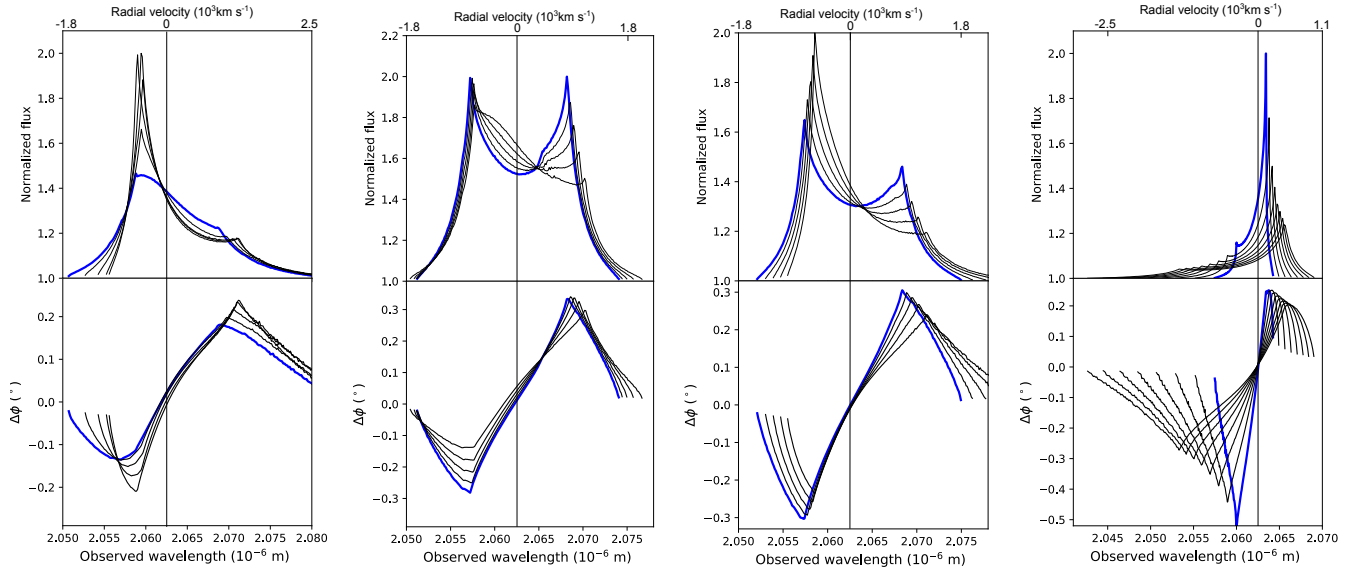


Fig. A.2. The surface mesh of the values of the first parameter in Eq. 13 over a grid of orbital elements of larger SMBH. The ascending node Ω_1 and true anomaly f_1 are given in the XY coordinate plane, and values of the calculated parameter are given on the Z-axis. Upper left plot: Case I - parameters are listed in Table 1Aa. Upper right plot: Case II - parameters are listed in Table 1Ab. Bottom left: Case III - parameters are listed in Table 1Ac. Bottom right: Case IV - parameters are listed in Table 1Ad.

sideration. For $i_0 = 10^\circ$, spectral lines have concave wings and narrow core. As i_0 increases, the line shapes broaden with convex sides. Still differential phases vary drastically in their amplitudes, widths, and forms. Wings of line shapes are arched if we randomize the inclinations of orbits of clouds in the BLR of more massive SMBH (see lower subfigures in Fig. D.1).

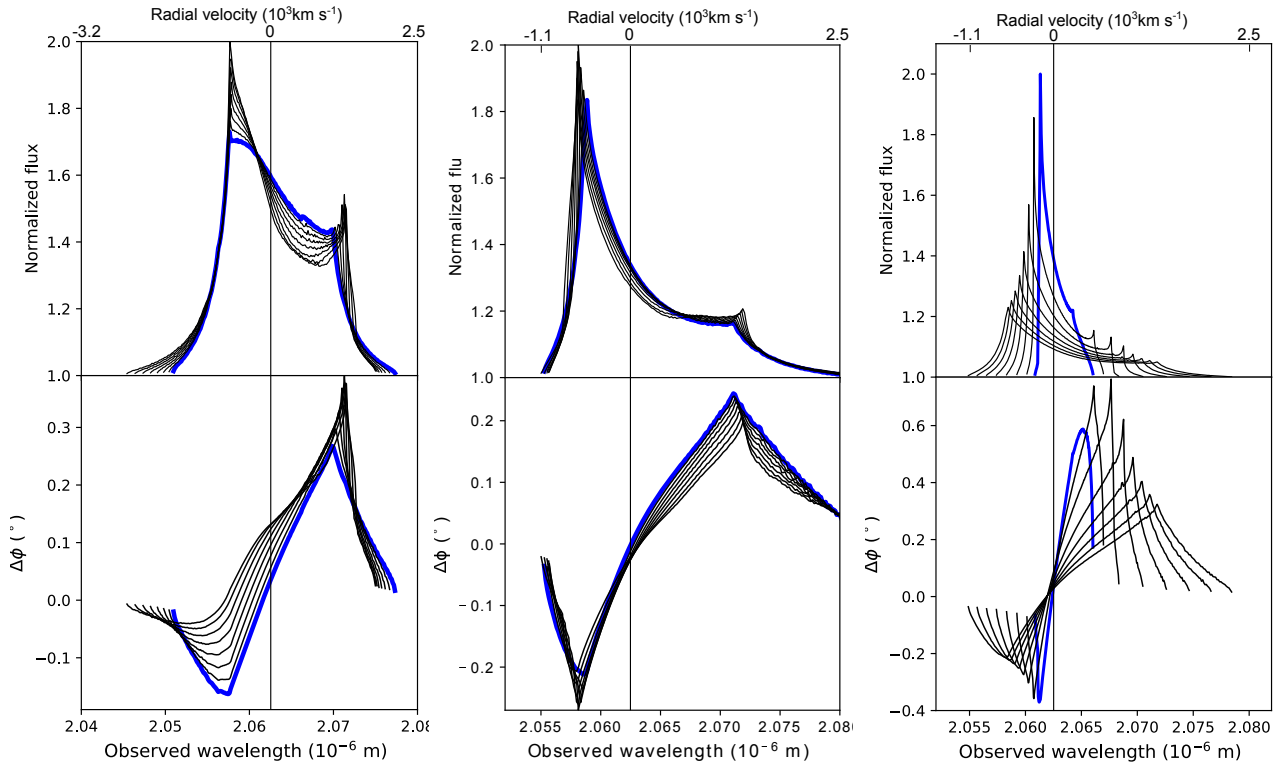
For a simultaneous variation of orbital eccentricities of clouds and SMBHs, and anti-aligned angular momenta of clouds in the BLR of larger SMBH, the convex shape of the line core appears (see blue line model in Fig. 2B a). The dip between the peaks is filled because of a more dispersed velocity field. However, concavity appears when orbital eccentricities of clouds in both BLRs and SMBHs change in opposite directions (seen line

profiles in Figs. 2B b and 2B c). Further, simultaneous variation of inclinations of observer and mutual inclinations of SMBHs orbits are investigated (see bottom panels in Figs. 2B d - 2B g). Spectral lines are narrower, with a broken wing. The form of the spectral line marked with blue colour in Fig. 2B g resembles some well known examples of 'Eiffel Tower' shapes of Pa α seen in 3C 273 and Mrk 110 (Landt et al. 2008, see their Fig.3). We observe that top of spectral line became convex when i_0 is increasing and mutual SMBH orbital inclination is decreasing. Differential phases evolution is remarkable in their right wings and plateau variations (see Fig. D.2). Even more drastic effects are given in Figs. 2B d - 2B g.



(Ba) $\Omega_c \in \mathcal{U}(10^\circ, 90^\circ)$, $\omega_c = 110^\circ$, $i_c \in \mathcal{U}(-5^\circ, 5^\circ)$, $e_c = 0.5$, $i_0 = 45^\circ$
 (Bb) $i_c = \mathcal{U}(-5^\circ, 5^\circ)$, $\Omega_c = 100^\circ$, $\omega_c = 10^\circ$, $i_0 = 45^\circ$, $e_c = \mathcal{U}(0.1, 0.5)$
 (Bc) $i_c = \mathcal{U}(-5^\circ, 5^\circ)$, $\Omega_c = 100^\circ$, $\omega_c = 110^\circ$, $i_0 = 45^\circ$, $e_c = \mathcal{U}(0.1, 0.5)$
 (Bd) $i_c = \mathcal{U}(-5^\circ, 5^\circ)$, $\Omega_c = 100^\circ$, $e_c = 0.5$, $\omega_c = 270^\circ$, $i_0 = \mathcal{U}(10^\circ, 45^\circ)$

Fig. B.1. Evolution of the Pa α emission line (upper subplots) and corresponding differential phase ($\Delta\phi$, lower subplots) as a function of the wavelength and radial velocity for different values of clouds orbital parameters in the model of single SMBH. Model parameters are given in sub-captions.



(Ba) $\omega_c = 10^\circ$

(Bb) $\omega_c = 110^\circ$

(Bc) $\Omega = 210^\circ$, $\omega_c = 10^\circ$, $e_c = 0.5$, $i_c = \mathcal{U}(-7.5^\circ, 7.5^\circ)$, $i_0 = \mathcal{U}(10^\circ, 45^\circ)$

Fig. B.2. Same as Fig. B.1 but for fixed values of clouds' orbital eccentricities $e_c = 0.5$ and angular position of observer $i_0 = 45^\circ$ and the range of clouds' orbital inclinations for each model is from $\mathcal{U}(-5^\circ, 5^\circ)$ to $\mathcal{U}(-20^\circ, 20^\circ)$.

Effects of the asynchronous orientation of the angular momenta of clouds' orbit in both BLRs (see Fig. D.3) differs from

the previous two cases. The 'Eiffel Tower' spectral shapes in Fig.

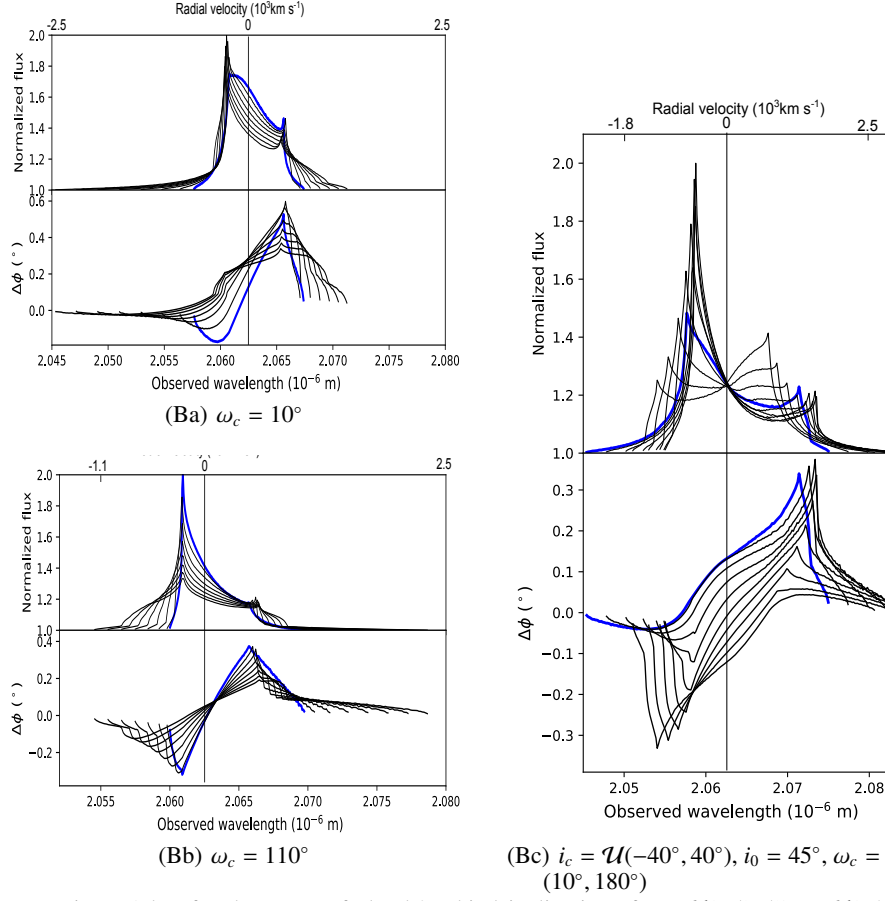


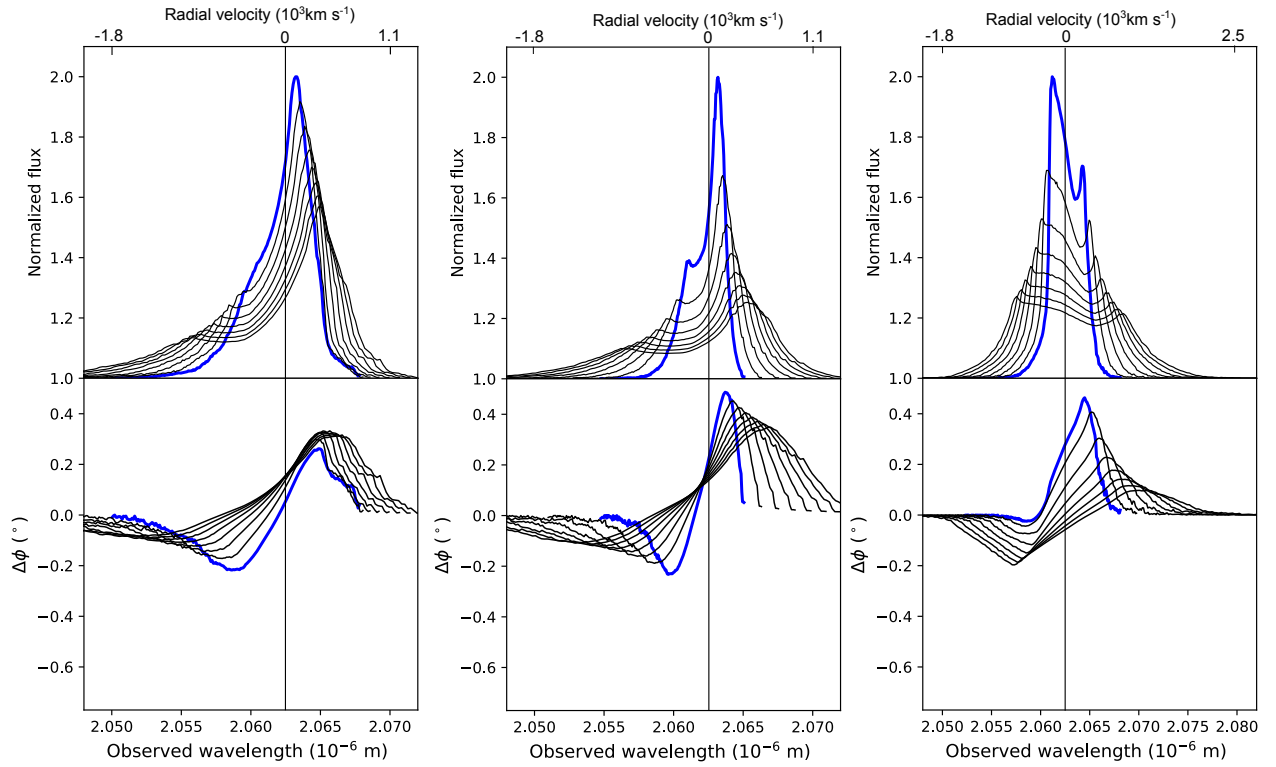
Fig. B.3. Same as Fig. B.1 but for the range of clouds' orbital inclinations from $\mathcal{U}(-5^\circ, 5^\circ)$ to $\mathcal{U}(-20^\circ, 20^\circ)$, fixed values of clouds orbital eccentricities $e_c = 0.5$, and $i_0 = 15^\circ$. The rest of the parameters are given in the sub-captions of the plots.

3B a and Fig. 2B g are similar, yet distinct in their left wings. This is reflecting a difference in Ω of clouds and SMBHs orbits.

More detailed Fig. D.5 summarizes simulations for different combinations of \mathcal{R} distributions of clouds' eccentricities and orbital parameters of SMBHs. Also, notable level of noise is present in the differential phase.

When motion of clouds in both BLRs are non-coplanar, then the differential phase is slightly deformed in the right-wing (see Fig. 5B b). Also, if clouds orbital eccentricities in one of the BLRs are high (0.5), then the differential phase shape will be smoother (see Figs. 5B c and 5B e). The same situation is for coplanar clouds' motion (see Fig. 5B c). Simulation results for $\Gamma_s(0.3, 1)$ distribution of clouds' eccentricities are given in Fig. D.6. For coplanar clouds' motion around a more massive component, the differential phase amplitude decreases (Figs. 6B b-6B d).

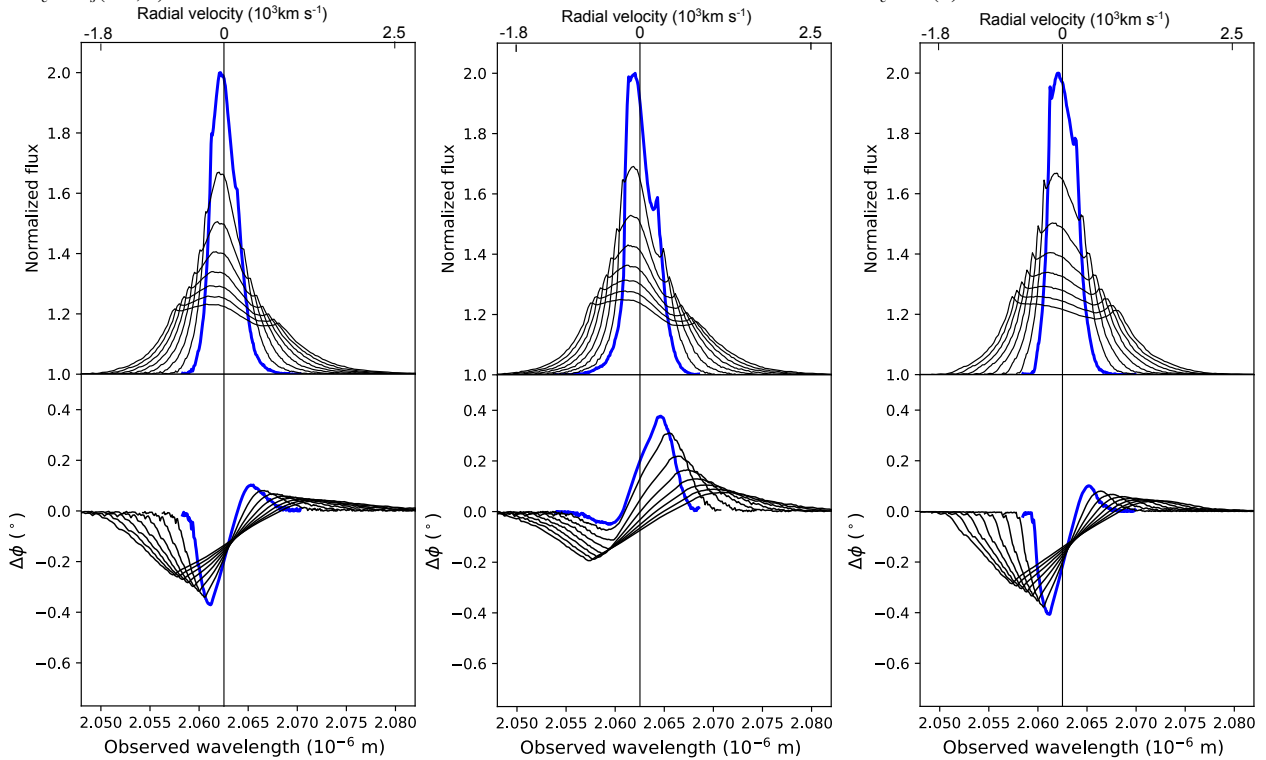
With the disfigured core of the spectral lines, the net effect is that the differential phase peaks shifts away from the line center because of the smaller contribution of lower velocities of clouds. In such cases, the plateau between differential phase peaks is more prominent. The opposite occur when there are higher contributions of projected lower velocities in spectral lines and consequently in the phase profiles.



(Ba) $i_0 = \mathcal{U}(-10^\circ, 45^\circ)$, $\delta i_0 = 5^\circ$, $i_c = \mathcal{U}(-20^\circ, 20^\circ)$, $\Omega_c = 100^\circ$, $\omega_c = 270^\circ$, $e_c \in \Gamma_s(0.3, 1)$

(Bb) $i_0 = \mathcal{U}(-10^\circ, 45^\circ)$, $\delta i_0 = 5^\circ$, C , $\Omega_c = 100^\circ$, $\omega_c = 270^\circ$, $e_c \in \mathcal{R}(1)$

(Bc) $i_0 = \mathcal{U}(-10^\circ, 45^\circ)$, $\delta i_0 = 5^\circ$, $i_c = \mathcal{U}(-10^\circ, 10^\circ)$, $\Omega_c = 100^\circ$, $\omega_c = 10^\circ$, $e_c \in \mathcal{R}(1)$

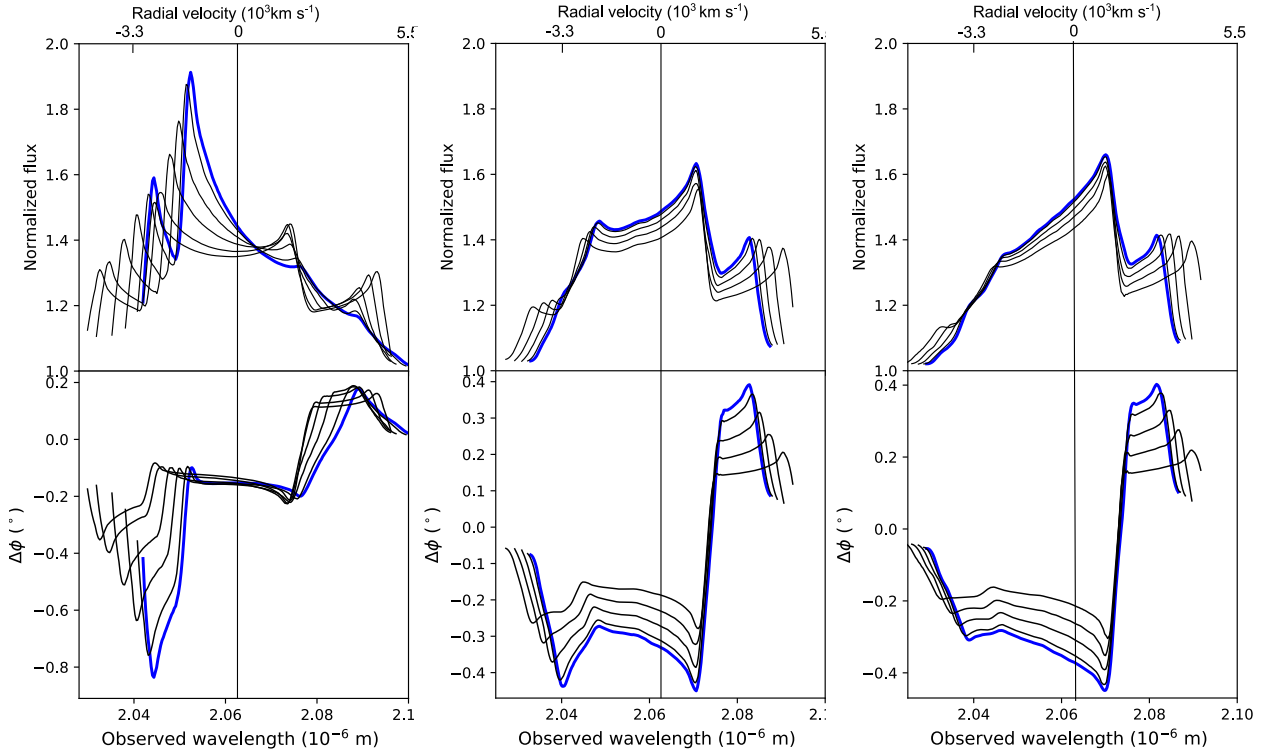


(Bd) $i_0 = \mathcal{U}(-10^\circ, 45^\circ)$, $\delta i_0 = 5^\circ$, C , $\Omega_c = 100^\circ$, $\omega_c = 10^\circ$, $e_c \in \Gamma_s(0.3, 1)$

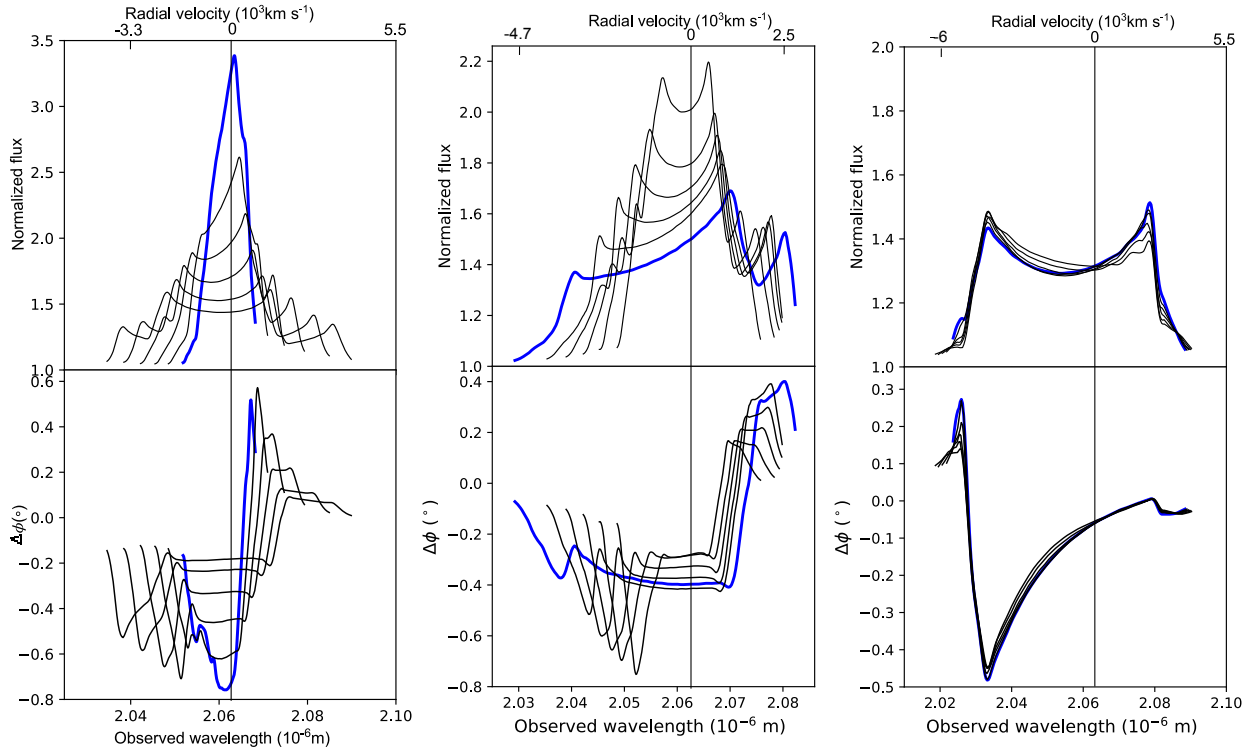
(Be) $i_0 = \mathcal{U}(-10^\circ, 45^\circ)$, $\delta i_0 = 5^\circ$, $i_c = (-7.5^\circ, 7.5^\circ)$, $\Omega_c = 100^\circ$, $\omega_c = 10^\circ$, $e_c \in \Gamma_s(0.3, 1)$

(Bf) $i_0 = \mathcal{U}(-10^\circ, 45^\circ)$, $\delta i_0 = 5^\circ$, C , $\Omega_c = 100^\circ$, $\omega_c = 10^\circ$, $e_c \in \mathcal{R}(1)$

Fig. B.4. Same as Fig. B.1 but for random samples of clouds' orbital eccentricities generated from $\Gamma_s(0.3, 1)$ and $\mathcal{R}(1)$ distributions. Varying parameters are listed in sub-captions, C stands for coplanar clouds orbits.

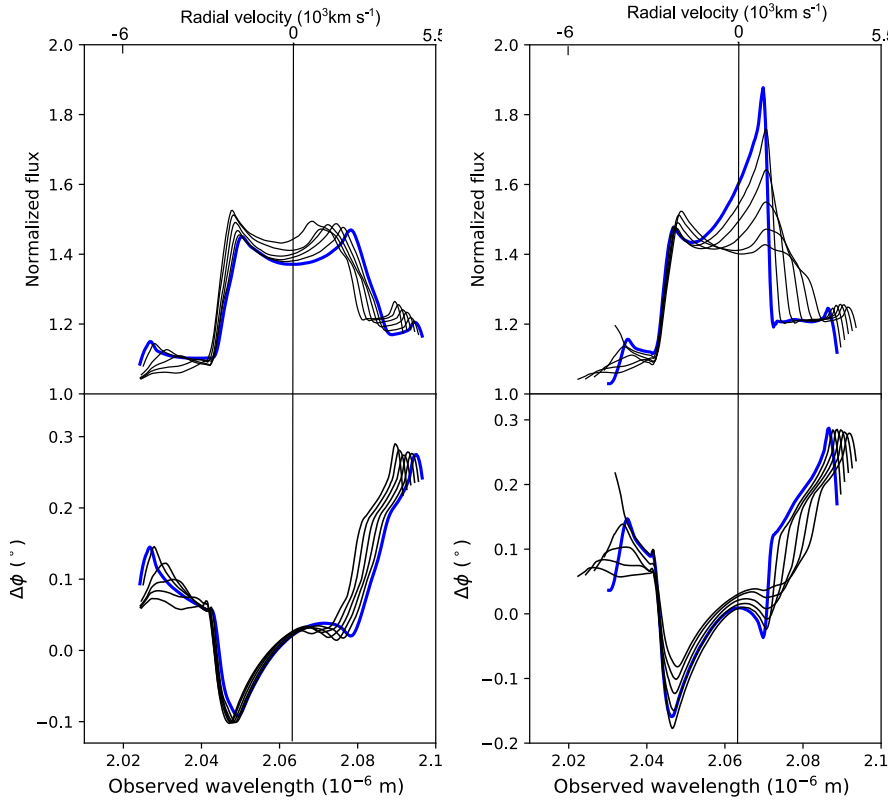


(C a) $i_0 = 45^\circ; C, \Omega_k = 100^\circ, \omega_k = 110^\circ, e_k = \mathcal{U}(0.05, 0.1 - 0.4, 0.45), k = 1, 2, \delta e_k = 0.1; i_c = \mathcal{U}(-5^\circ, 5^\circ), \Omega_c = 10^\circ, \omega_c = 180^\circ, e_c = \tilde{e}_k$ (C b) $i_0 = 45^\circ; i_k = \mathcal{U}(0^\circ, 45^\circ), \delta i_k = 5^\circ, \Omega_k = 100^\circ, \omega_k = 110^\circ, e_k = \mathcal{U}(0.05, 0.1 - 0.4, 0.45), \delta e_k = 0.1, k = 1, 2, i_c = \mathcal{U}(-5^\circ, 5^\circ), \Omega_c = 10^\circ, \omega_c = 50^\circ, e_c = 0.25$ (C c) $i_0 = 45^\circ; i_k = \mathcal{U}(0^\circ, 45^\circ), \delta i_k = 5^\circ, \Omega_k = 100^\circ, \omega_k = 110^\circ, e_k = \mathcal{U}(0.05, 0.1 - 0.4, 0.45), \delta e_k = 0.1, k = 1, 2, i_c = \mathcal{U}(-5^\circ, 5^\circ), \Omega_c = 10^\circ, \omega_c = 50^\circ, e_c = 0.45$



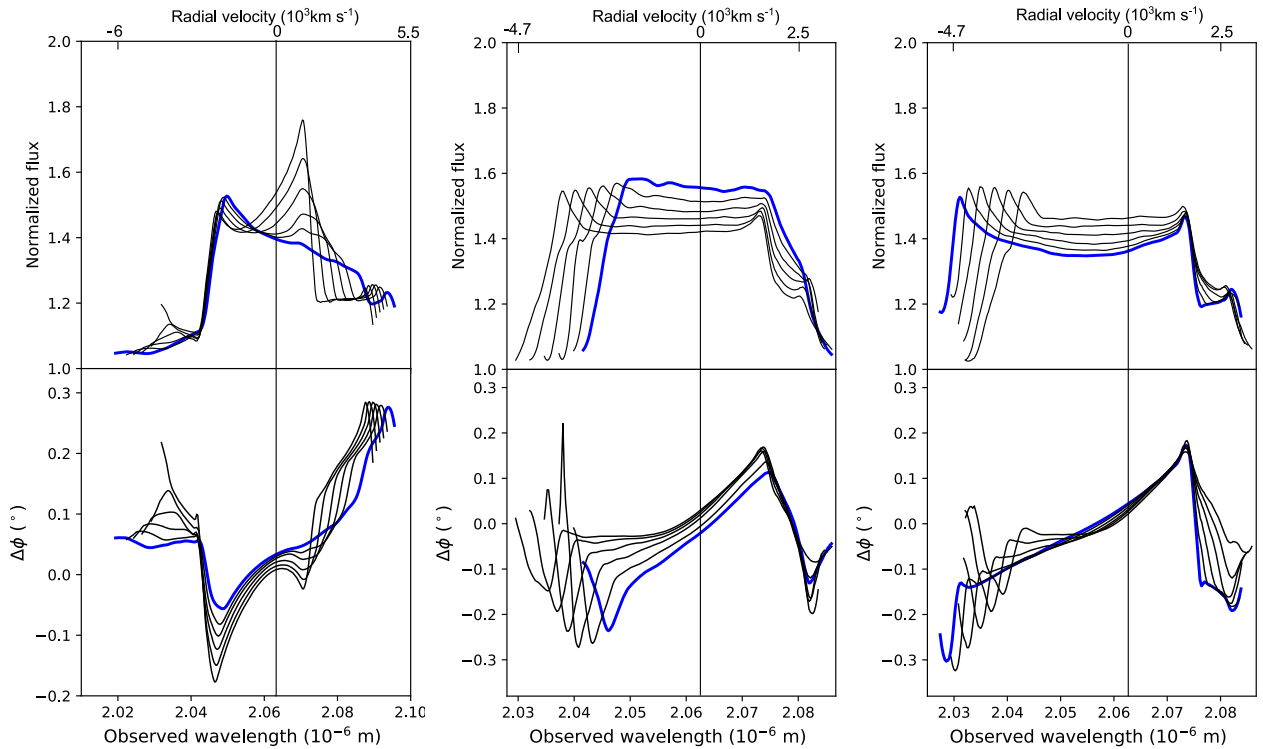
(C d) $i_0 = \mathcal{U}(10^\circ, 45^\circ), \delta i_0 = 5^\circ; C, \Omega_k = 100^\circ, \omega_k = 110^\circ, e_k = \mathcal{U}(0.05, 0.1 - 0.4, 0.45), \delta e_k = 0.1, k = 1, 2; i_c = \mathcal{U}(-5^\circ, 5^\circ), \Omega_{c1} = 200^\circ, \omega_{c1} = 150^\circ, \Omega_{c2} = 10^\circ, \omega_{c2} = 50^\circ, e_c = \tilde{e}_k$ (C e) $i_0 = \mathcal{U}(45^\circ, 10^\circ), \delta i_0 = -5^\circ; C, \Omega_k = 100^\circ, \omega_k = 110^\circ, e_k = \mathcal{U}(0.05, 0.1 - 0.4, 0.45), \delta e_k = 0.1, k = 1, 2; i_c = \mathcal{U}(-5^\circ, 5^\circ), \Omega_{c1} = 200^\circ, \omega_{c1} = 150^\circ, \Omega_{c2} = 10^\circ, \omega_{c2} = 180^\circ, e_c = e_k$ (C f) $i_0 = 45^\circ; C, \Omega_1 = 200^\circ, \Omega_2 = 100^\circ, \omega_1 = 110^\circ, e_k = 0.5, k = 1, 2; \mathcal{I} = \mathcal{U}(5^\circ, 45^\circ), \delta \mathcal{I} = 5^\circ, \Omega_{c1} = 200^\circ, \omega_{c1} = 150^\circ, \Omega_{c2} = 10^\circ, \omega_{c2} = 180^\circ, e_c = 0.5$

Fig. C.1. Evolution of the Pa α emission line (upper subplots) and corresponding differential phase ($\Delta\phi$, lower subplots) as a function of the wavelength radial velocity for different models of aligned CB-SMBH system. Common clouds' orbital elements are designed by subscript c. C stands for the coplanar CB-SMBH system. $\mathcal{I} = \mathcal{U}(l, r)$ stands for inclination ranges from $\mathcal{U}(-l, l)$ up to $\mathcal{U}(-r, r)$.



(C a) $i_0 = 45^\circ; i_k = \mathcal{U}(10^\circ, 90^\circ), \delta i_k = 10^\circ,$
 $\Omega_k = 200^\circ, \omega_k = 210^\circ, e_k = 0.5,$
 $k = 1, 2; \mathfrak{I} = \mathcal{U}(5^\circ, 45^\circ), \delta \mathfrak{I} = 5^\circ, \Omega_c =$
 $200^\circ, \omega_{c1} = 290^\circ, \omega_{c2} = 210^\circ, e_c = 0.5$

(C b) $i_0 = 45^\circ; i_k = \mathcal{U}(90^\circ, 10^\circ), \delta i_k = -10^\circ,$
 $\Omega_k = 200^\circ, \omega_k = 210^\circ, e_k = 0.5, k = 1, 2;$
 $\mathfrak{I} = \mathcal{U}(5^\circ, 45^\circ), \delta \mathfrak{I} = 5^\circ, \Omega_c = 200^\circ,$
 $\omega_{c1} = 290^\circ, \omega_{c2} = 210^\circ, e_c = 0.5$

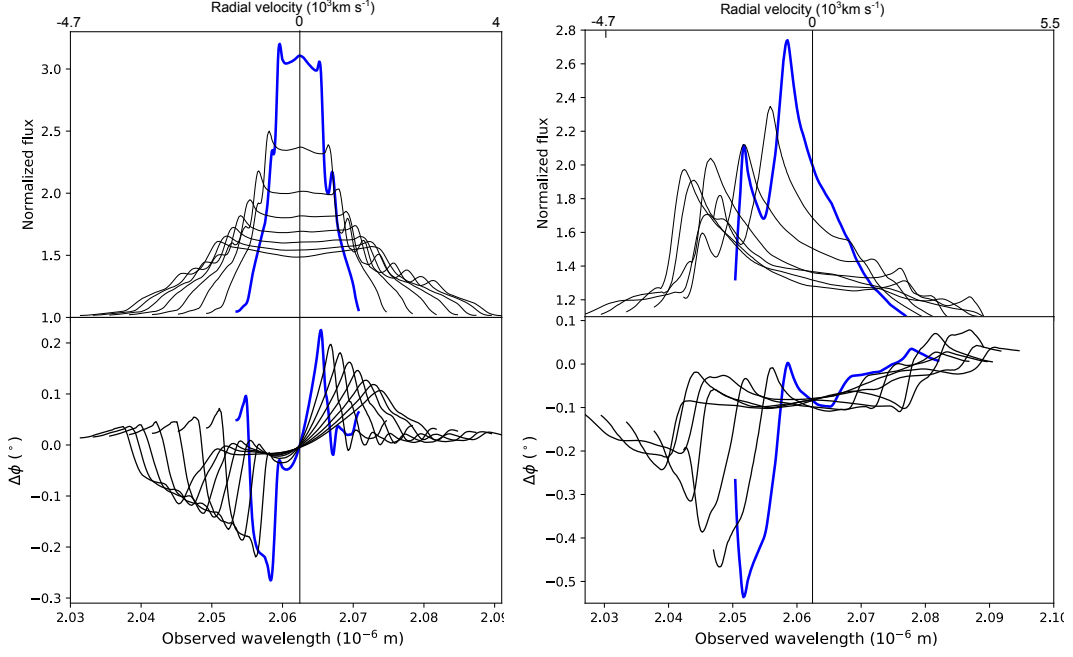


(C c) $i_0 = 45^\circ; i_k = \mathcal{U}(10^\circ, 90^\circ), \delta i_k = -10^\circ,$
 $\Omega_1 = 200^\circ, \Omega_2 = 100^\circ, \omega_k = 210^\circ,$
 $e_k = 0.5, k = 1, 2; \Omega_c = 200^\circ, \omega_{c1} =$
 $150^\circ, \omega_{c2} = 210^\circ, i_{c1} = \text{rnd}(5^\circ, 45^\circ),$
 $i_{c1} = (5^\circ, 45^\circ), e_c = 0.5$

(C d) $i_0 = 45^\circ; i_k = \mathcal{U}(90^\circ, 10^\circ), \delta i_k = -10^\circ,$
 $\Omega_k = 5^\circ, \omega_1 = 5^\circ, \omega_2 = 180^\circ, e_k = 0.5,$
 $k = 1, 2; \mathfrak{I} = \mathcal{U}(5^\circ, 45^\circ), \delta \mathfrak{I} = 5^\circ,$
 $e_c = 0.5, \Omega_c = 100^\circ, \omega_{c1} = 5^\circ,$
 $\omega_{c2} = 180^\circ$

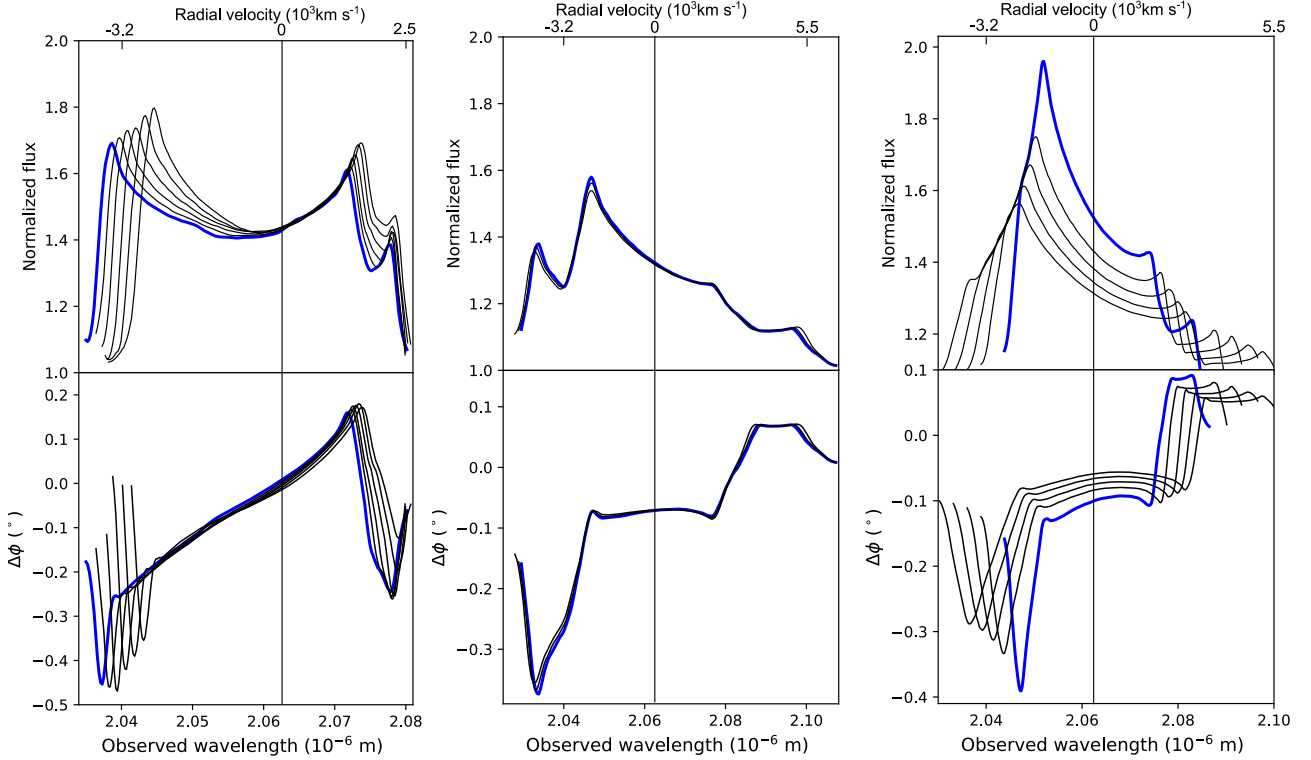
(C e) $i_0 = 45^\circ; i_k = \mathcal{U}(5^\circ, 45^\circ), \delta i_k =$
 $10^\circ, \Omega_k = 5^\circ, \omega_1 = 5^\circ, \omega_2 = 180^\circ, e_k =$
 $0.5, k = 1, 2; \mathfrak{I} = \mathcal{U}(5^\circ, 45^\circ), \delta \mathfrak{I} = 5^\circ, \Omega_c =$
 $100^\circ, \omega_{c1} = 5^\circ, \omega_{c2} = 180^\circ, e_c = 0.5$

Fig. C.2. Same as Fig. C.1 but for different SMBHs and clouds' orbital parameters. Plot (c): *rnd* stands for randomly chosen samples of orbital elements. $\mathfrak{I} = \mathcal{U}(l, r)$ stands for inclination ranges from $\mathcal{U}(-l, l)$ up to $\mathcal{U}(-r, r)$.



(C a) $i_0 = \mathcal{U}(10^\circ, 45^\circ)$, $\delta i_0 = 5^\circ$; $i_k = (10^\circ, 90^\circ)$,
 $\delta i_k = -10^\circ$, $\Omega_k = 5^\circ$, $\omega_1 = 5^\circ$, $\omega_2 = 180^\circ$,
 $e_k = 0.5$, $k = 1, 2$; $\mathfrak{I} = \mathcal{U}(10^\circ, 45^\circ)$,
 $\delta \mathfrak{I} = 5^\circ$, $\Omega_c = 100^\circ$, $\omega_{c1} = 5^\circ$,
 $\omega_{c2} = 180^\circ$, $e_c = 0.5$

(C b) $i_0 = \mathcal{U}(15^\circ, 45^\circ)$, $\delta i_0 = 5^\circ$; $i_k = \mathcal{U}(80^\circ, 20^\circ)$,
 $\delta i_k = -10^\circ$, $\Omega_k = \mathcal{U}(230^\circ, 330^\circ)$, $\delta \Omega_k = 20^\circ$,
 $\omega_k = \mathcal{U}(270^\circ, 170^\circ)$, $\delta \omega_k = 20^\circ$, $e_k = 0.5$,
 $k = 1, 2$; $\mathfrak{I} = \mathcal{U}(5^\circ, 45^\circ)$, $\delta \mathfrak{I} = 5^\circ$, $\Omega_c = \mathcal{U}(80^\circ, 180^\circ)$,
 $\delta \Omega_c = 20^\circ$, $\omega_c = \mathcal{U}(120^\circ, 20^\circ)$, $\delta \omega_c = 20^\circ$, $e_c = 0.5$

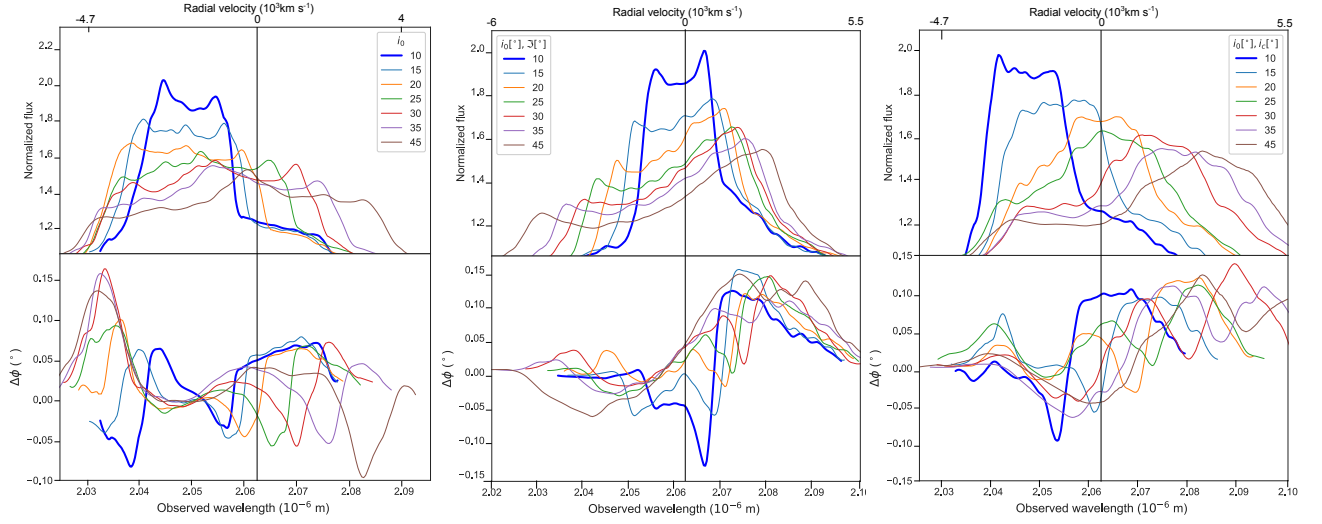


(C c) $i_0 = 45^\circ$; $i_k = \mathcal{U}(10^\circ, 90^\circ)$, $\delta i_k = 10^\circ$,
 $\Omega_k = 5^\circ$, $\omega_1 = 5^\circ$, $\omega_2 = 180^\circ$, $e_k =$
 0.2 , $k = 1, 2$; $\mathfrak{I} = \mathcal{U}(5^\circ, 45^\circ)$, $\delta \mathfrak{I} =$
 5° , $\Omega_c = 200^\circ$, $\omega_{c1} = 290^\circ$, $\omega_{c2} =$
 210° , $e_c = 0.2$

(C d) $i_0 = 45^\circ$; $i_k = 5^\circ$, $\Omega_k = \mathcal{U}(20^\circ, 180^\circ)$,
 $\delta \Omega_k = 20^\circ$, $\omega_k = \mathcal{U}(180^\circ, 20^\circ)$, $\delta \omega_k =$
 -20° , $e_k = 0.5$, $k = 1, 2$; $i_c = 5^\circ$, $\Omega_c = \Omega_k$,
 $\omega_{c1} = \omega_k$, $e_c = 0.5$

(C e) $i_0 = \mathcal{U}(20^\circ, 45^\circ)$, $\delta i_0 = 5^\circ$; $i_k = 10^\circ$,
 $\Omega_k = \mathcal{U}(230^\circ, 330^\circ)$, $\delta \Omega_k = 20^\circ$, $\omega_k =$
 $\mathcal{U}(270^\circ, 190^\circ)$, $\delta \omega_k = -20^\circ$, $e_k = 0.5$,
 $k = 1, 2$; $i_c = 5^\circ$, $\Omega_c = \mathcal{U}(80^\circ, 180^\circ)$,
 $\delta \Omega_c = 20^\circ$, $\omega_{c1} = \mathcal{U}(120^\circ, 20^\circ)$,
 $\delta \omega_k = -20^\circ$, $e_c = 0.5$

Fig. C.3. Same as Fig. C.1 but for different SMBHs and clouds' orbital parameters.



(B a) $C, \Omega_k = 100^\circ, \omega_1 = 250^\circ, \omega_2 = 70^\circ, e_k = 0.5, k = 1, 2; i_{c1} = \mathcal{U}(-5^\circ, 5^\circ), i_{c2} = \mathcal{U}(90^\circ, 175^\circ), \Omega_c = \text{rnd}(0.1^\circ, 359^\circ), \omega_{c1} = 120^\circ, \omega_{c2} = 300^\circ, e_c = 0.5$

(B b) $C, \Omega_k = 100^\circ, \omega_1 = 250^\circ, \omega_2 = 70^\circ, e_k = 0.5, k = 1, 2; \mathfrak{I} = \mathcal{U}(10^\circ, 45^\circ), \delta\mathfrak{I} = 5^\circ, i_{c2} = \mathcal{U}(90^\circ - 175^\circ), \Omega_c = \omega_c = \text{rnd}(0.1^\circ, 359^\circ), e_c = 0.5$

(B c) $C, \Omega_1 = 100^\circ, \Omega_2 = 300^\circ, \omega_1 = 100^\circ, \omega_2 = 180^\circ, e_k = 0.5, k = 1, 2; \mathfrak{I} = (10^\circ, 45^\circ), \delta\mathfrak{I} = 5^\circ, i_{c2} = \mathcal{U}(90^\circ - 175^\circ), \Omega_c = \text{rnd}(0.1^\circ, 359^\circ), \omega_{c1} = 220^\circ, \omega_{c2} = 40^\circ, e_c = \text{rnd}(0.1, 0.5)$

Fig. D.1. Same as Fig. C.1 but for anti-aligned angular momenta of clouds in the BLR of less massive SMBH.

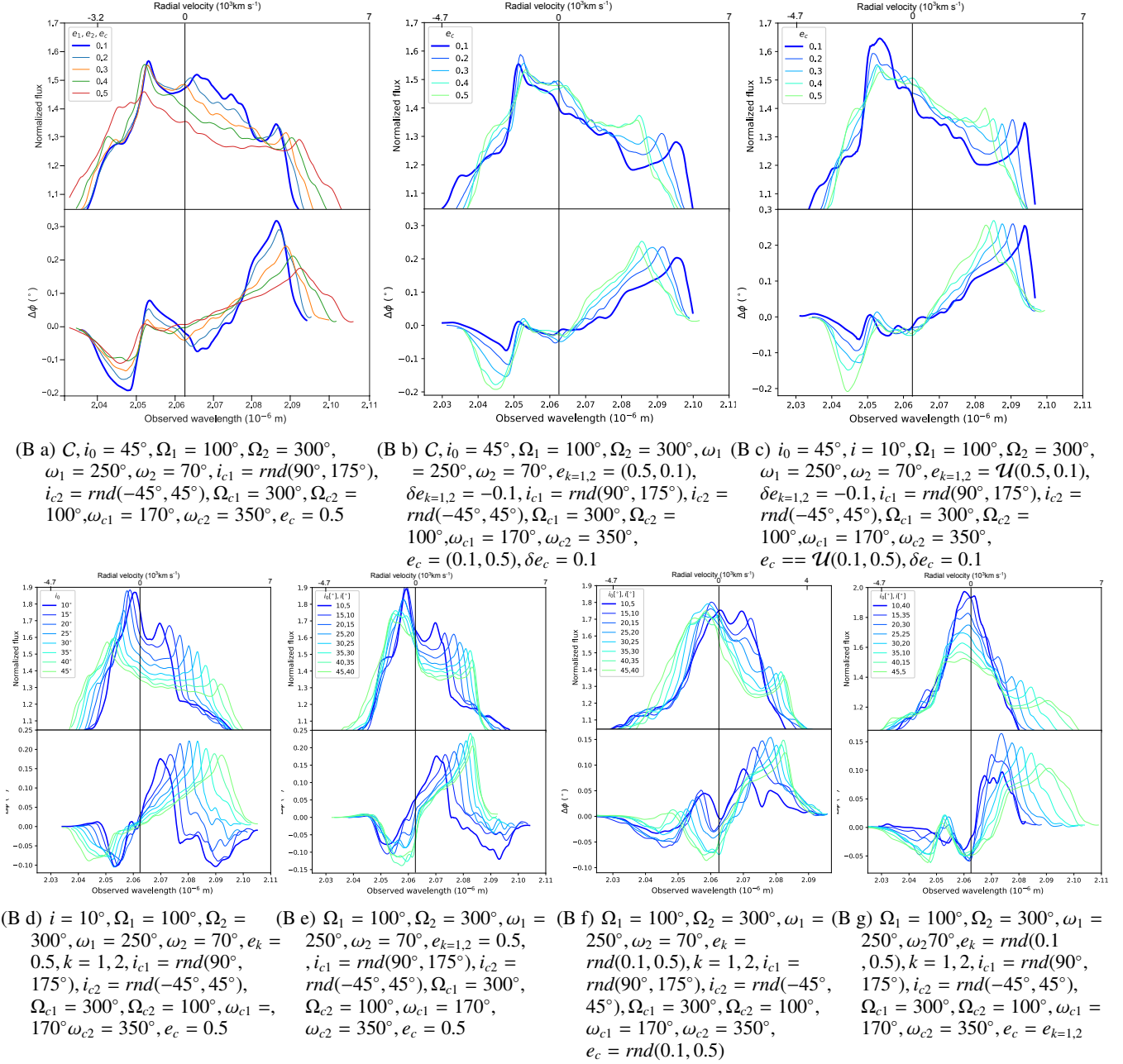
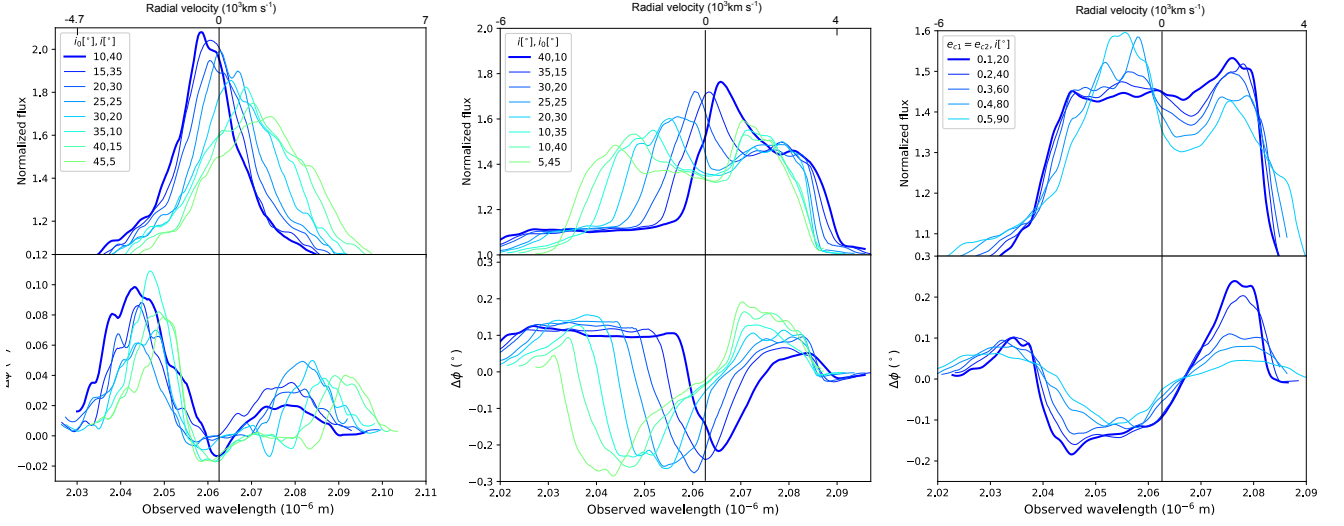
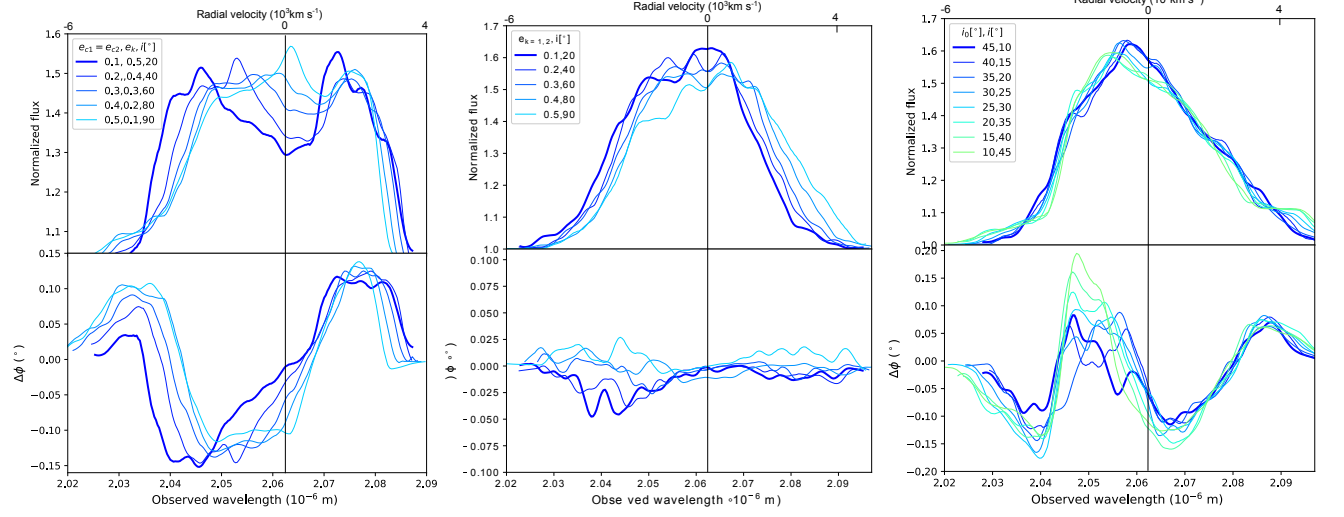


Fig. D.2. Same as Fig. D.1 but for anti-aligned angular momenta of clouds' orbits in the BLR of larger SMBH.

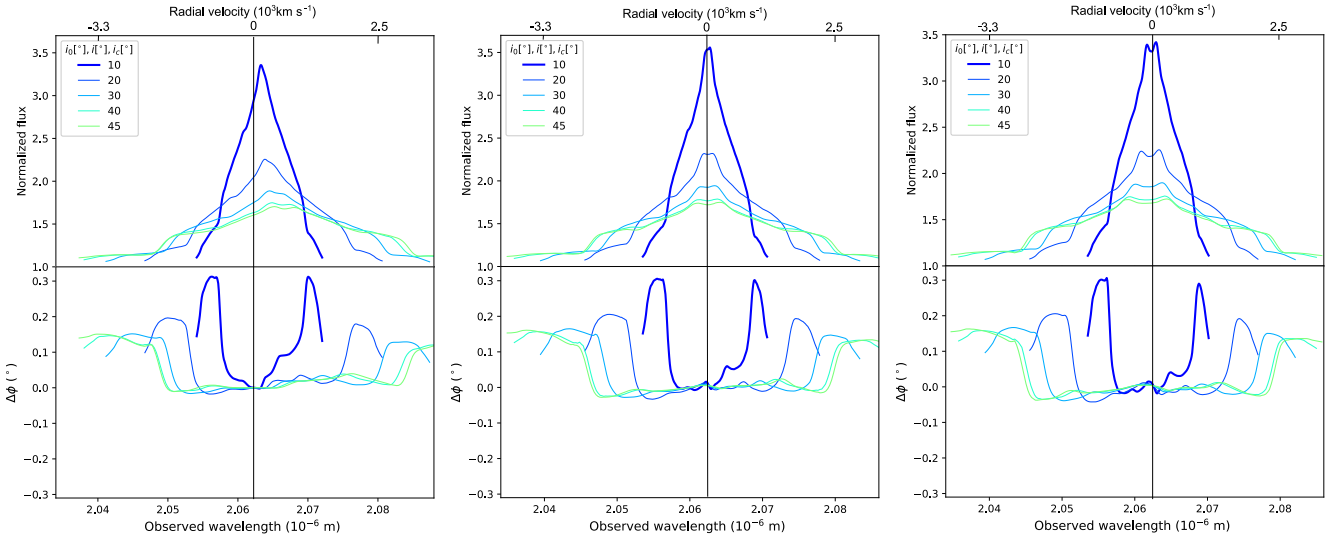


(B a) $\Omega_k = 300^\circ$, $e_k = \text{rnd}(0.1, 0.5)$, $k = 1, 2$, (B b) $\Omega_1 = 300^\circ$, $\Omega_2 = 100^\circ$, $e_k = 0.5$, $k = 1, 2$, (B c) $i_0 = 45^\circ$, $\Omega_1 = 100^\circ$, $\Omega_2 = 300^\circ$, $e_k = (0.1, 0.5)$, $k = 1, 2$, $\omega_1 = 250^\circ$, $\omega_2 = 70^\circ$, $\Omega_{c1} = 300^\circ$, $\Omega_{c2} = 300^\circ$, $\omega_{c1} = 170^\circ$, $\omega_{c2} = 350^\circ$, $e_c = \text{rnd}(0.1, 0.5)$, $\omega_1 = 250^\circ$, $\omega_2 = 70^\circ$, $\Omega_{c1} = 100^\circ$, $\Omega_{c2} = 300^\circ$, $\omega_{c1} = 350^\circ$, $\omega_{c2} = 170^\circ$, $e_c = 0.5$

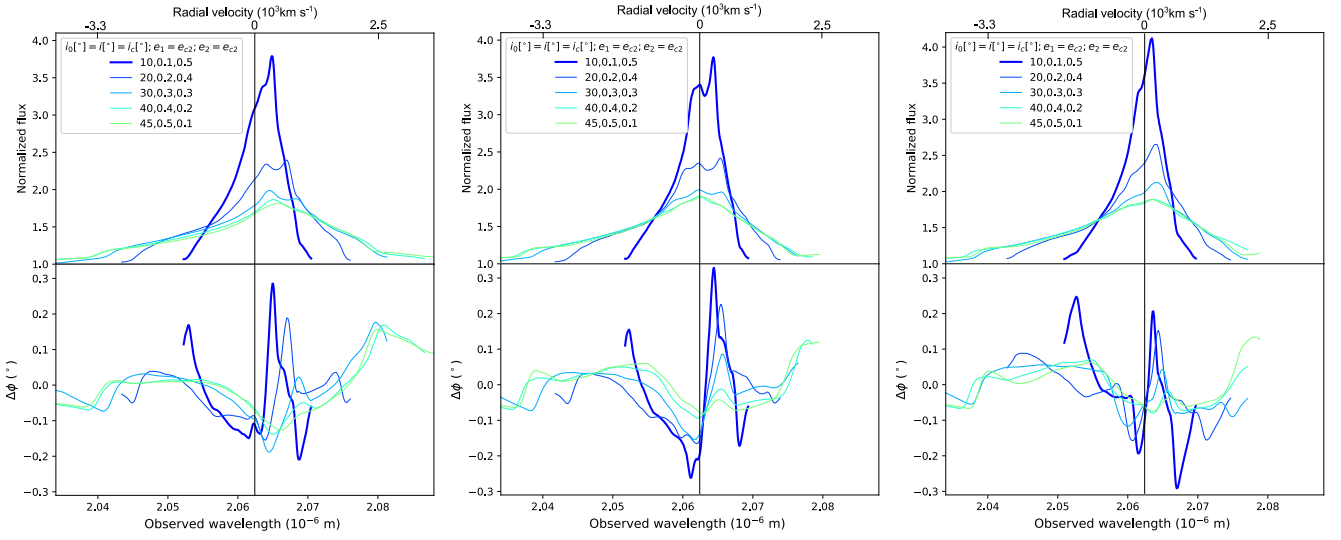


(B d) $i_0 = 45^\circ$, $\Omega_1 = 100^\circ$, $\Omega_2 = 300^\circ$, $\omega_1 = 250^\circ$, $\omega_2 = 70^\circ$, $\Omega_{c1} = 100^\circ$, $\Omega_{c2} = 300^\circ$, $\omega_{c1} = 350^\circ$, $\omega_{c2} = 170^\circ$, (B e) $\Omega_1 = 350^\circ$, $\Omega_2 = 100^\circ$, $\omega_1 = 230^\circ$, $\omega_2 = 50^\circ$, $e_k = 0.5$, $k = 1, 2$, $e_c = \text{rnd}(0.1, 0.5)$, $\Omega_c = \omega_c = \text{rnd}(10^\circ, 290^\circ)$, (B f) $\Omega_1 = 350^\circ$, $\Omega_2 = 300^\circ$, $\omega_1 = 50^\circ$, $\omega_2 = 230^\circ$, $e_k = 0.5$, $k = 1, 2$, $\Omega_{c1} = 100^\circ$, $\Omega_{c2} = \text{rnd}(10^\circ, 290^\circ)$, $\omega_{c1} = 100^\circ$, $\omega_{c2} = 280^\circ$, $e_c = 0.5$

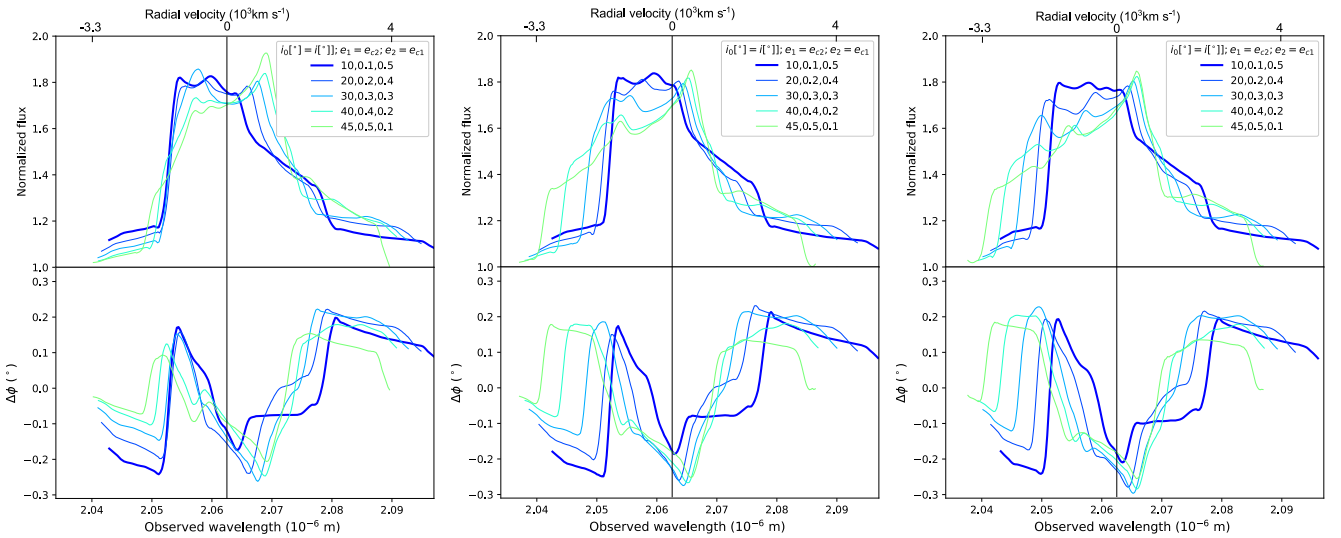
Fig. D.3. Same as Fig. D.2 but for anti-aligned angular momenta of clouds in both BLRs. Clouds' orbital inclinations are randomly distributed within the range $(90^\circ, 175^\circ)$.



(B a) $A_0 = 100\text{ld}$, $i_0 = i = (10^\circ - 40^\circ, 45^\circ)$, $\Omega_1 = 200^\circ$, $\Omega_2 = 150^\circ$, $e_k = 0.5$, $k = 1, 2$, $\omega_1 = 70^\circ$, $\omega_2 = 250^\circ$, $i_{c1} = i_{c2} = (10^\circ - 40^\circ, 45^\circ)$, $\Omega_{c1} = \Omega_{c2} = 200^\circ$, $\omega_{c1} = 100^\circ$, $\omega_{c2} = 280^\circ$, $e_c = 0.5$

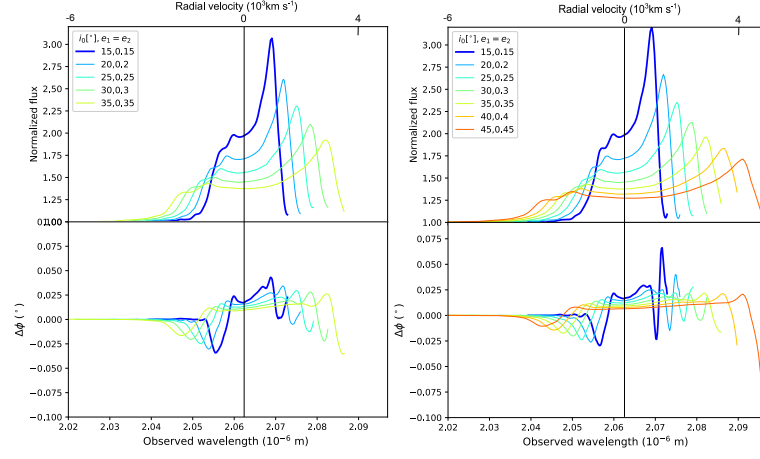


(B b) $A_0 = 100\text{ld}$, $i_0 = i = (10^\circ - 40^\circ, 45^\circ)$, $\Omega_1 = 200^\circ$, $\Omega_2 = 150^\circ$, $e_1 = (0.1, 0.5)$, $e_2 = (0.5, 0.1)$, $\omega_1 = 70^\circ$, $\omega_2 = 250^\circ$, $i_{c1} = i_{c2} = (10^\circ - 40^\circ, 45^\circ)$, $\Omega_{c1} = \Omega_{c2} = 200^\circ$, $\omega_{c1} = 100^\circ$, $\omega_{c2} = 280^\circ$, $e_{c1} = e_2$, $e_{c2} = e_1$



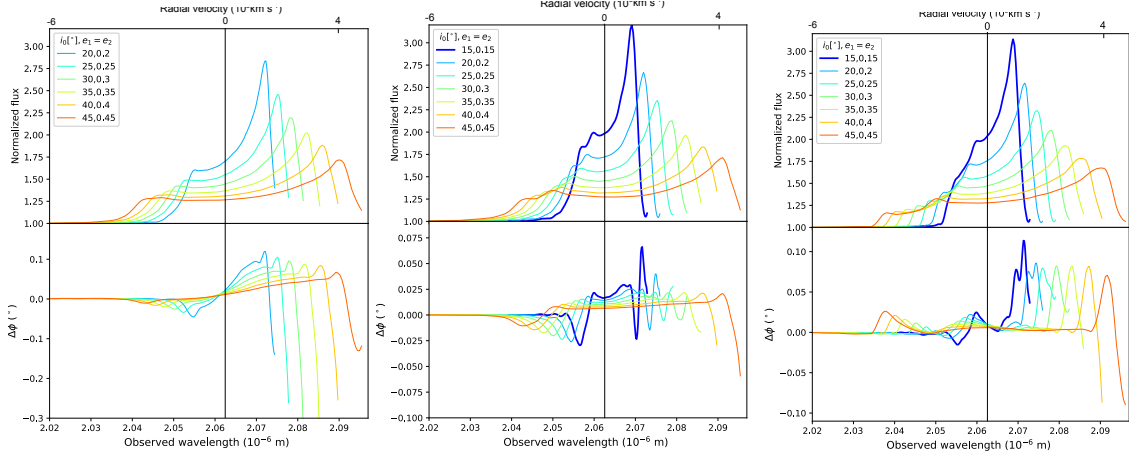
(B c) $A_0 = 100\text{ld}$, $i_0 = i = (10^\circ - 40^\circ, 45^\circ)$, $\Omega_1 = 200^\circ$, $\Omega_2 = 150^\circ$, $e_1 = (0.1, 0.5)$, $e_2 = (0.5, 0.1)$, $\omega_1 = 70^\circ$, $\omega_2 = 250^\circ$, $i_{c1} = i_{c2} = \text{rnd}(90^\circ - 175^\circ, 45^\circ)$, $\Omega_{c1} = \Omega_{c2} = 200^\circ$, $\omega_{c1} = 100^\circ$, $\omega_{c2} = 280^\circ$, $e_{c1} = e_2$, $e_{c2} = e_1$

Fig. D.4. Simulated interferometric observables for the CB-SMBH system during three orbital phases. From first to third column: $\Theta(t) = (0, 0.25)$ with an increment of 0.5. Varying orbital parameters are listed in legends and sub-captions.



(B a) $C, \Omega_k = 100^\circ, \omega_1 = 110^\circ, \omega_2 = 290^\circ,$
 $i_c = \mathcal{U}(-5^\circ, 5^\circ), \Omega_{c1} = 200^\circ, \Omega_{c2} = 10^\circ, \omega_{c1} = 150^\circ, \omega_{c2} = 330^\circ,$
 $e_{c1} = e_{c2} = \text{rnd}\mathcal{R}(1)$

(B b) $C, \Omega_k = 100^\circ, k = 1, 2, \omega_1 = 110^\circ,$
 $\omega_2 = 290^\circ, C, \Omega_{c1} = 200^\circ, \Omega_{c2} = 10^\circ, \omega_{c1} = 150^\circ, \omega_{c2} = 330^\circ,$
 $e_{c1} = e_{c2} = \text{rnd}\mathcal{R}(1)$

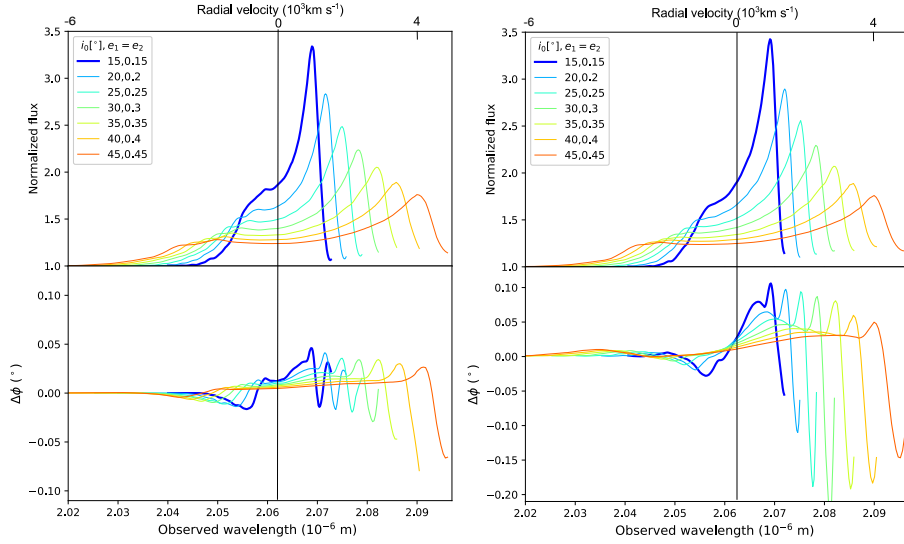


(B c) $C, \Omega_k = 100^\circ, k = 1, 2, \omega_1 = 110^\circ,$
 $\omega_2 = 290^\circ, i_{c1} = C, i_{c2} = \mathcal{U}(-5^\circ, 5^\circ), \Omega_{c1} = 200^\circ, \Omega_{c2} = 10^\circ, \omega_{c1} = 150^\circ, \omega_{c2} = 330^\circ,$
 $e_{c1} = \text{rnd}\mathcal{R}(1), e_{c2} = 0.5$

(B d) $C, \Omega_k = 100^\circ, k = 1, 2, \omega_1 = 110^\circ, \omega_2 = 290^\circ, i_{c1} = C, i_{c2} = \mathcal{U}(-5^\circ, 5^\circ), \Omega_{c1} = 200^\circ, \Omega_{c2} = 10^\circ, \omega_{c1} = 150^\circ, \omega_{c2} = 330^\circ,$
 $e_{c1} = e_{c2} = \text{rnd}\mathcal{R}(1)$

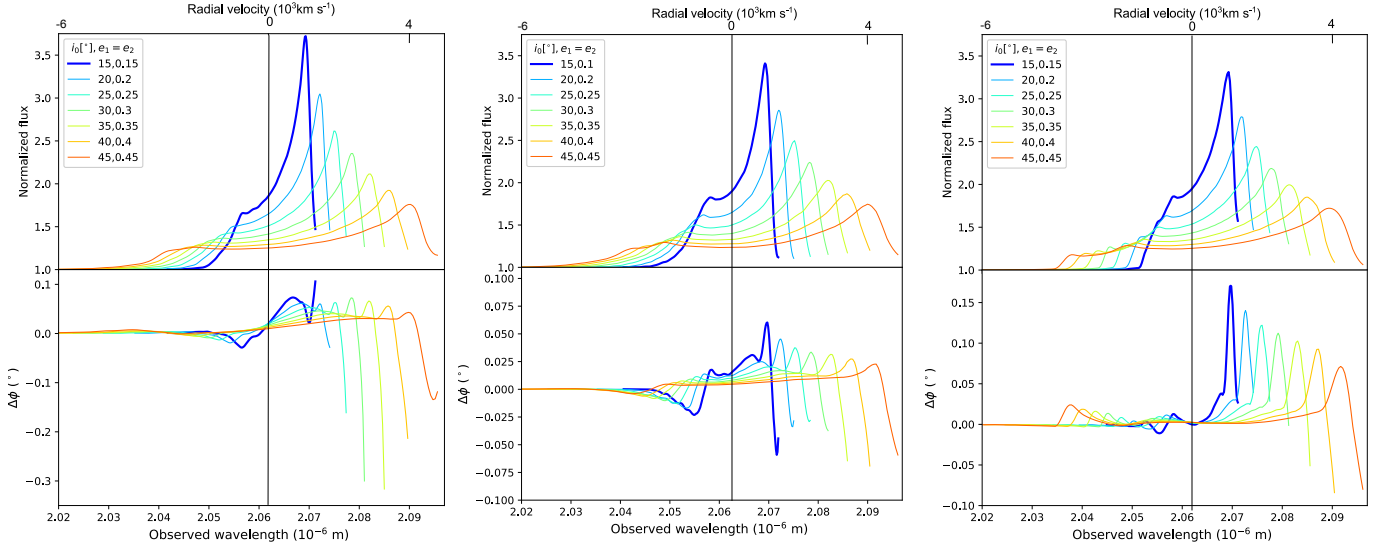
(B e) $C, \Omega_k = 100^\circ, k = 1, 2, \omega_1 = 110^\circ, \omega_2 = 290^\circ, i_{c1} = i_{c2} = \mathcal{U}(-5^\circ, 5^\circ), \Omega_{c1} = 200^\circ, \Omega_{c2} = 10^\circ, \omega_{c1} = 150^\circ, \omega_{c2} = 330^\circ, e_{c1} = 0.5, e_{c2} = \text{rnd}\mathcal{R}(1)$

Fig. D.5. Evolution of the Pa α emission line (upper subplots) and corresponding differential phase ($\Delta\phi$, lower subplots) for the CB-SMBH system as a function of the wavelength and radial velocity. The clouds' orbital eccentricities are drawn from Rayleigh distribution. Varying parameters are listed in sub-captions and legends, and C stands for coplanar orbits.



(B a) $C, \Omega_k = 100^\circ, \omega_1 = 110^\circ, \omega_2 = 290^\circ,$
 $i_c = \mathcal{U}(-5^\circ, 5^\circ), \Omega_{c1} = 200^\circ, \Omega_{c2} =$
 $10^\circ, \omega_{c1} = 150^\circ, \omega_{c2} = 330^\circ,$
 $e_{c1} = e_{c2} = \text{rnd}\Gamma_s(0.3, 1)$

(B b) $C, \Omega_k = 100^\circ, k = 1, 2, \omega_1 = 110^\circ,$
 $\omega_2 = 290^\circ, i_{c1} = \mathcal{U}(-5^\circ, 5^\circ), i_{c2} = C,$
 $\Omega_{c1} = 200^\circ, \Omega_{c2} = 10^\circ, \omega_{c1} = 150^\circ,$
 $\omega_{c2} = 330^\circ, e_{c1} = \text{rnd}\Gamma_s(0.3, 1),$
 $e_{c2} = 0.5$



(B c) $C, \Omega_k = 100^\circ, k = 1, 2, \omega_1 = 110^\circ,$
 $\omega_2 = 290^\circ, i_{c1} = C, i_{c2} = \mathcal{U}(-5^\circ, 5^\circ),$
 $\Omega_{c1} = 200^\circ, \Omega_{c2} = 10^\circ, \omega_{c1} =$
 $150^\circ, \omega_{c2} = 330^\circ, e_{c1} =$
 $\text{rnd}\Gamma_s(0.3, 1), e_{c2} = 0.5$

(B d) $C, \Omega_k = 100^\circ, k = 1, 2, \omega_1 = 110^\circ,$
 $\omega_2 = 290^\circ, i_{c1} = \mathcal{U}(-5^\circ, 5^\circ), i_{c2} = C,$
 $\Omega_{c1} = 200^\circ, \Omega_{c2} = 10^\circ, \omega_{c1} = 150^\circ,$
 $\omega_{c2} = 330^\circ, e_{c1} = e_{c2} =$
 $\text{rnd}\Gamma_s(0.3, 1)$

(B e) $C, \Omega_k = 100^\circ, k = 1, 2, \omega_1 = 110^\circ,$
 $\omega_2 = 290^\circ, i_{c1} = \mathcal{U}(-5^\circ, 5^\circ), i_{c2} = 0$
 $\Omega_{c1} = 200^\circ, \Omega_{c2} = 10^\circ, \omega_{c1} = 150^\circ,$
 $\omega_{c2} = 330^\circ, e_{c1} = 0.5,$
 $e_{c2} = \text{rnd}\Gamma_s(0.3, 1)$

Fig. D.6. Same as Fig. D.5 but for clouds' orbital eccentricities drawn from scaled and shifted $\Gamma_s(0.3, 1)$ distribution.